Westinghouse Non-Proprietary Class 3

WCAP-17642-NP
Revision 0

October 2013

Westinghouse Performance Analysis and Design Model (PAD5)

WCAP-17642-NP
Revision 0

Westinghouse Performance Analysis and Design Model (PAD5)

Tim M. Crede
Fuel Rod and Thermal-Hydraulic Design

Paul J. Kersting
PWR Core Methods

Otto Linsuaín
PWR Core Methods

Yun Long
PWR Core Methods

Guirong Pan
Materials and Fuel Rod Design

Andrew J. Petrarca
PWR Fuel Technology

Dave T. Rumschlag
Fuel Rod and Thermal-Hydraulic Design

Paul Schueren
Licensing and Engineering Programs

Henk Schutte
PWR Fuel Technology

Robert E. Sears
New Reactor Technology

October 2013

Prepared by: Robert E. Sears*
New Reactor Technology

Reviewers: Mike Krammen*
PWR Fuel Technology

Jeff Brown*
Core Engineering

Approved: Robert L. Oelrich, Jr., Manager *
PWR Core Methods

*Electronically approved records are authenticated in the electronic document management system.

Westinghouse Electric Company LLC
1000 Westinghouse Drive
Cranberry Township, PA 16066, USA

TABLE OF CONTENTS

LIST OF TABLES

LIST OF FIGURES

LIST OF ACRONYMS AND TRADEMARKS

AC	Alternating Current
ANC	Advanced Nodal Code
ANSI	American National Standards Institute
AO	Axial Offset
AOO	Anticipated Operational Occurrence
AOR	Analysis of Record
ASI	Axial Shape Index
ASME	American Society Mechanical Engineers
BE	Best Estimate
BOL	Beginning of Life
BWR	Boiling Water Reactor
CAOC	Constant Axial Offset Control
CE	Combustion Engineering
CEA	Commissariat à l'énergie atomique
CFFF	Columbia Fuel Fabrication Facility
CVCS	Chemical and Volume Control System
CWSR	Cold-Worked Stress Relieved
C+V	Calibration and Validation
DNB	Departure from Nucleate Boiling
DOE	Department of Energy
ECCS	Emergency Core Cooling System
EOC	End of Cycle
EOL	End of Life
EOS	Equation of State
EPRI	Electric Power Research Institute
FCEP	Fuel Criteria Evaluation Process
FCL	Fuel Centerline
FGR	Fission Gas Release
FSAR	Final Safety Analysis Report
GDC	General Design Criteria
HB	High Burnup
HBC	High Burnup Chemistry
HBEP	High Burnup Effects Program
HBWR	Halden Boiling Heavy-Water Reactor
ID	Inner Diameter
IFA	Instrumented Fuel Assembly
IFBA	Integral Fuel Burnable Absorber
LB	Lower Bound
LEU	Low-Enriched Uranium
LHGR	Linear Heat Generation Rate
LOCA	Loss of Coolant Accident
LTA	Lead Test Assembly
MAP	Maximum Allowable Power
MHI	Mitsubishi Heavy Industries

LIST OF ACRONYMS AND TRADEMARKS (cont.)

MMIP	Models and Methods Improvement Process
NO	Normal Operation
NRC	Nuclear Regulatory Commission
NSSS	Nuclear Steam Supply System
OD	Outer Diameter
OECD	Organization for Economic Co-Operation and Development
PA	Postulated Accident
PAD	Performance Analysis and Design
PCI	Pellet Clad Interaction
PCMI	Pellet Clad Mechanical Interaction
PIE	Post Irradiation Examination
PNNL	Pacific Northwest National Laboratory
PRTR	Plutonium Recycle Test Reactor
RAOC	Relaxed Axial Offset Control
RCCA	Rod Cluster Control Assembly
RIP	Rod Internal Pressure
SCIP	Studsvik Clad Integrity Project
SG	Steam Generator
SRA	Stress Relieved Anneal
SRP	Standard Review Plan
SRSS	Square Root of Sum of Squares
TCD	Thermal Conductivity Degradation
T.D.	Theoretical Density
TRD	Thermal Reaction accumulated Duty
TRE	Thermal Reaction Energy
UB	Upper Bound
UE	Uniform Elongation
UTS	Ultimate Tensile Stress
VV	Void Volume

1 INTRODUCTION AND SUMMARY

1.1 INTRODUCTION

The principal design tool for evaluating fuel rod performance is the Performance Analysis and Design (PAD) code. This computer program iteratively calculates the interrelated effects of fuel and cladding deformations including fuel densification, fuel swelling, fuel relocation, fuel rod temperatures, fill and fission gas release (FGR), and rod internal pressure (RIP) as a function of time and linear power. PAD evaluates the power history of a fuel rod as a series of steady-state power levels with instantaneous jumps from one power level to another. The length of the fuel rod is divided into several axial segments, and each segment is assumed to operate at a constant set of conditions over its length. Fuel densification and swelling, cladding stresses and strains, temperatures, burnup and fission gas releases are calculated separately for each axial segment and the effects are integrated to obtain the overall fission gas release and resulting internal pressure for each time step. The coolant temperature rise along the fuel rod is calculated based on the flow rate and axial power distribution, and the cladding surface temperature is determined with consideration of corrosion effects and the possibility of local boiling.

The fuel pellet is modeled as a solid cylinder with allowances for dishing, edge chamfering and pellet chipping. For purposes of evaluating thermal expansion, fuel densification and swelling, and fission gas release, the fuel pellet is divided into ten equal-volume concentric rings with each ring assumed to be at its average temperature during a given time step. Axial and radial thermal expansion, swelling and densification are determined for each ring and these effects are integrated over the entire fuel rod to determine the length of the fuel column and evaluate the void volumes (VV) required to compute the internal gas pressure.

The PAD fuel performance models have evolved in several stages from the original application (References 1.1 through 1.9). This report provides a compilation of the licensing basis documentation for all of the significant PAD fuel and clad performance models including descriptions for new models. Where appropriate, model validation data are provided to demonstrate the acceptability of the individual fuel and clad performance models relative to available fuel performance data.

Fuel performance data has been obtained over the past five decades from a number of sources. Commercial reactors provide a substantial portion of the in-reactor fuel performance database, beginning with the examinations of the first Zircaloy-4 clad fuel in the Plant Z reactor in Spain, conducted in the late 1960's and through the 1970's. Data for Westinghouse Improved Zircaloy-4 cladding, and the Westinghouse ZIRLO® cladding material were obtained from commercial irradiations. Data acquisition continues to the present with the recent examinations of **Optimized ZIRLO™** cladding material fuel rods irradiated to very high burnup (HB). Data from these commercial fuel programs has been obtained from both on-site and hot cell examinations to characterize fuel and cladding behavior under normal operation conditions.

Fuel and cladding performance data from commercial irradiation programs are augmented by data obtained under test reactor conditions. Test reactor programs allow for the examination of fuel and cladding performance under off-nominal conditions, such as transient power increases or very high power operation. Test reactor irradiations also allow for additional instrumentation to measure critical parameters such as fuel temperature, internal pressure and cladding elongation. The PAD5 fuel performance database

includes measurement data from jointly sponsored industry programs such as the Halden Project, the Studsvik Clad Integrity Project (SCIP), and the INTERRAMP, SUPERRAMP and TRANSRAMP ramp test programs. The combination of both normal commercial operation and test reactor operation data produces a substantial basis for the calibration and validation of the PAD5 fuel and cladding performance models over the broad range of operating conditions addressed in fuel rod design. Data selected from the database for model Calibration and Validation (C+V) will be identified, as appropriate, for each PAD5 performance model.

1.2 SCOPE AND SUMMARY

The PAD5 models are the latest versions in the Westinghouse PAD code. Model updates incorporated into the PAD code address all of the fuel and cladding performance models required for high burnup fuel design. Key fuel performance updates to the PAD5 models include fuel Thermal Conductivity Degradation (TCD) with burnup, enhanced high burnup athermal fission gas release (pellet rim effects) and enhanced high burnup fission gas bubble swelling. Cladding creep and growth models are also updated to reflect high burnup cladding performance.

In addition to high burnup analysis capability, a key driver for the implementation of the PAD5 models in fuel design is to address regulatory concerns associated with fuel thermal conductivity degradation with burnup. It is intended that, following the Nuclear Regulatory Commission (NRC) review and approval, the PAD5 model will be applied on a forward fit basis to all domestic Westinghouse PWR fuel rod design analyses, including both Westinghouse and Combustion Engineering Nuclear Steam Supply System (CE NSSS) fuel.

A comprehensive description of all PAD5 models is provided in this topical. Some models are unaffected by increased fuel burnup and thermal conductivity degradation and remain the same as in the prior PAD 4.0 version, some models were adjusted to address high burnup and fuel thermal conductivity degradation, and some new models have been incorporated in the code. All PAD models are described in this topical, but the report clearly identifies models that are the same as in PAD 4.0, modified models and new models. Section 2 provides an overview of the PAD5 model changes.

The major performance models in PAD5 are discussed in Sections 3 through 6 of this report, as follows:

- Section 3 Thermal Model, including Thermal Conductivity Degradation
- Section 4 Gas Release and Internal Pressure Model
- Section 5 Fuel and Clad Deformation Models
- Section 6 Fuel and Clad Material Properties

Details of the PAD5 model calibration and validation are provided in Appendix A. Appendix B provides PAD5 model results for several sample cases using the PAD code, including both Westinghouse and CE NSSS fuel rod designs, with and without integral burnable absorbers (either ZrB_2, Gd_2O_3-UO_2, or Er_2O_3-UO_2).

To facilitate implementation of the PAD5 models, this topical combines the description of the PAD5 fuel and clad performance models with an assessment of the fuel rod design criteria to be addressed with the PAD code, including a description of the analysis methods for each criterion. Section 7 summarizes these

fuel rod design criteria and application methods which address the fuel rod design related aspects of the fuel system design as discussed in the US NRC Standard Review Plan (SRP), Section 4.2 (Reference 1.10). The design criteria presented in Section 7 will be applied to all Westinghouse PWR fuel rod designs, and they supersede criteria and evaluation methods previously approved for application to Westinghouse and CE NSSS fuel rod designs.

Section 8 describes a process by which the PAD5 fuel and clad performance models or methods may be improved and implemented in design. The process specifies criteria to be applied to model/model improvements such that, when satisfied, the improved model or method will be acceptable for implementation without requiring additional NRC review and approval. Any model or method improvement that does not satisfy the specified criteria will require explicit NRC review and approval prior to implementation.

In summary, this topical report requests NRC review and approval of:

1. The PAD5 fuel performance models for application to lead rod average burnup up to [ ]^{a,c} for **Optimized ZIRLO** cladding, and 62 GWd/MTU for all ZIRLO and Zircaloy-4 cladding.

2. The fuel rod design criteria and associated PAD5 model evaluation methods for design application to rod average burnup up to [ ]^{a,c}

3. The PAD5 Model and Method Improvement Process (MMIP) that will be applied to future PAD5 model and method changes to determine if these changes are acceptable for implementation without an explicit licensing submittal

1.3 SECTION 1 REFERENCES

1.1 NS-SL-521, NS-SL-524, and NS-SL-543, (Proprietary), and NS-SL-527, and NS-SL-544, (Non Proprietary), Supplemental information on fuel design transmitted from R. Salvatori, Westinghouse, to D. Knuth, AEC, January 1973.

1.2 WCAP-8218-P-A, (Proprietary) and WCAP-8219-A, (Non-Proprietary), "Fuel Densification Experimental Results and Model for Reactor Application," March 1975.

1.3 WCAP-8720 (Proprietary), "Improved Analytical Models Used in Westinghouse Fuel Rod Design Computations," October 1976.

1.4 WCAP-8270 Addendum 2 (Proprietary), "Revised PAD Code Thermal Safety Model," October 1982.

1.5 WCAP-10851-P-A, (Proprietary) and WCAP-11873-A, (Non-Proprietary), "Improved Fuel Performance Models for Westinghouse Fuel Rod Design and Safety Evaluations," August, 1988.

1.6 WCAP-15063-P-A Revision 1, with Errata, (Proprietary) and WCAP-15064-NP-A Revision 1, with Errata, (Non-Proprietary), "Westinghouse Improved Performance Analysis and Design Model (PAD 4.0)," July 2000.

1.7 WCAP-12610-P-A (Proprietary), June 1990 and WCAP-14342-A (Non-Proprietary), "VANTAGE+ Fuel Assembly Reference Core Report," April 1995.

1.8 CENPD-404-P-A, (Proprietary), and CENPD-404-NP-A, (Non-Proprietary), "Implementation of ZIRLO™ Cladding Material in CE Nuclear Power Fuel Assembly Designs," November 2001.

1.9 WCAP-12610-P-A & CENPD-404-P-A, Addendum 1-A (Proprietary) and WCAP-14342-A & CENPD-404-NP-A, Addendum 1-A, (Non-Proprietary), "Optimized ZIRLO™," July 2006.

1.10 NUREG-0800, Standard Review Plan for the Review of Safety Analysis Reports for Nuclear Power Plants, Chapter 4.2, "Fuel System Design," March, 2007.

2 FUEL PERFORMANCE MODELS INTRODUCTION

2.1 BACKGROUND AND PURPOSE

The primary objectives for upgrading the PAD 4.0 Code (Reference 2.1) to PAD5 are to (a) improve and/or validate the fuel and clad performance models for application to high burnup, with a target lead rod average burnup of [ ]^{a,c} GWd/MTU for fuel with **Optimized ZIRLO** cladding material and 62 GWd/MTU for Westinghouse PWR fuel with Zircaloy-4 or ZIRLO® High Performance Fuel Cladding Material and (b) to explicitly model fuel Thermal Conductivity Degradation (TCD) with burnup.

The PAD5 models describe fuel and clad behavior influenced by time, temperature, or burnup dependent phenomena for individual fuel rods. A fuel pin history is followed through a series of time increments during each of which the power is assumed to be constant. Independent radial thermal equilibrium calculations are performed for each discrete axial segment. Fuel burnup, fuel and clad temperatures, fuel fission gas release, and fuel and cladding deformations are calculated for each axial segment, with convergence based on fuel-cladding gap size for each axial segment. The converged results for each segment are coupled to those of other segments through the assumption of complete and instantaneous mixing of the free gases within the fuel rod. The coupling permits integrated, whole rod predictions of fuel rod fission gas release and internal pressure, with convergence based on the total moles of free gas.

This report is written such that the basis for all of the models in the code are justified and supported in a single document, including models that are not changed relative to prior code versions.

2.2 OVERVIEW OF MODEL CHANGES

Table 2.2-1 summarizes the PAD5 models discussed in detail in later sections of this report. Comments in the table highlight whether the models are the same as or changed relative to PAD 4.0.

Table 2.2-1 Fuel Performance Models in PAD5

System	Section	Model	Comments
Thermal	3.1	Thermal Hydraulic	Same as PAD 4.0
	3.2	Film Temperature Drop	Same as PAD 4.0
	3.3	Clad Corrosion	Same as Reference 2.2
	3.4	Clad Temperature Drop	Same as PAD 4.0
	3.5	Gap Conductance	[ ]^{a,c}
	3.6	Fuel Temperature Drop	[ ]^{a,c} Radial power distribution within pellet updated to be consistent with PARAGON (Reference 2.3)
	3.7	Plenum Temperature	Same as PAD 4.0

Table 2.2-1 (cont.) Fuel performance models in PAD5

System	Section	Model	Comments
Gas Release and Internal Pressure	4.1	Helium Solubility and Release	Same as PAD 4.0
	4.2	Helium Release (Zirconium Diboride)	Updated model using Halden test data
	4.3	Fission Gas Release	Updated athermal release model; Added high burnup athermal release model; Recalibrated thermal fission gas release model
	4.4	Equation of State (EOS)	Same as PAD 4.0
	4.5	Gas Absorption In Cladding Effect	Same as PAD 4.0
	4.6	Void Volumes and Internal Pressure	Updated crack volume and gap volume due to relocation model
Fuel and Clad Deformation	5.1	Clad Stresses	Added deviatoric stress for creep and plasticity analysis
	5.2	Clad Elastic Deformation	Same as PAD 4.0
	5.3	Clad Plasticity	[ ]^{a,c}
	5.4	Clad Creep	Revised irradiation creep model. Recalibrated thermal and irradiation creep model with addition of newer data
	5.5	Cladding Diametral Growth	Updated for ZIRLO and **Optimized ZIRLO** cladding
	5.6	Fuel Relocation	Updated to add explicit relocation model
	5.7	Fuel Swelling and Densification	Validated to data with different manufacture processes
	5.8	Fission Gas Bubble Swelling	Recalibrated PAD 4.0 model
	5.9	Rod Axial Growth	Updated with addition of newer data for ZIRLO and **Optimized ZIRLO** cladding
Materials Properties	6.1	Fuel: UO_2/UO_2-Gd_2O_3/UO_2-Er_2O_3	Updated fuel melting temperature [ ]^{a,c} Updated Urania – Gadolinia thermal conductivity model; Added Urania- Erbia Properties; Other properties remain the same as PAD 4.0
	6.2	Zirconium Diboride Integral Fuel Burnable Absorber	Same as PAD 4.0, but updated operating experience

Table 2.2-1 (cont.) Fuel performance models in PAD5			
System	**Section**	**Model**	**Comments**
Materials Properties (cont.)	6.3	Cladding: Zircaloy-4,/ZIRLO and /**Optimized ZIRLO**	Added irradiation hardening on yield strength and ultimate tensile strength; Other properties remain the same as PAD 4.0
	6.4	Fill Gas & Fission Gas Material Properties	Same as PAD 4.0

2.3 LIMITS OF APPLICABLITY

The ranges of applicability for PAD5 fuel rod design and safety analyses are defined by the aggregate of the calibration and validation data used in PAD5, summarized as follows:

- Pressurized water reactor designs using Low-Enriched Uranium (LEU) fuel loading
- Zircaloy-4 (including OPTIN, conventional Zircaloy-4, and improved Zircaloy-4) cladding, ZIRLO cladding, and **Optimized ZIRLO** cladding
- Uranium U^{235} enrichments up to [ ]^{a,c}
- ZrB_2 fuel pellet coating
- Gadolinia concentrations up to [ ]^{a,c}
- Erbia concentrations up to [ ]^{a,c}
- Fuel grain sizes ranging from [ ]^{a,c} to [ ]^{a,c}
- Nominal true pellet density ranging from [ ]^{a,c} to [ ]^{a,c} of the theoretical density of UO_2.
- Rod average burnups up to 62 GWd/MTU for Zircaloy-4 and ZIRLO cladding and up to [ ]^{a,c} for **Optimized ZIRLO** cladding
- Steady-state rod average linear heat generation up to [ ]^{a,c} with local powers up to [ ]^{a,c}
- Transient power and associated fuel centerline temperatures up to the melt temperature defined in subsection 6.1.5

The PAD5 models and application methods will be implemented on a forward fit basis with the fuel design criteria of Section 7 for all Westinghouse PWR fuel, including CE-NSSS applications that

formerly applied FATES3B fuel performance code models and methods. All PAD5 fuel performance models and the ZIRLO and **Optimized ZIRLO** cladding performance models are applicable to current Westinghouse fuel fabricated for CE-NSSS cores. PAD5 may also be used to perform analyses for legacy fuel fabricated with Zircaloy-4 clad, though it is not anticipated that fuel of this vintage would be further irradiated in current reload cores. The PAD5 Zircaoy-4 cladding models are directly applicable to legacy Westinghouse NSSS Zircaloy-4 clad fuel rods. For analysis of CE-NSSS fuel with legacy CE Zircaloy-4 or OPTIN cladding, PAD5 may be applied [

]^{a,c}

2.4 SECTION 2 REFERENCES

2.1 WCAP-15063-P-A Revision 1, with Errata, (Proprietary) and WCAP-15064-NP-A Revision 1, with Errata, (Non-Proprietary), "Westinghouse Improved Performance Analysis and Design Model (PAD 4.0)," July 2000.

2.2 WCAP-12610-P-A & CENPD-404-P-A, Addendum 2 "Westinghouse Clad Corrosion Model for ZIRLO™ and **Optimized ZIRLO™**," November 2008.

2.3 WCAP-16045-P-A (Proprietary) and WCAP-16045-NP-A (Non-Proprietary), "Qualification of the Two-Dimensional Transport Code PARAGON," August 2004.

3 THERMAL MODEL

Section 3 describes the PAD5 models for calculating the temperature distribution for the fuel rod, beginning with the coolant conditions surrounding the individual fuel rod and proceeding inward to the fuel centerline. Independent radial temperature calculations are performed at each axial segment in PAD5. The models described are:

- Coolant thermal-hydraulic model,
- Coolant-to-clad film temperature model, including crud,
- Clad corrosion models, including
  - The oxide-to-metal ratio
  - The clad corrosion temperature drop model
- Clad temperature model,
- Fuel-cladding gap conductance, including
  - Gap gas mixture thermal conductivities
  - Gap gas accommodation
  - Open gap conductance
  - Contact gap conductance,
- Fuel temperature model, including
  - Fuel thermal conductivity, and
- Fuel rod plenum temperature model

3.1 THERMAL HYDRAULIC MODEL

This model is the same as that used in PAD 4.0 (Reference 3.1). Original documentation of this model is located in Attachment P of NS-SL-521 (Reference 3.2) with additional information in Reference 3.9.

The thermal hydraulic model calculates the bulk coolant temperature, $T_{bulk}(z)$, at any axial position:

[ ]^{a,c} (3-1)

where:

$q''(z)$ is the heat flux at axial elevation z,
C_p is the coolant heat capacity,
G is the mass flow rate,
De is the hydraulic diameter,
T_{in} is the inlet water temperature,
[ ]^{a,c}.

Appropriate values for [ ]^{a,c}. A typical value for [ ]^{a,c}.

3.2 FILM TEMPERATURE DROP

This model is the same as that used in PAD 4.0 (Reference 3.1). Original documentation of this model is located in NS-SL-521(Reference 3.2), Attachment P.

The surface temperature of the zirconium oxide layer is derived from the bulk coolant temperature with consideration of the following three modes of heat transfer:

1. Forced convection without boiling using the [ ]^{a,c} and accounting for conduction heat transfer across the crud layer, if present.

2. Nucleate boiling from an essentially clean surface using the [ ]^{a,c}.

3. Nucleate boiling through a crud layer using the [ ]^{a,c}.

The mode of heat transfer is a function primarily of the heat flux and, if assumed to be present, the crud thickness, and to a lesser extent, of fluid and system conditions. For the ZIRLO cladding and **Optimized ZIRLO** cladding corrosion models (References 3.7 and 3.8) [

]^{a,c}

The clad oxide surface temperature under forced convection heat transfer, T_C, is given by:

$$\left[\right]^{a,c} \qquad (3\text{-}2)$$

where:

q'' is the heat flux (BTU/hr·ft^2),
T_{bulk} is the bulk coolant temperature (°F),
h_{film} = the [ ]^{a,c} (BTU/hr-ft^2-°F),
K_f is the crud conductivity under forced convection (BTU/hr-ft-°F),
δ_{crud} is the crud thickness (ft).

If T_C is less than the saturation temperature, T_{sat}, the calculation would proceed to the consideration of the temperature rise through the oxide layer. Otherwise, the film temperature calculation considers the impact of subcooled nucleate boiling.

For typical calculations involving ZIRLO and **Optimized ZIRLO** cladding, [

]^{a,c}, as given by:

[a,c] (3-3)

where:

[

]a,c

and,

T_{sat} is the coolant saturation temperature (°F),
P is the system pressure (psi).

The clad surface temperature using the [ ]a,c heat transfer becomes (References 3.9 and 3.10):

[a,c] (3-4)

where:

[ ]a,c

If crud is explicitly modeled, then the [ ]a,c is also calculated using:

[ ]a,c (3-5)

where:

K_b is the effective crud conductivity in nucleate boiling (BTU /hr-ft-°F)
δ_{crud} is the crud thickness (ft.)

The temperature at the clad oxide surface under nucleate boiling heat transfer is:

[ ]a,c (3-6)

3.2.1 Crud Model

This model is the same as that used in PAD 4.0 (Reference 3.1).[

]a,c

[

]^{a,c}

The crud formation model in PAD provides a means to [

]^{a,c}

The crud thickness model allows for [
]^{a,c} as shown below:

[ ]^{a,c} (3-7)

where:

δ_{crud} is the total crud thickness (mils)

[ ]^{a,c} is an input constant crud thickness (mils) assumed to be formed under [

]^{a,c}

[ ]^{a,c} is the crud thickness (mils) assumed to be formed under [
]^{a,c} conditions.

[ ]^{a,c} (3-8)

where:

[ ]^{a,c} (3-9)

q''_{boil} is the fractional heat transfer through the coolant film layer due to [
]^{a,c}

q'' is the total heat transfer

A_{crud} and B_{crud} are input constants.

3.3 CLAD CORROSION MODELS

3.3.1 ZIRLO Cladding and *Optimized ZIRLO* Cladding

*The ZIRLO and **Optimized ZIRLO** cladding corrosion models have been approved by the NRC (References 3.7 and 3.8) and are incorporated into the PAD code.*

The corrosion model form consists of a Thermal Reaction Accumulated Duty (TRD) term which is an
[

]^{a,c}

[a,c] (3-10)

where:

[

]a,c

[ ]a,c (3-11)

where:

[

]a,c

The [ ]a,c

[ ]a,c (3-12)

where:

[

]a,c

The corresponding TRD is the [ ]a,c

[a,c] (3-13)

where:

T is the total time duration in hours.

The ZIRLO cladding best estimate oxide thickness, CR_{ZIRLO}, is calculated with the expression:

[a,c] (3-14)

The coefficients A and B are model constants.

The **Optimized ZIRLO** cladding best estimate oxide thickness, $CR_{OPTZIRLO}$ is calculated from the [ ]a,c as follows:

[ ]a,c (3-15)

Validation of the ZIRLO and **Optimized ZIRLO** cladding corrosion models was presented in detail in Reference 3.7 and approved in Reference 3.8. Figures 3.3-1 and 3.3-2 (Reference 3.9) illustrate the measured oxide thickness data as a function of TRD for ZIRLO and **Optimized ZIRLO** cladding, respectively, with the upper 95% uncertainty curve.

a,b,c

Figure 3.3-1 ZIRLO Cladding Material Measured Oxide Thickness Versus TRD With Upper 95% Uncertainty Curve (Reference 3.9)

a,b,c

[

]

Figure 3.3-2 *Optimized ZIRLO* Cladding Material Measured Oxide Thickness Versus TRD With Upper 95% Uncertainty Curve (Reference 3.9)

3.3.2 Zircaloy-4 Cladding

The following model was in PAD 4.0 (Reference 3.1) for application to Zircaloy-4 cladding. This model was presented to the NRC in Reference 3.11. Current fuel does not employ Zircaloy-4 cladding. This model is used as required to analyze Zircaloy-4 clad fuel designs. It is applicable for rod average burnup up to [ ]^{a,c}. *Zircaloy-4 clad fuel will not be used in design at burnups greater than this value.*

The Zircaloy-4 cladding corrosion model in PAD describes the in-pile corrosion of Zircaloy-4 fuel cladding in terms of weight gain rate, dw/dt, as follows:

a,c

[ ] (3-16)

where:

a,c

[ ] (3-17)

is the out-of-reactor thermal corrosion rate, in (mg/ dm^2)/ day,

T_K is the oxide surface temperature in kelvins, and:

$$F_1 = [\quad]^{a,c}$$
$$= [\quad]^{a,c}$$

and the in-reactor corrosion acceleration factors are:

[

]^{a,c}

where:

[

]^{a,c}

Figure 3.3-3 shows the measured versus predicted oxide comparisons for the Zircaloy-4 corrosion model applied to Westinghouse conventional and improved Zircaloy-4. Figure 3.3-4 provides the measured minus predicted versus predicted oxide comparisons for Westinghouse conventional and improved Zircaloy-4. The 95% uncertainty bounds are seen in Figure 3.3-4.

a,b,c

Figure 3.3-3 Measured Versus Predicted Oxide Thickness – Westinghouse Zircaloy-4 Model

a,b,c

Figure 3.3-4 Measured Minus Predicted Oxide Thickness – Westinghouse Zircaloy-4 Model

3.3.3 Oxide-to-Metal Ratio

This model is the same as presented in PAD 4.0 (Reference 3.1) and in the recently licensed ZIRLO and ***Optimized ZIRLO*** *cladding corrosion model Topical (References 3.7 and 3.8).*

Due to the differences in densities of the oxide and the base metal, there is volumetric change from the metal consumed to the oxide formation. This volumetric difference results in a thicker oxide than the equivalent thickness of the base metal that was consumed. The ratio of the volumes is characterized by the oxide-to-metal ratio (O/M). The theoretical O/M ratio, O/M_{th}, is referred to as the Pilling-Bedworth ratio, and for zirconium-based alloys, the value of 1.56 is commonly used. However, during the in-reactor generation of ZrO_2, different mechanisms occur that cause the oxide density to be less than theoretical resulting in higher O/M ratios at increasing oxide thickness. As the oxide grows, it transitions from a protective to a non-protective structure. The non-protective oxide contains cracks and pores and this transition occurs when the oxide is about [ ]^{a,c}.

The equations governing the O/M ratio as a function of oxide thickness are as follows:

[a,c] (3-18a)

[a,c] (3-18b)

where:

δ_{ZrO_2} is the oxide thickness (mils).

The cladding base metal wall thickness corrected for oxide, t'_{wall}, is then:

$$t'_{wall} = t_{wall} - \frac{\delta_{ZrO_2}}{O/_M} \tag{3-19}$$

where:

t_{wall} is the initial clad wall thickness.

3.3.4 ZrO_2 Temperature Drop Model

This model is the same as that used in PAD 4.0 (Reference 3.1) and prior PAD versions (References 3.2, 3.12, and 3.14).

The temperature drop across the zirconium oxide layer, δ_{ZrO_2}, is given by:

[a,c] (3-20)

where:

K_{ZrO_2} is the zirconium oxide thermal conductivity (BTU/hr-ft-°F) (see subsection 6.3.2) and
δ_{ZrO_2} is the zirconium oxide thickness (ft).

The temperature at the clad metal-to-oxide interface, $T_{clad}^{m/o}$, is then:

$$T_{clad}^{m/o}(z) = T_C(z) + \Delta T_{ZrO_2} \tag{3-21}$$

where T_C is the temperature at the oxide surface.

3.4 CLAD TEMPERATURE DROP MODEL

This model is the same as presented in PAD 4.0 (Reference 3.1) and prior PAD versions (References 3.2, 3.12, and 3.14.

When the thermal conductivity of the cladding is a [ ]^{a,c} (Reference 3.1 and Subsection 6.3.2):

[ ]^{a,c} (3-22)

then the heat conduction equation can be solved for the cladding inner surface temperature:

[ ]^{a,c} (3-23)

where:

R_o is the clad outer radius,
R_i is the clad inner radius,
$T_{clad}^{m/o}$ is the metal-oxide interface temperature from Equation (3-21), and
TCI is the cladding inner surface temperature.

For the calculations of cladding creep rates and thermal expansion, the cladding average temperature is used. This is found by numerically calculating the volumetric average of the cladding temperature.

3.5 GAP CONDUCTANCE MODEL

This model is modified from that used in PAD 4.0 (Reference 3.1). Original documentation of this model is located in Attachment F of NS-SL-521 (Reference 3.2) and Reference 3.12.

The temperature drop across the pellet to clad gap is given by:

[ ]^{a,c} (3-24)

The gap conductance, h_{gap}, contained in the fuel rod design model is dependent on the [ ]^{a,c}.

3.5.1 Gap Conductance Used for Finite Gaps

The PAD5 gap conductance model for an open gap is given by:

[ ]^{a,c} (3-25)

where:

h_{gap} is the gap conductance (BTU/hr-ft^2-°F),
K_{mix} is the effective gas thermal conductivity (BTU/hr-ft-°F),
GAP is the diametral gap (in),
δ_r is the effective surface roughness (ft).

The gap conductance calculated with Equation (3-33) is used to calculate the temperature drop across the annular gap. The fuel-clad gap is determined by first radially deforming both the fuel and cladding. The cladding is radially deformed considering thermal expansion (subsection 6.3.3), elastic deformation in response to the rod internal pressure and coolant pressure (Section 5.2), creep (Section 5.4), clad diametral growth (Section 5.5), and plastic deformation (Section 5.3). The fuel is radially deformed considering thermal expansion (subsection 6.1.3), relocation (Section 5.6), fuel densification and swelling (Section 5.7), and high temperature fission gas bubble swelling (Section 5.8).

3.5.2 Gas Mixture Thermal Conductivity Model

This model is the same as that used in PAD 4.0 (Reference 3.1). Original documentation of this model is located in Attachment F of Reference 3.2.

[
]^{a,c} The relationship for calculating the thermal conductivity of a monatomic gas mixture is based on the work of [ ]^{a,c}.

a,c
[ ] (3-26)

where the case $i=j$ is excluded from the sum over j (innermost sum) and:

a,c
[ ] (3-27)

a,c
[ ] (3-28)

and

n is the number of component gases in the mixture,
M represents the molecular weight,
x is the mole fraction,
K stands for the thermal conductivity (BTU/hr-ft-°F).

The correlations used for the thermal conductivities of the individual gases in the pellet-cladding gap are described in Section 6.4.

In calculating the gas mixture thermal conductivity for the gas occupying the pellet-cladding gap, the average temperature between the pellet surface and the cladding inner surface is employed.

3.5.3 Accommodation Coefficient

This model is the same as that used in PAD 4.0 (Reference 3.1). Original documentation of this model is located in Reference 3.12.

When the ratio of the mean free path of the gas molecules to the characteristic dimension (gap) of the body exceeds [ ]^{a,c}. Heat transfer from a solid to a gas in this, [ ]^{a,c} is then dependent on an accommodation coefficient which is defined as the ratio of the actual energy interchange to the maximum possible energy interchange between a surface and a gas. Generally the accommodation coefficient factor of a heavy gas such as argon or xenon is near one and this effect can be neglected. But the effect cannot be neglected when the gap is filled with a light gas such as helium. For helium, PAD calculates the following factor by which the bulk thermal conductivity of helium should be divided when calculating temperature drops in [ ]^{a,c}:

$$f_\alpha = 1 + \left(\frac{\alpha_1 + \alpha_2 - \alpha_1\alpha_2}{\alpha_1\alpha_2}\right)\left(\frac{4}{C_p + C_v}\right)(K_{He}/\mu)(\lambda/\delta) \tag{3-29}$$

where:

α_1 is the accommodation coefficient of the fuel,
α_2 is the accommodation coefficient of the cladding,
C_p is the constant pressure heat capacity,
C_v is the constant volume heat capacity,
K_{He} is the gas thermal conductivity,
μ is the gas viscosity,
λ is the mean free path,
δ is the characteristic dimension (e.g., radial gap).

Assuming that [ ]^{a,c} and utilizing relationships from the [ ]^{a,c} it can be shown that Equation (3-29) reduces to:

$$f = 1 + \frac{\left[1.6787 \cdot 10^{-5}\left(\frac{2-A}{A}\right)K_{He}T^{1/2}\right]}{P_f\,\delta} \tag{3-30}$$

where:

K is in BTU/hr-ft-°F
T is the gap gas temperature in degrees Rankine,
P_f is the absolute gas pressure in psi,
δ is the radial gap in feet

and where A, the accommodation coefficient, is a function of pressure (Reference 3.17), as shown in Figure 3.5-1, and is given by:

$$[\qquad\qquad]^{a,c} \tag{3-31}$$

The effective thermal conductivity of helium used in Equation (3-26) accounts for the accommodation factor, so that:

$$K_{eff} = K_{He} / f \tag{3-32}$$

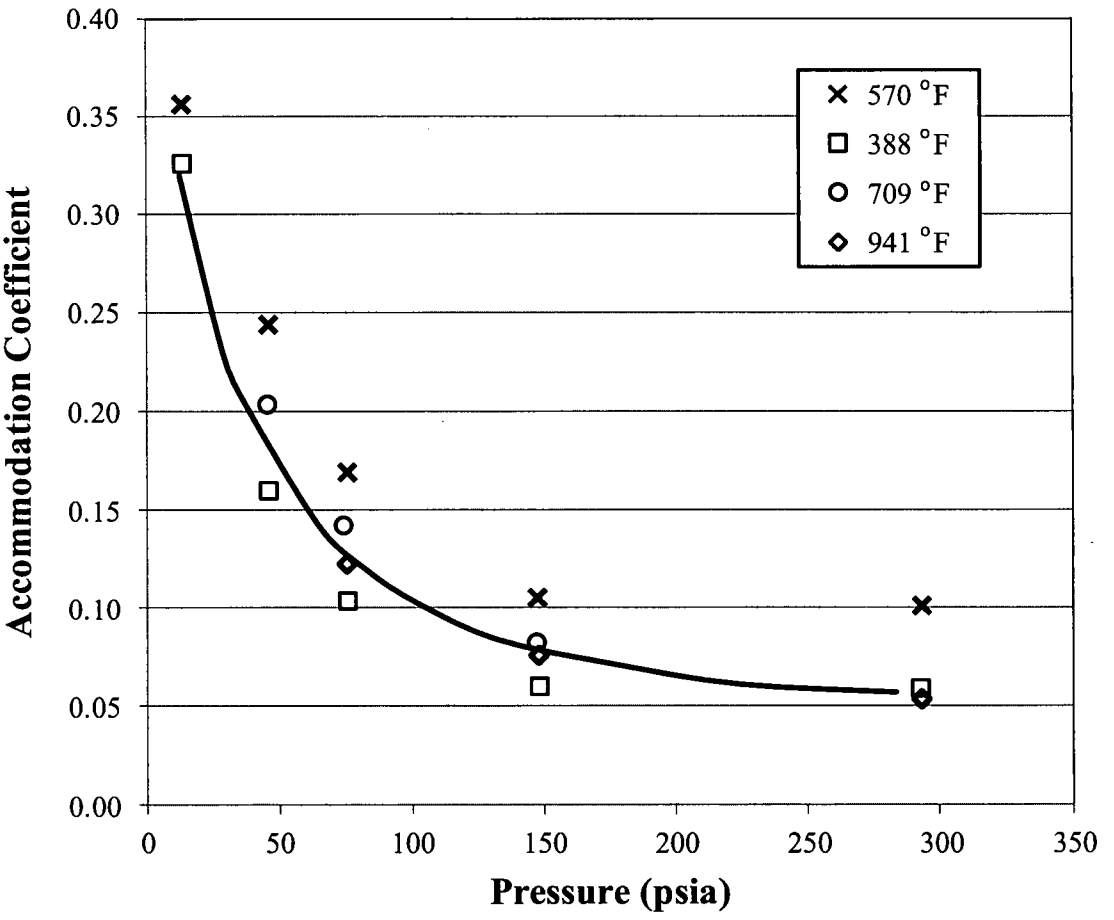

Figure 3.5-1 Variation in Accommodation Coefficient with Pressure (Reference 3.17)

3.5.4 Gap Conductance Used for Pellet-Clad Contact

This model is the same as that used in PAD 4.0 (Reference 3.1). Original documentation of this model is located in Reference 3.12.

When the pellet is in contact with the cladding, the PAD5 gap (contact) conductance is determined by:

$$\left[\right]^{a,c} \qquad (3\text{-}33)$$

where:

h_{gap} is the contact conductance (BTU/hr-ft^2-°F),
P_c is the contact pressure (psi), [ ]^{a,c}
K_{mix} is the thermal conductivity of the gas mixture (BTU/hr-ft-°F),
δ_r is the effective surface roughness (ft).

If the deformed cladding inner diameter is predicted to be radially inside of the deformed fuel diameter in a particular axial segment, i.e., an interference fuel-cladding gap, the fuel-cladding contact pressure is calculated based on the interference gap size assuming both the fuel and cladding are in the elastic state (see subsection 5.1.1).

Equation (3-33) is based on the work of [ ]^{a,c} and has been selected as a mean value between the published curves. The contact conductance described by Equation (3-33) is shown in Figure 3.5-2, and is compared to the published work. The adequateness of this selection is confirmed by the ability of the overall model to correlate the data.

a,c

Figure 3.5-2 Contact Conductance for UO_2-Zr at 500°F in Argon

3.6 FUEL TEMPERATURE DROP MODEL

This model is the same as that used in PAD 4.0 (References 3.1) and previous PAD versions (References 3.12, and 3.14). A brief description of this model is included below.

The fuel temperature profile across a fuel pellet, from the fuel surface to the fuel centerline, is calculated by solving the heat conduction equation for a cylindrical pellet (assuming radial heat flow) using [ ]^{a,c} method:

$$\left[\right]^{a,c} \tag{3-34}$$

where:

$K(T)$ is the fuel thermal conductivity, assumed to depend on temperature and burnup,
T_S is the temperature at the pellet surface,
$T(r)$ is the pellet temperature at radial position r,
R_S is the pellet radius at the outer surface,
$q''(r')$ is the heat flux at radial position r'.

The heat flux is calculated as:

$$q''(r') = \frac{1}{r'} \int_{R_{IN}}^{r'} q'''(r'')\, r''\, dr'' \tag{3-35}$$

where:

$q'''(r'')$ is the volumetric power density at pellet radius r''.

In PAD, the fuel pellet is divided into ten equal-volume radial rings. The volumetric power density in each ring is given by the pellet radial power distributions discussed in subsection 3.6.2.

The PAD code assumes that the burnup, fuel density, and volumetric power density in each radial ring are uniform over the ring. Using Equations (3-34) and (3-35), the value of [ ]^{a,c} is calculated for each ring. The [ ]^{a,c} correlation for the fuel thermal conductivity presented in subsection 6.1.2 is then solved for the temperature at each ring boundary.

3.6.1 Fuel Thermal Conductivity

This model is revised for PAD5. Original documentation of this model is located in Reference 3.14.

The fuel thermal conductivity model should account for the dependence of thermal conductivity on local fuel temperature and local burnup, as well as on the burnable absorber concentration [ ]^{a,c}. The model used in PAD5 has been updated to explicitly account for fuel thermal conductivity degradation with burnup and is described in subsection 6.1.2.

The fuel thermal conductivity model can be qualified directly, based on thermal conductivity data from laser flash thermal diffusivity measurements, and indirectly, based on measured fuel temperatures. The validation against measured fuel temperatures is presented in the thermal calibration results in Appendix A.

Figures 3.6-1 through 3.6-3 show plots of the fuel thermal conductivity of UO_2, gadolinia, and erbia fuel, respectively, as a function of temperature for various burnups. The plots have been extended to the melting point. The correlations for fuel thermal conductivity and fuel melting point from subsections 6.1.2 and 6.1.5, respectively, were used.

a,c

Figure 3.6-1 Thermal Conductivity for UO_2 Fuel at Various Burnups

a,c

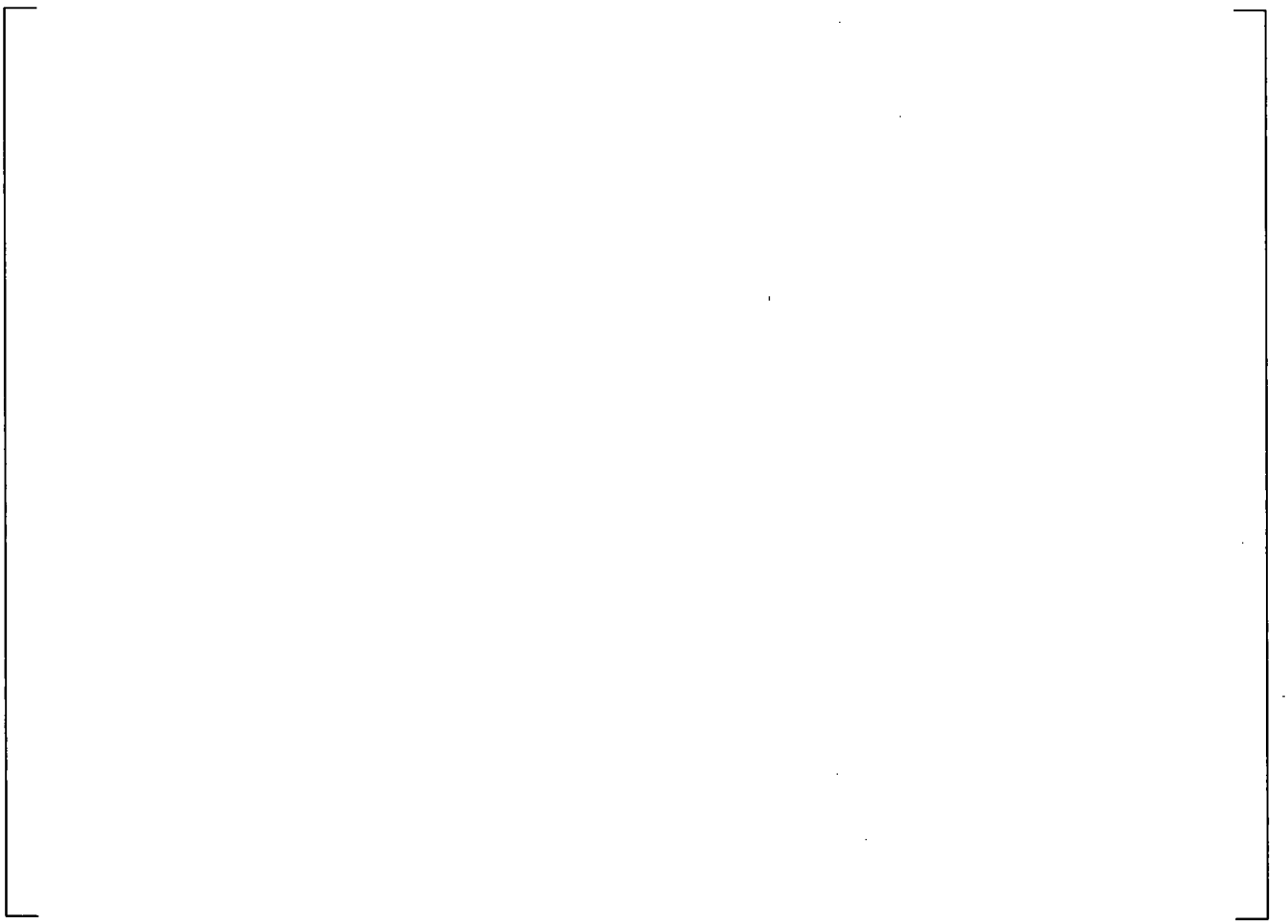

Figure 3.6-2 Thermal Conductivity for 8% Gadolinia Fuel at Various Burnups

a,c

Figure 3.6-3 Thermal Conductivity for 2.5% Erbia Fuel at Various Burnups

3.6.2 Pellet Radial Power Distribution Model

This model is revised for PAD5.

The radial power distribution (and the resulting radial power depression factor) in the PAD code is a function of [ ]^{a,c}. Local distributions are determined for each axial segment by a parabolic interpolation to data which are tabulated as a function of [ ]^{a,c}. It has been shown that these distributions [

]^{a,c}.

Radial power distributions can be accurately calculated by PARAGON (Reference 3.13) for various fuel types (UO_2, erbia, gadolinia, and ZrB_2-coated fuel), at various burnups, and for different reactor types.

Figures 3.6-4 through 3.6-7 show sample radial power distributions used in PAD5. Figure 3.6-4 displays radial power distributions for UO_2 fuel with 4.5% enrichment. Figure 3.6-5 presents graphs for radial power distributions for ZrB_2-coated fuel with 3% uranium enrichment. For this graph the focus is on

lower burnups, as the distributions approach those of pure UO_2 fuel at burnups starting from about 15 GWd/MTU. Figure 3.6-6 shows radial power distribution for 2.5% erbia fuel of 4% uranium enrichment, and Figure 3.6-7 shows radial power distributions for 8.1% gadolinia fuel of 4.5% uranium enrichment. PAD divides the pellet into ten equal-volume radial rings. In the graphs shown in Figures 3.6-4 through 3.6-7, ring number one corresponds to the innermost ring and ring number ten corresponds to the outermost ring.

a,c

Figure 3.6-4 Radial Power Distributions for 4.5% Enriched UO_2 Fuel at Various Burnups

a,c

Figure 3.6-5 Radial Power Distributions for ZrB_2-Coated 3% Uranium Enriched Fuel for Various Burnups

a,c

Figure 3.6-6 Radial Power Distributions for 2.5% Erbia Fuel with 4% Uranium Enrichment at Various Burnups

a,c

Figure 3.6-7 Radial Power Distributions for 8.1% Gadolinia Fuel with 4.5% Uranium Enrichment at Various Burnups

3.7 PLENUM TEMPERATURE MODEL

This model is the same as what was used in PAD 4.0 (Reference 3.1). Original documentation of this model is located in NS-SL-521 (Reference 3.2), Attachment M.

The plenum gas temperature calculation is based on the data obtained from two in-pile experiments. The first experiment was performed in the Organization for Economic Co-Operation and Development (OECD) Halden Boiling Heavy Water Reactor in Norway during the second half of 1968. The second experiment was performed in the Plutonium Recycle Test Reactor (PRTR) during several months of operation as part of the Plutonium Utilization Program at Pacific Northwest National Laboratory (PNNL). For both experiments, both internal gas pressure and plenum gas temperature were recorded during the irradiation period.

The plenum geometries, the axial heat flux distributions and the fuel rod characteristics were significantly different in the two experiments. However, it was possible to derive from these data a very simple relationship between the gas plenum temperature, the coolant temperature, and the fuel rod operating power. This relationship reveals that the plenum gas temperature is directly related to the surrounding coolant temperature and is a weak function of the fuel rod power. Although the plenum geometries in these two experiments are somewhat different from our reference fuel rod plenum geometry, this simple

model can be used to predict the operating plenum gas temperature in the Westinghouse fuel rods to a sufficient degree of accuracy.

The resulting equation is:

$$T_{plenum} = T_{coolant} + \overset{a,c}{\left[\quad\right]} \tag{3-36}$$

where:

T_{plenum} is the average temperature of the gas space in the plenum of a PWR fuel rod (°F),
$T_{coolant}$ is the rod coolant channel outlet temperature. (°F),
[

]^{a,c}

3.8 SECTION 3 REFERENCES

3.1 WCAP-15063-P-A Revision 1, with Errata, (Proprietary) and WCAP-15064-NP-A Revision 1, with Errata, (Non-Proprietary), "Westinghouse Improved Performance Analysis and Design Model (PAD 4.0)," July 2000.

3.2 NS-SL-521, NS-SL-524, and NS-SL-543, (Proprietary), and NS-SL-527, and NS-SL-544, (Non Proprietary), Supplemental information on fuel design transmitted from R. Salvatori, Westinghouse, to D. Knuth, AEC, January 1973.

3.3 WCAP-14565-P-A (Proprietary) and WCAP-15306-NP-A (Non-Proprietary) "VIPRE-01 Modeling and Qualification for Pressurized Water Reactor Non-LOCA Thermal-Hydraulic Safety Analysis," October 1999.

3.4 F. W. Dittus, and L. M. K. Boelter, "Heat Transfer in Automobile Radiators of the Tubular Type," University of California Publications in Engineering, Vol. 2, No. 13, pp 443-461, October 1930.

3.5 J. R. Thom, W. M. Walker, T. A. Fallon, G. F. S. Reising, "Boiling in Sub-cooled Water During Flow Up Heated Tubes or Annuli," Proc. Inst. Mech. Engrs., 1965-1966.

3.6 L. S. Tong, "Heat-Transfer Mechanisms in Nucleate and Film Boiling," Nuc. Engs. & Des., 21 (1972), 1-25.

3.7 WCAP-12610-P-A & CENPD-404-P-A, Addendum 2 "Westinghouse Clad Corrosion Model for ZIRLO™ and **Optimized ZIRLO™**," November 2008.

3.8 Letter from Sher Bahadur (US NRC) to James Gresham (Westinghouse), "Final Safety Evaluation for Westinghouse Electric Company (Westinghouse) Topical Report WCAP-12610-P-A & CENPD-404-P-A, Addendum 2/WCAP-14342-A & CENPD-404-NP-A, Addendum 2, 'Westinghouse Clad Corrosion Model for ZIRLO™ AND **Optimized ZIRLO™** ' (TAC Nos. ME0222 and ME2317)," July 18, 2013.

3.9 LTR-NRC-11-48, "Responses to NRC Request for Additional Information on WCAP-12610-P-A & CENPD-404-P-A Addendum 2, 'Westinghouse Clad Corrosion Model for ZIRLO and **Optimized ZIRLO™**,' (TAC No. ME0222) (Proprietary/Non-Proprietary)," September 19, 2011.

3.10 LTR-NRC-10-27," Responses to the NRC's Request for Additional Information RE: Westinghouse Electric Company Topical Report WCAP-12610-P-A & CENPD-404-P-A, Addendum 2 / WCAP-14342-A & CENPD-404-NP-A, Addendum 2, 'Westinghouse Clad Corrosion Model For ZIRLO™ and **Optimized ZIRLO™**' (TAC No. ME0222) (Proprietary/Non-Proprietary)," April 30, 2010.

3.11 NSD-NRC-97-4948 "Transmittal of Presentation Material," January 1979.

3.12 WCAP-8720 (Proprietary) "Improved Analytical Models Used in Westinghouse Fuel Rod Design Computations,"October 1976.

3.13 WCAP-16045-P-A (Proprietary) and WCAP-16045-NP-A (Non-Proprietary), "Qualification of the Two-Dimensional Transport Code PARAGON," August 2004.

3.14 WCAP-10851-P-A, (Proprietary) and WCAP-11873-A, (Non-Proprietary) "Improved Fuel Performance Models for Westinghouse Fuel Rod Design and Safety Evaluations," August 1988.

3.15 R. S. Brokaw, "Alignment Charts for Transport Properties, Viscosity, Thermal Conductivity and Diffusion Coefficients for Nonpolar Gases and Gas Mixtures at Low Density," Report NASA TR R-81, 1961.

3.16 E. H. Kennard, "Kinetic Theory of Gases," McGraw Hill, New York, 1938.

3.17 N. K. Zimina, "Combined Allowance for the Effect of Pressure and Accommodation Coefficient on the Thermal Conductivity of Light Gases at Elevated Pressures," Heat Transfer – Soviet Research, 6, No. 6, 57-65 (1974).

3.18 R. A. Dean, "Thermal Contact Conductance between UO_2 and Zircaloy-2," CVNA-127, May 1962.

3.19 A. M. Ross and R. L. Stoute, "Heat Transfer Coefficient between UO_2 and Zircaloy-2," Report AECL-1552, Chalk River Ontario, June 1962.

4 GAS RELEASE AND INTERNAL PRESSURE

Section 4 describes the PAD5:

- Fuel helium solubility model,
- ZrB_2 helium release model,
- Fission gas release model,
- Free gas equation of state,
- Cladding gas absorption, and
- Open void volume and rod internal pressure models.

4.1 HELIUM SOLUBILITY AND RELEASE

This model is the same as in PAD 4.0 (Reference 4.1). Original documentation of this model is located in PAD 3.3 (Reference 4.2).

Following initial manufacturing, the fuel pellets in fuel rods containing pressurized helium are assumed to absorb a portion of the helium atmosphere within a short period of time. During operation an additional 0.3 atoms of helium are produced for every 100 fissions and a portion of the produced helium is released.

Review of published literature indicates that dissolution of helium into UO_2 occurs to a small extent. Westinghouse has carried out tests to determine the extent of helium dissolution in UO_2 during irradiation in helium pressurized fuel rods. Knowledge of the extent of dissolution of helium is important in calculating fuel rod internal pressures.

Data from 90% Theoretical Density (T.D.) and 95% T.D. fuel irradiated in the Plant AA reactor to burnups between 1000 and 5000 MWd/MTU (Table 4.1-1) and higher burnup data for fuel between 91.5% T.D. and 96.0% T.D. (Table 4.1-2) have been fit with a standard multiple linear regression equation to obtain the helium solubility equation used in the PAD5 code:

$$S = [\qquad\qquad\qquad\qquad\qquad\qquad]^{a,c} \qquad (4-1)$$

where:

S	is the helium solubility, (cc (STP)/gm UO_2)
ρ_0	is the initial fuel density, (% T.D.)
P_0	is the initial gas pressure, (psia)
BU	is the fuel burnup, (MWd/MTU)

Table 4.1-3 compares the predicted and measured solubility data using this equation.

The use of the helium content (solubility) equation in design consists essentially of the following steps.

- The extent of helium dissolution is calculated for the initial fuel density assuming dissolution to be complete at the beginning of irradiation.

- The initial backfill pressure is calculated to be consistent with the loss of helium due to solution. The internal gas pressure (P) is then given by:

$$P = P_O - \Delta P_S \tag{4-2}$$

where:

P_O is the initial fill pressure
ΔP_S is the pressure reduction due to the initial absorption of helium.

- At any point during irradiation the helium content in the fuel is re-evaluated using Equation (4-1) and assuming that helium produced by fissioning is 0.30 atoms/100 fissions. Thus at any time:

$$H_R = S_O + H_p - S(t) \tag{4-3}$$

and the fractional release (relative to the total) is:

$$F_H = \frac{H_R}{S_O + H_P} \tag{4-4}$$

where:

$S(t)$ is the helium content at any time
S_O is the initial helium absorbed into the fuel
H_R is the helium release during irradiation
H_p is the helium produced by fissioning.

Figure 4.1-1 illustrates how the helium content varies as a function of density and burnup.

The helium which has been released from the fuel (H_R) increases the internal gas pressure proportionally.

Table 4.1-1 Plant AA Helium Solubility Data

Rod Identification	Fuel Density (%T. D.)	Design Pressure (psia)	Burnup (MWd/MTU)	Helium Content (cc/gm)
(1) 506-A1	90.1	720	4600	[
(2) 506-A2	90.1	720	4600	
(3) 506-B1	90.2	720	3300	
(4) 506-B2	90.2	720	3300	
(5) PM-1	94.7	500	3310	
(6) PM-2	94.7	500	3500	
(7) PM-3	94.7	500	3350	
(8) PM-4	94.7	500	3500	
(9) PM-5	94.7	500	1070	]

a,b,c

Table 4.1-2 Plant A and Plant Z Helium Solubility Data

Rod Identification	Fuel Density (% T. D.)	Design Pressure (psia)	Burnup (MWd/MTU)	Helium Content (cc/gm)
(1) Plant A 007-110	96	600	14030	[
(2) Plant A 007-4.5	96	600	7788	
(3) Plant A 013-110	96	380	10707	
(4) Plant A 11-110	94	200	13774	
(5) Plant A/3/C18-H1-1A	91.5	275	23500	
(6) Plant A /3/C18-H1-1B	91.5	275	23500	
(7) Plant A /3/C18-J5-1A	91.5	275	22600	
(8) Plant A /3/C18-J5-1B	91.5	275	22600	
(9) Plant Z 285/75-76	94.6	500	31000	
(10) Plant Z 285/75-76	94.6	500	31000	
(11) Plant Z 285/9.9-10.4	94.6	500	30000	
(12) Plant Z 285/4.8-5.2	94.6	500	25000	]

a,b,c

Table 4.1-3 Comparison of Predicted and Measured Helium Solubility Data

Data Point	Helium Content (cc/gm)	
	Predicted	Measured
Table 4.1-1 (1)		
Table 4.1-1 (2)		
Table 4.1-1 (3)		
Table 4.1-1 (4)		
Table 4.1-1 (5)		
Table 4.1-1 (6)		
Table 4.1-1 (7)		
Table 4.1-1 (8)		
Table 4.1-1 (9)		
Table 4.1-2 (1)		
Table 4.1-2 (2)		
Table 4.1-2 (3)		
Table 4.1-2 (4)		
Table 4.1-2 (5)		
Table 4.1-2 (6)		
Table 4.1-2 (7)		
Table 4.1-2 (8)		
Table 4.1-2 (9)		
Table 4.1-2 (10)		
Table 4.1-2 (11)		
Table 4.1-2 (12)		

a,b,c

a,b,c

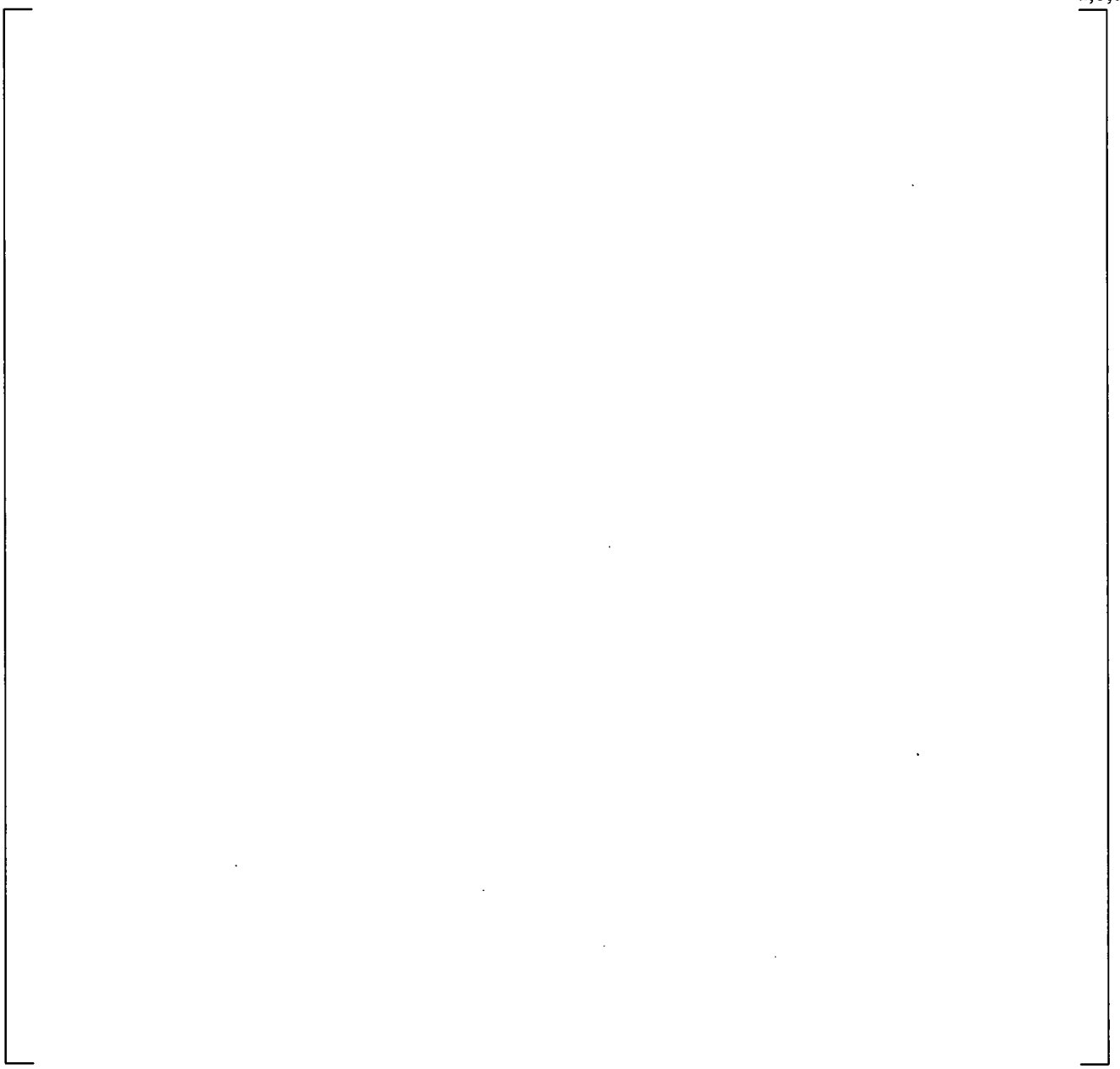

Figure 4.1-1 Comparison of Predicted and Measured Helium Content

4.2 HELIUM RELEASE (ZIRCONIUM DIBORIDE)

The helium generation from ZrB_2 is the same as in PAD 4.0. The helium release model for ZrB_2 is revised for PAD5.

4.2.1 Background and Helium Release Data

Helium generation from the ZrB_2 coating is equal to the Boron-10 (B^{10}) depletion of the boron coating. The model for the fractional B^{10} depletion of boron coated pellets is

[ ]^{a,c} (4-5)

where:

B_{10} = fraction remaining of B^{10}
the units of Rod Burnup are GWd/MTU
the units of Enrichment are weight percent
the constants are [ ]^{a,c}

The ZrB_2 helium release model in PAD 4.0 conservatively assumes [
]^{a,c} for best estimate results since the licensing of the Vantage 5 fuel assembly in Reference 4.3. This model is largely based on results from early [

]^{a,c}.

There are helium release data from [

]^{a,c}

A recent Halden test has allowed a better understanding of the magnitude and trend of the release during the time of helium production and after the completion of the production. Two rods with ZrB_2 coating [ ]^{a,c}. The fraction of helium gas released from the ZrB_2 coating was determined to be around [

]^{a,c}

[

]a,c

Table 4.2-1 Boron Coated Fuel Helium Release Data from LTA Programs							
Test Number	Plant	Thickness (mil)	B^{10} Enrichment (%)	Percent B (%)	Helium Release (Fraction)	Burnup (GWd/MTU)	Time (hrs)

a,b,c

Table 4.2-1 (cont.) Boron Coated Fuel Helium Release Data from LTA Programs

Test Number	Plant	Thickness (mil)	B^{10} Enrichment (%)	Percent B (%)	Helium Release (Fraction)	Burnup (GWd/MTU)	Time (hrs)

a,b,c

a,b,c

Figure 4.2-1 Helium Release Fraction as Function of Irradiation Time

4.2.2 ZrB_2 Helium Release Model

The temperature of the ZrB_2 coating was maintained at [ ]^{a,c} which is higher than the temperature of the ZrB_2 coating expected in normal commercial reactor operation. While the absolute helium release fraction may vary in the Halden test rod due to this temperature difference, the helium release trend and the time-dependence indicated by the Halden data should be applicable to commercial fuel rods with ZrB_2 coated pellets.

From Beginning of Life (BOL) to the time the helium release reaches a maximum release fraction, the release fraction as a function of time can be modeled as three linear segments – the Best Estimate (BE) model shown in Figure 4.2-2. [

]^{a,c}

[

]a,b,c

a,b,c

Figure 4.2-2 ZrB_2 Helium Release Model and Data

In summary, the proposed helium release fraction model as a function of irradiation time for PAD5 is [

]a,c

4.3 FISSION GAS RELEASE MODEL

The model function form for the thermal release was developed as part of PAD 3.4 (Reference 4.4). The model continued to be used in PAD 4.0 (Reference 4.1). The coefficients for the thermal release model are recalibrated with an updated database. [
]^{a,c}

A two component gas release model is used to describe the fission gas release, with one component giving the gas release from the high fuel temperature regions of the high power rods and the second component giving the major contribution to the gas release from the lower power rods and the cooler outer regions of the fuel rods. The fission gas release model is based on a fission gas production rate of 30 atoms per 100 fissions.

4.3.1 Thermal Fission Gas Release Model

The high temperature gas release model is based on concepts drawn from mechanistic models of high temperature gas release through interlinking of grain edge fission gas bubbles. Fission gas produced in the interior of the fuel grains migrates to the grain boundaries by diffusion or grain boundary sweeping, depending on the local fuel temperature. Fission gas bubbles form on the grain boundaries and a saturated gas bubble density develops on the grain edges as irradiation continues. Eventually the grain edge bubbles interlink, and the fission gas stored in the bubbles is vented to the fuel rod void volume. An equilibrium release rate is eventually established such that the net gas release rate equals the fission gas production rate.

The functional form of the thermal fission gas release model developed in Reference 4.4 is a phenomenological model based on the irradiation dependence of the gas release from mechanistic gas release models for the diffusion of the fission gas generated in the fuel grains to the grain boundaries, formation of fission gas bubbles on the grain boundaries, and release of the fission gas when these grain boundary bubbles interlink. At low fuel temperatures the grain boundary bubbles do not form, since the gas diffusion rates are very low, and no fission gas is released by this gas release mechanism. At higher fuel temperatures, grain boundary gas bubble formation and grain boundary gas bubble interlinking occurs. There is a delay in the gas release at the higher fuel temperatures to account for the time needed for the grain boundary bubbles to form and interlink. This delay decreases with increasing temperature, as the gas diffusion rates increase, and at very high fuel temperatures the thermal fission gas release is virtually instantaneous. The principal feature of this gas release model is that fission gas is released as fast as it is produced once a burnup threshold is reached. To give a smooth variation in the thermal fission gas release, a transition region is used through which the gas release rate varies continuously between no thermal gas release at low temperatures to a release rate equal to the fission gas production rate at high temperatures.

The temperature dependence of the fission gas release model burnup thresholds is determined by fitting the model with the fission gas release data. The burnup thresholds are shown in Figure 4.3-1. The burnup thresholds B_{INC} (for incubation) and B_{REP} (for Release Equal Production) are defined as functions of the local temperature T, in K, by pairs of burnup and temperature values, with the threshold curves given by:

[a,c] (4-6)

The burnups (in MWd/MTU) and temperatures (in K) defining the inflection points for the B_{INC} and B_{REP} curves are:

[

]a,c

The fractional gas release in the three regions shown in Figure 4.3-1 are given by:

[a,c] (4-7a)

[a,c] (4-7b)

[a,c] (4-7c)

where:

$R_{thermal}$ is fractional thermal fission gas release
B is the local burnup (MWd/MTU)
and B_{REP} and B_{INC} are calculated from the current local temperature.

Equation (4-7b) is a simple interpolation formula between no release for burnup less than B_{INC} to release equal to production for burnup greater than B_{REP}, with the constants chosen so that the fractional release $R_{thermal}$ is a continuous function of burnup.

For time dependent fuel temperatures, the thermal fission gas release model is applied by assuming that the thermal fission gas release is path independent when the fuel temperatures increase, so that there is rapid release of stored fission gas when the fuel temperatures increase. When the fuel temperatures decrease, there is no change in the amount of fission gas that has been released until the burnup reaches a value where the model predicts additional fission gas release at the lower temperature. Though the fractional thermal fission gas release will decrease with decreasing temperatures, the total amount of fission gas released will either remain constant or increase.

Because of the path independence of the steady-state thermal fission gas release with increasing temperatures, a transient fission gas release model is used to obtain the fission gas release during short duration overpower transients. The transient fission gas release model is given by:

$$R_{transient}(t) = f(t)R_{thermal} \tag{4-8}$$

where f(t) is an approximation of the Booth expression (Reference 4.5) for the diffusion of the fission gas in the fuel grain to the grain boundary:

[ ]^{a,c} (4-9a)

[ ]^{a,c} (4-9b)

where:

τ = $D_{Xe}t/XDIFF^2$

D_{Xe} is the Xenon diffusion coefficient (cm^2/sec)

t is the time (sec)

XDIFF is an effective grain radius (cm), [ ]^{a,c}

and the Xenon diffusion coefficient, (Reference 4.6), is:

$$D_{Xe} = 7.6x10^{-6}\exp(-35000/T) + 1.41x10^{-18}\phi^{1/2}\exp(-13800/T) + 2x10^{-30}\phi \tag{4-10}$$

where:

T is the local temperature (K)
ϕ is the local fission rate (fissions/cm^3-sec)

The f(t) transient factor is always used in calculating the thermal fission gas release. It has a relatively minor impact on the thermal fission gas release fractions calculated during steady state operation, where the fuel operates at effectively constant temperatures for a sufficiently long time for f(t) to reach its asymptotic value, f(t) = 1.

[

]^{a,c}

a,b,c

Figure 4.3-1 B_{REP} and B_{INC} Burnup Dependence

4.3.2 Athermal Fission Gas Release Models

Two models are used for the athermal fission gas release at low fuel temperatures. At all fuel burnups, there is a relatively small amount of fission gas release due to recoil and knockout. The fission gas release fraction due to knockout and recoil, R_{KOR}, is given by:

$$[\qquad\qquad]^{a,c} \tag{4-11}$$

where:

Bu_{loc} is the fuel local radial burnup (MWd/MTU) and
$[\qquad\qquad]^{a,c}$

In addition, a significant increase in the fission gas release of rods that operated at relatively low power at high burnups has been measured. The fuel temperatures achieved for this fuel during high burnup operation are too low for there to be any significant release due to the thermal fission gas release effects included in the PAD5 thermal fission gas release model.

To account for this enhanced athermal fission gas release at high burnup, an enhanced athermal fission gas release fraction, $R_{ath,enh}$, is calculated:

$$[\qquad\qquad]^{a,c} \tag{4-12a}$$

$$[\qquad\qquad]^{a,c} \tag{4-12b}$$

where Bu_{loc} is the fuel radial local burnup, in MWd/MTU, and Bu_{enh} is the threshold burnup for the enhanced athermal fission gas release, in MWd/MTU. The value of these model constants for the high burnup enhanced athermal fission gas release are:

$$[\qquad\qquad]^{a,c}$$

4.4 EQUATION OF STATE (EOS) MODEL

This model is the same as in PAD 4.0 (Reference 4.1).

4.4.1 Background

The relationship between pressure, temperature, and mass for the fill gas or fission gas in PAD 3.4 (Reference 4.4) and earlier models was based on the Ideal Gas Law. The Ideal Gas Law relationship is valid for many gases near room temperature and pressure, and is good for noble gases such as helium, neon, and argon up to moderate pressures (400–500 psia). At high pressures (P > 500 psia) however, the

Ideal Gas Law becomes increasingly inaccurate. Figure 4 from Chapter VII of Reference 4.7 shows that above about 500 psia, inert gases do not exhibit ideal behavior. At end of life, when the rod internal pressure can exceed 2000 psia, none of these gases will exhibit ideal behavior. Therefore, use of the Ideal Gas Law to estimate rod pressure given the temperature and specific volume will be inaccurate.

A survey was conducted to determine the most appropriate EOS. It was determined that the Peng-Robinson equation, (Reference 4.8), gave the most accurate predictions for the range of interest. However, this EOS consistently under predicts the measurements over the whole range of helium mole fraction. A positive aspect of this EOS is that the prediction error is insensitive to the helium concentration, thus leading to the following (calibrated) gas EOS:

$$P^c = \alpha P \tag{4-13}$$

where P^c is the corrected or calibrated Peng-Robinson gas EOS, P is the original Peng-Robinson gas EOS, and [ ]^{a,c} is a correction factor determined from the data depicted in Figure 4.4-1, which shows the prediction error DP/P as defined below as a function of helium mole fraction for the corrected Peng-Robinson EOS. The prediction errors are very balanced and range between -2% and 2%.

For fission gas mixtures even at end of life, helium generally has the highest mole fraction. Measured data was obtained from References 4.9 through 4.13 for the various gas matrix evaluations.

DP/P is defined as:

$$\frac{DP}{P} = \frac{P_{predicted} - P_{measured}}{P_{measured}} \tag{4-14}$$

This quantity is positive when the pressure is over predicted, and negative when under predicted.

The calibrated Peng-Robinson EOS performs well at high He composition. Figure 4.4-2 shows the calibrated Peng-Robinson Predicted vs. Measured plot results for various pressures.

a,c

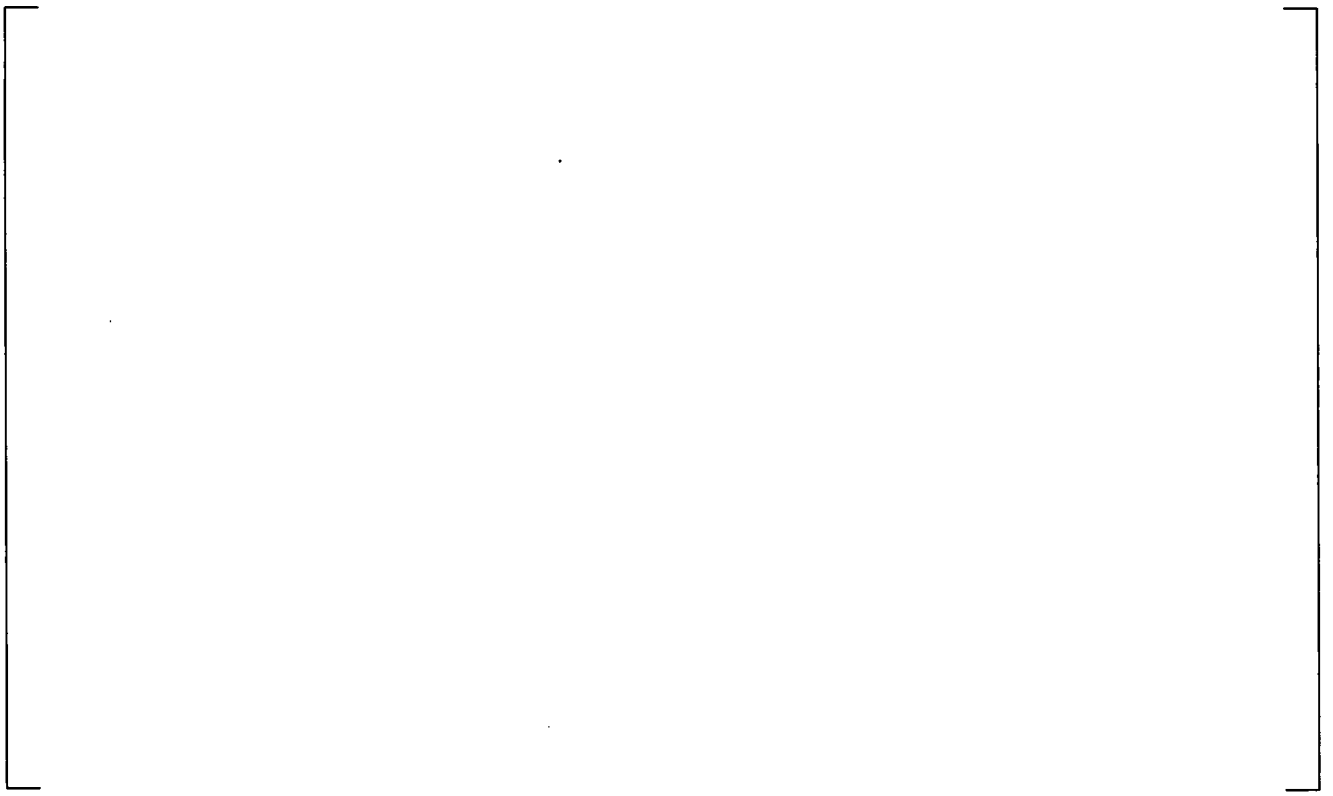

Figure 4.4-1 Calibrated Peng-Robinson Equation of State DP/P versus Helium Mole Fraction

a,c

Figure 4.4-2 Calibrated Peng-Robinson Equation of State Predicted versus Measured Pressure

In summary, the Ideal Gas Law was found to potentially underpredict pressure for compositions with high helium mole fraction and the Peng-Robinson EOS was found to better fit measured data.

4.4.2 EOS Model

The pressure-temperature-volume relationship for a pure fluid is often represented by a cubic Equation of State, which has the general form:

$$P = \frac{RT}{v-b} - \frac{a}{v^2 + ubv + wb^2} \tag{4-15}$$

where P is the pressure, T is temperature, v is specific volume, and R is the Universal Gas constant.

For the Peng-Robinson equation of state, u = 2 and w = -1 with:

$$b = \frac{0.07780RT_c}{P_c} \tag{4-16}$$

and:

$$a = \frac{0.45724R^2T_c^2}{P_c}[1 + f\omega(1 - T_r^{0.5})]^2 \quad (4\text{-}17)$$

where:

$$f\omega = 0.37464 + 1.54226\omega - 0.26992\omega^2 \quad (4\text{-}18)$$

In Equations (4-16) and (4-17), the subscript "c" denotes properties at the critical point. The reduced temperature is defined as:

$$T_r = \frac{T}{T_c} \quad (4\text{-}19)$$

The function for fω given by Equation (4-18) uses the acentric factor ω, which is a parameter that represents the complexity of a molecule with respect to geometry and polarity. For mono-atomic gases, ω is usually zero or very small.

In the PAD5 code up to eight different gases can be present in the gas mixture. Table 4.4-1 lists these components and the properties assigned in the code as taken from Reference 4.8.

Table 4.4-1 Pure Gas Component Properties List for PAD5

Component	T_c (K)	P_c (bar)	ω
Helium	5.19	2.27	-0.365
Xenon	289.7	58.4	+0.008
Krypton	209.4	55.0	+0.005
Argon	150.8	48.7	+0.001
Nitrogen	126.2	33.9	+0.039
Water Vapor	647.3	221.2	+0.344
Hydrogen	33.2	13.0	-0.218
Oxygen	154.6	50.4	+0.025

For gas mixtures, the attraction and repulsion between molecules of different components causes non-linear variation of some properties with composition. To account for this in Equation (4-15), a set of mixing rules can be defined to this non-linearity. The values of "a" and "b" in Equation (4-15) are re-defined. Based on the recommendations in Reference 4.8, the following mixing rules are used in the PAD5 code:

$$a_m = \sum_i \sum_j y_i y_j \left(a_i a_j\right)^{0.5}\left(1 - k_{ij}\right) \quad (4\text{-}20)$$

$$b_m = \sum_i y_i b_i \quad (4\text{-}21)$$

The b_i and a_i for each pure component are given by Equations (4-16) and (4-17) respectively. The term k_{ij} is used for some binary pairs to adjust for strong interactions and is determined from experimental data. In the PAD5 code $k_{ij} = 0$, is assumed for all binary combinations.

4.5 GAS ABSORPTION IN CLADDING EFFECT

This model is the same as in PAD 4.0 (Reference 4.1).

The fuel rod internal free gas mixture includes: (1) the fission gases produced during operation, (2) gas from the pellets including the gas from the ZrB_2 coating if present, (3) the gas from the rod pre-pressurization, and (4) the [ ]^{a,c}. When the rod is pre-pressurized and sealed during fabrication, the rod [ ]^{a,c}. Zirconium alloys are known to react with [ ]^{a,c}.

For example, assuming a plenum volume of about [ ]^{a,c} and a gas mixture of [ ]^{a,c}. With about [ ]^{a,c} the corresponding weight gain for total [ ]^{a,c}. Based on reaction rates in Reference 4.15, [ ]^{a,c} will occur within [ ]^{a,c}. Thus, all of the [ ]^{a,c}.

Zirconium preferentially reacts with [ ]^{a,c} are present. When the [ ]^{a,c} The absorption rate of [ ]^{a,c}. Based upon the weight of [ ]^{a,c}. Thus, it will take about [ ]^{a,c}. This may be a lower than actual rate since the rate is temperature dependent. [ ]^{a,c}

Irradiated rods were punctured in the hot cell and the gas present in the rod was captured and analyzed. In the 22 Plant B rods measured and in 7 other rods from Plant C and Plant D, there was [ ]^{a,b,c}. The measurement sensitivity is reported as less than 0.01% by volume. If the [ ]^{a,c} pressurization and a resultant internal rod gas mixture with [ ]^{a,c} by volume. These levels, if present in the rod at end of life, are above the detection limit by a factor of over 100.

These evaluations indicate that the [ ]^{a,c} the Zircaloy-4, ZIRLO, or **Optimized ZIRLO** cladding microstructure, and [ ]^{a,c}. Therefore, PAD5

does not account for [
]^{a,c}.

4.6 VOID VOLUMES AND INTERNAL PRESSURE

This model has minor updates to what was used in PAD 4.0 (Reference 4.1). Original documentation for the model is located in NS-SL-521 (Reference 4.16 Attachment C). PAD5 updates the crack volume and the gap volume due to the pellet relocation model. The central hole volume for the annular pellets was also modeled in PAD 4.0, but was not discussed in the PAD 4.0 topical report.

The fuel rod void volume at power is the sum of the following void components:

- Plenum volume
- Dish volume
- Fuel-clad gap volume
- Crack volume
- Open porosity volume
- Fuel pellet surface imperfection volumes
- Central hole volume for annular pellets

Plenum volume is calculated from the initial clad, fuel, and spring dimensions and subsequently accounts for temperature and irradiation effects (such as clad growth and fuel swelling).

The dish volume is calculated at any given power and time by applying the appropriate thermal expansion and fuel swelling to ten radial rings, recalculating the shape of the pellet, and then summing up the volume at the pellet end face.

The fuel-clad gap volume is calculated by subtracting a pellet cross-sectional area based on radial fuel pellet expansion due to fuel densification, swelling, thermal expansion, and pellet relocation, from a cladding ID cross-sectional area which includes the effects of elastic and plastic cladding deformation.

The crack volume, as a result of pellet cracks from the thermal stress, is calculated at any given power and time by applying the linear thermal expansion to ten radial rings (appropriate to its average temperature), calculating the pellet volume based on the pellet radius, and then subtracting the sum of the volumetric expansions of each ring. [
]^{a,c}

[
]^{a,c}

a,c

$$\left[\qquad\qquad\right] \tag{4-22}$$

where j is the axial section index, Δl_j is the height of the axial section, DP_{hot} is the hot pellet diameter, and δD_{reloc} is the diametral relocation . $\Delta V_{reloc,j}$ is added to the pellet crack volume in each axial section.

The open porosity volume is calculated as a function of initial fuel density and fuel temperature at power. The open porosity at room temperature is:

[ ]^{a,c} (4-23)

where ρ_0 is geometric density in % T.D. The above relationship was obtained from open porosity measurements on a large number of unirradiated production fuel pellets.

The open porosity dependence on temperature, T, is calculated as follows:

[

]^{a,c}

Fuel pellet surface imperfection volume is the difference between the geometric and true density. It has been determined to be [ ]^{a,c} of the fuel volume, based on a large number of measurements on unirradiated production pellets.

The central hole volume for the annular pellets is calculated from the initial central hole volume and subsequently accounts for temperature and irradiation effects (such as fuel thermal expansion and fuel swelling and densification).

All the volumes thus calculated are summed to give the total fuel rod internal void volume.

Rod internal pressure is calculated using the Peng-Robinson EOS discussed in Section 4.4. The various volumes and the corresponding temperatures used in the equation are:

a,c

Plenum volume	[ ]
Dish volume	
Fuel-clad gap volume	
Crack volume	
Open porosity volume	
Fuel pellet surface imperfection volumes	
Central hole volume for annular pellet	

4.7 SECTION 4 REFERENCES

4.1 WCAP-15063-P-A Revision 1, with Errata (Proprietary) and WCAP-15064-NP-A Revision 1, with Errata, (Non-Proprietary), "Westinghouse Improved Performance Analysis and Design Model (PAD 4.0)," July 2000.

4.2 WCAP-8720 (Proprietary), "Improved Analytical Models Used in Westinghouse Fuel Rod Design Computations," October 1976.

4.3 WCAP-10444 Addendum 1-A, "Reference Core Report Vantage 5 Fuel Assembly Addendum 1," March 1986.

4.4 WCAP-10851-P-A, (Proprietary) and WCAP-11873-A, (Non-Proprietary), "Improved Fuel Performance Models for Westinghouse Fuel Rod Design and Safety Evaluations," August, 1988.

4.5 A. H. Booth, "A Method of Calculating Fission Gas Diffusion from UO_2 Fuel and its Application to the X-2-f Loop Test", CRDC-721 (AECL 496) September 1957.

4.6 A. D. Appelhans and J. A Turnbull, "Measured Release of Radioactive Xenon, Krypton, and Iodine from UO_2 at Typical Light Water Reactor Conditions, and Comparison with Release Models," NUREG/CR-2298, EGG-2124, November 1981.

4.7 G. A. Cook, "Argon, Helium, and the Rare Gases," Interscience Publishers, New York, 1961.

4.8 R. C. Reid, J. M. Prausnitz, and B. Poling, "The Properties of Gases and Liquids," 4th Ed., McGraw Hill, 1987.

4.9 J. M. Gandhi and S. C. Saxena, "Correlated Thermal Conductivity Data of Rare Gases and their Binary Mixtures at Ordinary Pressures," Journal of Chemical and Eng. Data, Vol. 13, No. 3, July 1968.

4.10 J. J. Hurley, et al., "Virial Equation of State of Helium, Xenon, and Helium-Xenon Mixtures from Speed of Sound and Burnett PrT Measurements," International Journal of Thermophysics, Volume 18, No.3, May 1997.

4.11 R. D. McCarty, "Thermophysical Properties of Helium-4 From 2 to 1500K With Pressures to 1000 Atmospheres," COM 75-10334, National Bureau of Standards, Nov. 1972.

4.12 Matheson, Gas Data Book, 6th Ed.

4.13 T. C. Briggs, and A. R. Howard, "Compressibility Data for Helium, Nitrogen, and Helium-Nitrogen Mixtures at 0°, 25°, and 50°C and at Pressures to 1000 Atmospheres," Bureau of Mines Report of Investigations 7639, 1972.

4.14 Handbook of Chemistry and Physics, 54 Edition, page F-191.

4.15 Lustman and Kerze, "The Metallurgy of Zirconium," McGraw-Hill Book Company, Inc., 1955, pages 578-608.

4.16 NS-SL-521, NS-SL-524, and NS-SL-543, (Proprietary), and NS-SL-527, and NS-SL-544, (Non Proprietary), Supplemental information on fuel design transmitted from R. Salvatori, Westinghouse, to D. Knuth, AEC, January 1973

5 CLAD AND FUEL DEFORMATION MODELS

Section 5 begins by describing the PAD5 cladding models for:

- Clad stresses, including fuel-cladding contact pressure, differential pressure stresses, stress for clad creep and plasticity analysis, and thermal stresses,
- Clad elastic deformation,
- Clad plasticity,
- Clad creep, and
- Clad diametral growth.

Following a description of these cladding models, Section 5 then describes fuel models for:

- Fission gas bubble swelling,
- Fuel swelling and densification, and
- Fuel relocation

Lastly, the fuel rod cladding axial growth model is described. Clad and fuel thermal expansion models are described in subsections 6.3.3 and 6.1.3, respectively.

5.1 CLAD STRESSES

5.1.1 Fuel – Clad Interference Gap and Contact Pressure

This model is the same as in PAD 4.0 (Reference 5.1) except that the fuel relocation deformation is considered in the interference gap in PAD5.

The fuel-clad gap is determined by first radially deforming both the fuel and cladding. The cladding is radially deformed considering thermal expansion (subsection 6.3.3), elastic deformation in response to the rod internal pressure and coolant pressure (Section 5.2), creep (Section 5.4), clad diametral growth (Section 5.5), and plastic deformation (Section 5.3). The fuel is radially deformed considering thermal expansion (subsection 6.1.3), relocation (Section 5.6), fuel densification and swelling (Section 5.7), and high temperature fission gas bubble swelling (Section 5.8).

If the deformed cladding inner diameter is predicted to be radially inside of the deformed fuel diameter in a particular axial segment, i.e., an interference fuel-cladding gap, the fuel-cladding contact pressure is calculated based on the interference gap size. The interference gap, GAP, is represented as a positive quantity for this calculation. The fuel-cladding contact pressure is calculated assuming both the fuel and cladding are in the elastic state. The contact pressure is given by:

a,c

[ ] (5-1)

where:

P_{ct} is the contact pressure (psi)

GAP is the diametral interference (in)
R_i is the clad inside radius (in)
E is Young's Modulus (psi)
μ is Poisson's Ratio
K_c is the cladding radius ratio, R_o/R_i
and the subscripts c and p refer to cladding and fuel pellet, respectively.

Some deformations (for example, fuel relocation, clad plasticity, and cladding creep) may depend on the calculated stress or contact pressure. These deformations and the contact pressure for a give time step have to be solved iteratively. The solution procedure is summarized in Section 2.1.

5.1.2 Cladding Stresses from Differential Pressure

This model is the same as in PAD 4.0 (Reference 5.1).

The cladding stresses are calculated assuming no interaction between the axial segments in the fuel rod geometry. For elastic analysis, the cladding stresses for radial, hoop and axial directions are:

a,c

(5-2a)

a,c

(5-2b)

a,c

(5-2c)

where:

σ_r = radial stress (psi)
σ_θ = hoop stress (psi)
σ_z = axial stress (psi)
P_{gas} = rod internal pressure (psi)
P_{sys} = coolant system pressure (psi)
P_{con} = pellet-cladding contact pressure (psi)
R_o = cladding outer radius prior to accounting for elastic strains (in)
R_i = cladding inner radius prior to accounting for elastic strains (in)
K_c = R_o/R_i.

The radial and hoop stresses depend on the radial position 'R' in the cladding wall, and the axial stress is constant across the cladding wall.

5.1.3 Stress for Clad Creep and Plasticity Analysis

This model is new for PAD5.

PAD5 uses the Prandtl-Reuss flow rule to calculate the cladding hoop creep and plastic strain increments, with the stresses calculated at the cladding mid-wall:

$$\delta\varepsilon_\theta = \frac{\delta\varepsilon_{eff}}{\sigma_{eff}}\sigma_{\theta,d} \tag{5-3}$$

where:

$\delta\varepsilon_\theta$ = hoop strain increment (in/in)
$\delta\varepsilon_{eff}$ = effective strain increment, calculated from the creep rate model (in/in)
σ_{eff} = effective stress (psi or MPa)
$\sigma_{\theta,d}$ = hoop deviatoric stress (psi or MPa)

with:

$$\sigma_{\theta,d} = \sigma_\theta - 1/2(\sigma_r + \sigma_z)$$

and:

$$\sigma_{eff} = \frac{1}{\sqrt{2}}\left[(\sigma_\theta - \sigma_r)^2 + (\sigma_r - \sigma_z)^2 + (\sigma_z - \sigma_\theta)^2\right]^{1/2} \tag{5-4}$$

This flow rule can be generalized to calculate the hoop, radial, and axial creep and plasticity strain increments, using the definitions:

$$\sigma_{\theta,d} = \sigma_\theta - 1/2(\sigma_r + \sigma_z) \tag{5-5a}$$

$$\sigma_{r,d} = \sigma_r - 1/2(\sigma_\theta + \sigma_z) \tag{5-5b}$$

$$\sigma_{z,d} = \sigma_z - 1/2(\sigma_r + \sigma_\theta) \tag{5-5c}$$

With these definitions,

$$\sigma_{eff} = \sqrt{\frac{2}{3}}\left[\sigma_{\theta,d}^2 + \sigma_{r,d}^2 + \sigma_{z,d}^2\right]^{1/2}. \tag{5-6}$$

5.1.4 Thermal Stresses

This model is the same as in PAD 4.0 (Reference 5.1).

Thermally induced hoop stresses caused by the temperature gradient through the cladding are considered in the fatigue calculation. These stresses are given by:

[a,c] (5-7)

and

[a,c] (5-8)

where λ and η are cladding anisotropic property coefficients, k_{clad} is the clad thermal conductivity (BTU/hr-ft-°F), $q''(Z)$ is the heat flux (BTU/hr-ft^2) at axial elevation z, and $\sigma_{\theta,o}$ and $\sigma_{\theta,i}$ are at the cladding outside and inside, respectively.

Assuming isotropic properties and rearranging, simplified forms of these expressions are obtained:

[a,c] (5-9)

and

[a,c] (5-10)

where, α is the thermal expansion coefficient, μ is Poisson's ratio, ΔT is the temperature (°F) difference between clad inner and outer surface.

5.2 CLAD ELASTIC DEFORMATION

This model is the same as in PAD 4.0 (Reference 5.1).

Considering the fuel rod as a closed-end transversely isotropic thick-walled cylinder in a three dimensional system subjected to the external coolant pressure, P_s, and the internal fission gas pressure, P_f, the elastic diametric deflection at the inner surface due to the pressure differential is given by:

[a,c] (5-11)

where:

K_c = cladding radius ratio, (R_o/R_i);
μ_c = Poisson's ratio for cladding;
E_c = Young's Modulus for cladding (psi).

5.3 CLAD PLASTICITY

This model is revised for PAD5.

Cladding plastic strains follow a power law expression:

a,c

[ ] (5-12)

where:

ε_{pl} is the plastic effective strain (in/in)
σ_{eff} is the cladding effective stress (psi or MPa)
σ_y is the irradiated cladding 0.2% offset yield stress (psi or MPa)

The correlation for the plasticity model stress exponent N can be developed using the materials properties correlations for Young's modulus (E), the yield stress, and the ultimate tensile strength.

Though Equation (5-12) will be used as an equation for engineering strain as a function of engineering stress in PAD5, it is an equation for true strain as a function of true stress. This distinction is not significant for plastic strains < 2%, which is probably the maximum plastic strain that could occur in fuel rod overpower ramp tests and is certainly more than the plastic strain that would be calculated in design analyses, which will be no more than the 1% allowable transient total strain increment. However, the distinction is significant for the evaluation of unirradiated cladding tubing plasticity data when it is used to obtain data for the stress exponent N in Equation (5-12).

During a uniaxial test,

$$\varepsilon_{true} = \ln(1 + \varepsilon_{eng}) \tag{5-13}$$

and:

$$\sigma_{true} = \sigma_{eng} e^{\varepsilon_{true}} \tag{5-14}$$

Including the elastic strains, the relationship between the total true strain and the true stress is:

a,c

[ ] (5-15)

The engineering strain at the maximum is the Uniform Elongation (UE) and the engineering stress at the maximum is the Ultimate Tensile Stress (UTS). The condition defining the UE is:

[a,c] (5-16)

From Equations (5-15) and (5-16), it can be shown that the stress exponent N and the cladding Uniform Elongation (UE) are related by two coupled non-linear equations:

[a,c] (5-17)

[a,c] (5-18)

where E is the cladding Young's modulus and UTS is the cladding Ultimate Tensile Strength.

Using the Westinghouse materials properties correlations for E, the irradiated yield stress σ_y and the irradiated Ultimate Tensile Stress in Section 6, the stress exponent N for irradiated cladding is temperature dependent and is given by:

[ ]^{a,c} (5-19a)

[ ]^{a,c} (5-19b)

where:

T_c is the cladding temperature (°C).

This correlation for N is applicable to irradiated Zircaloy-4, ZIRLO, and **Optimized ZIRLO** cladding.

Figure 5.3-1 shows the behavior of the PAD5 cladding plasticity model. This plasticity model is implemented using the von Mises criterion and the Prandtl-Reuss flow law to calculate the hoop, radial, and axial components of the plastic strains as discussed in subsection 5.1.3, in the same way that the hoop, radial, and axial components of the cladding creep strains are calculated.

a,c

Figure 5.3-1 Plasticity Model Schematic Behavior

5.4 CLAD CREEP

The thermal creep model is the same as in PAD 4.0 (Reference 5.1). The irradiation creep model is revised in PAD5. The coefficients are updated for PAD5 based on calibration to in-reactor and test reactor data.

In-reactor diametral creep is predominantly a combination of the following mechanisms: thermal creep, irradiation enhanced creep, and irradiation induced diametral growth.

The in-reactor cladding creep determines the total effective strain rate by adding together the terms for thermal, irradiation, and diametral growth:

[a,c] (5-20)

where:

$\dot{\varepsilon}_{th}$ = thermal creep rate (%/hour),
$\dot{\varepsilon}_{irr}$ = irradiation creep rate (%/hour), and
$\dot{\varepsilon}_{gr}$ = diametral stress-free irradiation growth rate (%/hour).

$\dot{\varepsilon}_{th}$, $\dot{\varepsilon}_{irr}$, and $\dot{\varepsilon}_{gr}$ are treated as mid-wall quantities, i.e., mid-wall clad strain and mid-wall clad strain rate. The thermal and irradiation creep components are distributed to the hoop, radial, and axial directions based on the flow rule relationship of the deviatoric stress, effective stress, and effective strain that was established in subsection 5.1.3. Only the diametral stress free irradiation growth is considered here. The axial stress free irradiation growth is considered in Section 5.9 rod axial growth.

For each cladding type [

]^{a,c} determined with the final functional form such that the average Predicted-Measured creep value for each clad material is approximately zero; and thus the total effective strain rate is given by:

[a,c] (5-21)

Thermal effective creep rate $\dot{\varepsilon}_{th}$ is a time derivative of:

[a,c] (5-22)

where:

ε_{th} = thermal creep effective strain (-),
t = time (hour),
Φ = cumulative fast fluence (n/cm^2),
HTCAL and DTCAL are calibration coefficients.

and the secondary creep rate is:

[a,c] (5-23)

where:

$\dot{\varepsilon}_s$ = secondary creep rate (1/hour)

T = temperature (K),

σ_{eff} = effective stress (MPa),

E = Young's modulus (MPa),

STCAL and QTCAL are calibration coefficients.

and the saturated primary creep strain is:

[a,c] (5-24)

and the time constant is:

[a,c] (5-25)

where, PTCAL and CTCAL are calibration coefficients.

From a review of the available irradiation creep data on Cold-Worked Stress Relieved (CWSR) Zircaloy-4, ZIRLO, and **Optimized ZIRLO** cladding, [

]^{a,c}

a,b,c

Figure 5.4-1 B&W/EPRI CWSR Zircaloy-4 Irradiation Creep Data (103 MPa) for Various Temperatures

The revised effective irradiation creep rate $\dot{\varepsilon}_{irr}$ is:

a,c

(5-26)

where:

Φ = cumulative fast fluence (n/cm^2),
ϕ = instantaneous fast flux (n/cm^2-sec),

[ ]^{a,c} (5-27)

T = temperature (K),
AICAL, DICAL, FICAL, and TSATIRR are calibration coefficients,

[

]^{a,c}

In PAD 4.0, [

]^{a,c}. This change of temperature dependence is based on the following observations:

1. [

]^{a,c}

2. [

]^{a,c}

3. [

]^{a,c}

However, [

]^{a,c}.

The diametral growth $\dot{\varepsilon}_{gr}$ is described in Section 5.5.

The creep model calibration and model uncertainties are discussed in the creep model calibration section of Appendix A. The calibrated model coefficients are:

Table 5.4-1 PAD5 Creep Model Coefficients

Creep Model	Calibration Parameters	Values	Comments
Thermal Creep	STCAL		
	PTCAL		
	CTCAL		
	HTCAL		
	QTCAL		
	DTCAL		
Irradiation Creep	AICAL		
	DICAL		
	FICAL		
	TSATIRR		

a,c

The coefficients CCOEF1 and CCOEF2 are cladding alloy specific material constants, with values given in the following table:

Table 5.4-2 PAD5 Creep Model Alloy Specific Material Constants

Cladding Material	CCOEF1	CCOEF2
[		] a,c

5.5 CLAD DIAMETRAL GROWTH

The rod growth model for Zircaloy-4 cladding is the same as in PAD 4.0 (Reference 5.1). Rod growth models for ZIRLO cladding and ***Optimized ZIRLO*** *cladding are revised for PAD5.*

5.5.1 ZIRLO Cladding and *Optimized ZIRLO* Cladding

The fluence dependence of the experimental data for both ZIRLO and **Optimized ZIRLO** cladding is different from the PAD 4.0 model. The PAD 4.0 model has an exponential decay fluence dependence. The data exhibit an approximately linear fluence dependence. Figures 5.5-1 and 5.5-2 show that:

- The fluence dependence is linear and
- The measured strains (note that the data have negative hoop strain values) are significantly lower than the PAD 4.0 model.

The models for the stress-free diametral growth strains of ZIRLO cladding and **Optimized ZIRLO** cladding are:

[ ]^{a,c} (5-28)

where R_θ are the low fluence irradiation growth rates and Φ is the fast fluence. The values for these material parameters, for ε_θ in units of % and fast fluence in units of 10^{21} n/cm^2, are:

Parameter (Units)	ZIRLO Cladding	*Optimized ZIRLO* Cladding
R_0 (%/10^{21} n/cm^2, E>1 MeV)	[	] a,c

where [

]^{a,c}.

The hoop strain data are shown in Figures 5.5-1 for ZIRLO cladding and 5.5-2 for **Optimized ZIRLO** cladding as a function of fluence.

In the case of ZIRLO cladding, [
]^{a,c}. Figure 5.5-1 shows that the data are consistent.

In the case of **Optimized ZIRLO** cladding, [

]^{a,c}

a,b,c

[

]

Figure 5.5-1 ZIRLO Cladding Irradiation Growth Diameter Strain

a,b,c

Figure 5.5-2 *Optimized ZIRLO* Cladding Diameter Irradiation Growth

a,b,c

Figure 5.5-3 *Optimized ZIRLO* Cladding Steady State Diametral Irradiation Growth Rate

5.5.2 Zircaloy-4 Cladding

This model is the same as in PAD 4.0 (Reference 5.1).

a,c

$$\left[\qquad\qquad\right] \tag{5-29}$$

where $\dot{\varepsilon}_z$ = axial growth rate (time derivative of Equation [5-48] in subsection 5.9.3).

5.6 FUEL RELOCATION

This model is new for PAD5.

Fuel pellets crack as a result of thermal stress during operation. When there is a fuel-cladding gap, the fuel pellet fragments move towards the cladding and reduce the gap size. Previous versions of PAD have accounted for this effect in the thermal calculations, but not in the pellet-cladding mechanical interaction calculations.

When the gap is open, the relocation depends on the pellet-cladding gap size. The relocation may also change due to mutual interaction between the pellet fragments caused by thermal expansion during a power change or long term interaction effects due to fuel swelling. When the pellet-cladding gap closes, the relocation may reduce due to the contact forces exerted on the pellet fragments. This relocation reduction is not expected to be instantaneous. The magnitude of the relocation reduction depends on the contact pressure and the nature of the interface, which may change during irradiation as a result of failure or localized creep of the asperities on the fuel and/or cladding surface.

The pellet relocation phenomenon has been studied in detail by Oguma (Reference 5.2). Oguma's model is based on the analyses of pellet cracking (crack pattern and diameter increase) using out-of-pile experiments of cracked pattern behavior under soft and hard pellet-clad interaction. Oguma's work also included analyses of gap closure during power ramps of instrumented fuel rods irradiated in the Halden Boiling Water Reactor for determining the burnup and power dependence of pellet relocation. Similar models were used in developing the Westinghouse fuel performance code FATES (Reference 5.3) and the EPRI fuel performance code ESCORE (Reference 5.4).

The pellet fragment relocation diameter change is added to the hot pellet Outer Diameter (OD), calculated without considering relocation, and reduces the pellet-cladding mechanical gap. For consistency with the PAD mechanical analysis, the fragment relocation is defined as an increment in the pellet outer diameter, δD_{reloc} (in).

The initial pellet fragment diametral relocation, before the pellet-cladding gap initially closes, is given by:

$$\left[\right]^{a,c} \qquad (5\text{-}30)$$

Where:

[ ]^{a,c}

[ ]^{a,c}

[ ]^{a,c}

[ ]^{a,c}

The meaning of the variables found in these equations is as follows:

G_o = as-fabricated pellet-cladding diametral gap (in)
DP = as-fabricated pellet diameter (in)
Bu = local burnup (MWd/MTU)
Q = linear heat generation rate (kW/ft)
Q_c = critical power for pellet cracking (onset of relocation), = [ ]^{a,c}

and CRELOC0G, CRELOC0P, CRELOC1, CRELOC2, CRELOC3, and CRELOC4 are calibration constants that have been adjusted in the PAD5 calibration.

For Westinghouse fuel designs, the current calibration of the relocation model results in maximum initial diametral relocations (at high powers and low burnups) of [ ]^{a,c}, increasing to saturation at about [ ]^{a,c} at burnups of about [ ]^{a,c}, provided the gap remains open. Figure 5.6-1 shows fuel diametral relocations for a pellet diameter of 0.3444 in, and an as-fabricated diametral gap of 7 mil as a function of burnup at various power levels.

a,c

Figure 5.6-1 Behavior of the Initial Relocation as a Function of Burnup at Constant Powers

It is assumed that the relocation never decreases when the gap is open. In addition, it is assumed that when the power increases, the relocation immediately increases to the value it would have had if the fuel had been operated at the current power from Beginning of Life (BOL). Therefore, for cases where the Linear Heat Generation Rate (LHGR) changes from time step to time step before the pellet-cladding gap initially closes, the relocation is given by the maximum of Equation (5-30), calculated using the burnup and LHGR in the current time step, and the relocation at the end of the previous time step.

If the gap is closed, relocation accommodation, i.e., inward motion of the pellet fragments due to the forces applied by the cladding on the fragments, is modeled using [ ]^{a,c}:

a,c

(5-31)

where P_c is the contact pressure (psi) and η (psi-hr) is a calibration constant. The solution of this rate equation over a time interval δt is:

[ ]^{a,c} (5-32)

where $\delta D_{reloc,o}$ is the pellet relocation diameter increment at the start of the time interval. Assuming P_c varies relatively slowly over the time interval, δt:

[ ]^{a,c} (5-33)

[ ]^{a,c} gives an exponential decay time of [ ]^{a,c}, roughly consistent with the RECOR test data (Reference 5.5), for a contact pressure of [ ]^{a,c}. In the implementation, η was used as the calibration factor, CRELOC5.

When the gap re-opens, it is assumed that there will be recovery of the accommodated relocation, such that the relocation eventually returns to the maximum value given by Equation (5-30) if the gap remains open for a sufficiently long time. This recovery ($\delta D_{reloc,reopen}$) of the accommodated relocation is given by:

[ ]^{a,c} (5-34a)

[ ]^{a,c} (5-34b)

[ ]^{a,c} (5-34c)

[ ]^{a,c}

Where:

δBu is the burnup increment (MWd/MTU) in the time interval δt,
$\delta D_{reloc,o}$ is the pellet relocation diameter increment at the start of the time interval, and
$\delta D_{reloc,max}$ is the maximum value of the relocation throughout the previous operation of the fuel.

[

]^{a,c}

The pellet fragment relocation reduces the pellet-cladding gap void volume and increases the pellet internal crack void volume. The relocation's impact on void volume is discussed in Section 4.6.

Validation of the relocation model is based on fuel temperature data for open gap conditions and ramp test cladding diameter change data for both open and closed gap conditions. These calibration results are shown in Appendix A. The calibrated coefficients are:

[

]^{a,c}

5.7 FUEL SWELLING AND DENSIFICATION MODELS

This model is the same as in PAD 4.0 (Reference 5.1). Validation of the model is extended to fuel with manufacture processes that are different from those used at the Westinghouse Columbia Fuel Fabrication Facility (CFFF).

Densification and swelling are dependent on the manufacturing process. The densification and swelling model in PAD 4.0 is limited to fuel with microstructure close to Westinghouse fuel manufactured in the Columbia Fuel Fabrication Facility (CFFF). For fuel manufactured with different microstructure, the NRC densification model (Reference 5.6) is used in PAD 4.0. In PAD5, the densification model was extended to model fuel manufactured outside of the Columbia Fuel Fabrication Facility based on measured volume change data for fuel manufactured in the Westinghouse Sweden Vasteras Nuclear Fuel Factory and for the Combustion Engineering (CE) fuel manufactured in the Hematite plant.

5.7.1 Model Description

The PAD densification and swelling model is from Reference 5.7. Justification of the correlation and its coefficients are provided in Section 2-2 of Reference 5.7.

The PAD model for the fractional volume change due to solid fission product swelling and densification is:

[ ]^{a,c} (5-35)

where the first term gives the solid fission product swelling and the second term gives the densification, with F the burnup in fissions/cm^3, P_0 is the initial porosity, and N is a function of the fuel sintering temperature:

[ ]^{a,c} (5-36)

where T_{sint} is the pellet fabrication sintering temperature in K.

The PAD equation relating the burnup F in fissions/cm^3 to the burnup Bu in MWd/MTU is:

[ ]^{a,c} (5-37)

where ρ is the as-fabricated fuel fractional density (in terms of as-fabricated initial porosity P_o, $\rho = 1 - P_o$). In terms of Bu, the PAD model for solid fission product swelling and densification is:

[ ]^{a,c} (5-38)

Note that the units of Bu in Equation (5-38) are MWd/MTU.

PAD5 will use this model as the basis for fuel densification and swelling with [

]^{a,c}

5.7.2 Data and Qualification

The combined densification and swelling model is validated using volume change data. Data provided in Tables 5.7-1, 5.7-2, and 5.7-3 are for fuel manufactured in Westinghouse Columbia, Vasteras, and the former CE Hematite fuel manufacture facilities. All Westinghouse (Columbia, Vasteras, and Hematite) data are plotted in Figure 5.7-1 as function of burnup.

For fuel manufactured in the Westinghouse Columbia Fuel Fabrication Facility, the fuel densification and swelling model has been validated in Reference 5.7. [

]^{a,c} The predicted vs. measured results are shown in Figure 5.7-2, and the predicted minus measured versus burnup results are shown in Figure 5.7-3. [

]^{a,c} the model predicts the PWR fuel pellets with less uncertainty, as shown in Figure 5.7-4.

Table 5.7-1 Volume Change (ΔV/V) Data for Fuel Manufactured in Columbia Fuel Fabrication Facility

Rod	Burnup (GWd/MTU)	ΔV/V (%)	Initial Density (%)

a,b,c

Table 5.7-1 Volume Change (ΔV/V) Data for Fuel Manufactured in Columbia Fuel Fabrication Facility (cont.)

Rod	Burnup (GWd/MTU)	ΔV/V (%)	Initial Density (%)
[			]a,b,c

Note:
1. [ ]a,b,c

Table 5.7-2 Volume Change (ΔV/V) Data for Fuel Manufactured in Vasteras Nuclear Fuel Factory			
Reactor	Burnup (GWd/MTU)	ΔV/V (%)	Initial Density (%)

a,b,c

Table 5.7-2 Volume Change (ΔV/V) Data for Fuel Manufactured in Vasteras Nuclear Fuel Factory (cont.)

Reactor	Burnup (GWd/MTU)	ΔV/V (%)	Initial Density (%)

a,b,c

Table 5.7-3 Volume Change (ΔV/V) Data for CE Fuel (References 5.8 through 5.11)

Reactor	Burnup (GWd/MTU)	ΔV/V (%)	Initial Density (%)

a,b,c

Table 5.7-3 Volume Change (ΔV/V) Data for CE Fuel (References 5.8 thru 5.11) (*cont.*)

Reactor	Burnup (GWd/MTU)	ΔV/V (%)	Initial Density (%)

a,b,c

Table 5.7-3 Volume Change (ΔV/V) Data for CE Fuel (References 5.8 thru 5.11) (cont.)

Reactor	Burnup (GWd/MTU)	ΔV/V (%)	Initial Density (%)

a,b,c

a,b,c

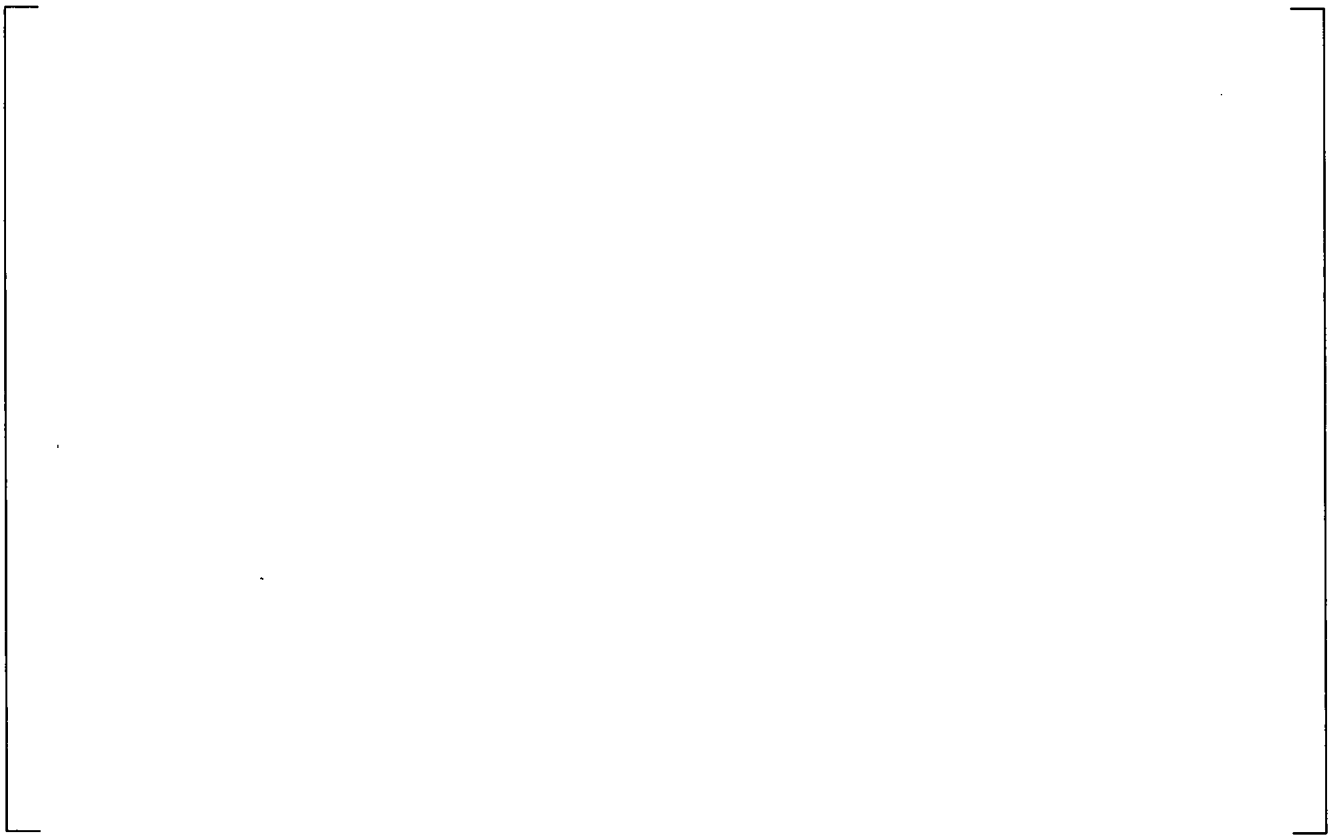

Figure 5.7-1 Columbia, Vasteras, and CE Fuel Volume Change Data Comparison

a,b,c

Figure 5.7-2 Predicted vs. Measured Volume Change (ΔV/V) Using PAD Densification and Swelling Model

a,b,c

Figure 5.7-3 Predicted – Measured Volume Change (ΔV/V) Versus Burnup for All Westinghouse Fuel Using PAD Densification and Swelling Model

a,b,c

Figure 5.7-4 Predicted – Measured Volume Change (ΔV/V) Versus Burnup for Columbia and CE Fuel Using PAD Densification and Swelling Model

5.8 FISSION GAS BUBBLE SWELLING

This model is revised for PAD5. The fission gas swelling model used in PAD 4.0 (Reference 5.1) and previous PAD versions (Reference 5.7) and developed in PAD3.3 (Reference 5.12) has been improved and recalibrated.

For irradiated fuel, fission gas atoms will diffuse through the fuel grains and accumulate at the grain boundaries. When the gas concentration reaches a certain amount, release tunnels will form and fission gas will be released to the rod internal free volume. During this process, fission gas bubbles form inside the grains as very fine bubbles and on the grain boundaries as larger bubbles. The grain boundary bubbles contribute to the majority of the gas swelling.

A schematic representation of the PAD5 fission gas swelling model is shown in Figure 5.8-1. Two significant mechanisms are modeled, depending on the temperature of the fuel. [

]^{a,c} This model is consistent with fission gas bubble/porosity data from unrestrained fuel (Section 2.9.3 of Reference 5.13) and restrained fuel (Reference 5.14).

a,c

Figure 5.8-1 Schematic of PAD5 Fission Gas Swelling Porosity Distribution

The PAD5 gas swelling is given by:

a,c

(5-39)

[

]a,c

Some irradiation time is needed for fission gas build up and bubble growth. [

]^{a,c}

For conditions allowing sufficient time for gas bubbles to develop (i.e., steady state operation or a ramp with a long hold period at high power), the burnup effect on the gas bubble swelling is modeled through BPORCM as:

a,c

(5-40)

[

]^{a,c}

For short transients, there is not enough time for the fission gas bubble to fully develop, and there will be no additional gas swelling at lower burnup and reduced gas swelling at high burnup compared to long ramps. The burnup effect on the gas bubble swelling during a short transient is modeled through BPORCM as:

a,c

(5-41)

where:

[

]^{a,c}

The fission gas swelling model is calibrated in Appendix A to the diameter change measurements from various ramp test programs at higher burnup when relocation is expected to be fully accommodated (i.e., some RISO III and Studsvik Clad Integrity Program (SCIP) ramp test rods). The calibrated BPORC, FRBUP, XBUP, FGSWFACT, BPORCTR, XBUPTR1, and XBUPTR2 are:

[

]a,c

5.9 ROD AXIAL GROWTH MODEL

Rod growth model for Zircaloy-4 is the same as in PAD 4.0 (Reference 5.1). Rod growth models for ZIRLO and ***Optimized ZIRLO*** *clad fuel are revised for PAD5.*

Separate rod growth models were developed for ZIRLO cladding, **Optimized ZIRLO** cladding, and Zircaloy-4 cladding materials.

5.9.1 ZIRLO Cladding Material

[

]a,b,c

Table 5.9-1 ZIRLO Cladding Fuel Rod Growth Data Base

Plant	Number of Measurements

a,b,c

Table 5.9-1 ZIRLO Cladding Fuel Rod Growth Data Base (cont.)

Plant	Number of Measurements
[	]a,b,c

The PAD5 ZIRLO cladding rod growth model [

]a,c

Equations (5-42) through (5-44) describe the ZIRLO cladding rod growth model developed.

[ ]a,c (5-42)

[ ]a,c (5-43)

[ ]a,c (5-44)

where:

$(\Delta L/L)_{BE}$ = Best Estimate (BE) fuel rod average growth (%)

$(\Delta L/L)_{UB}$ = Upper Bound (UB) (95% bound) fuel rod average growth (%)

$(\Delta L/L)_{LB}$ = Lower Bound (LB) (95% bound) fuel rod average growth (%)

Φ = fuel rod average fast fluence (E > 1 MeV) (10^{21} × n/cm^2)

The PAD5 ZIRLO cladding rod growth model is plotted with the ZIRLO cladding rod growth data in Figure 5.9-1. The predicted minus measured ZIRLO cladding growth as a function of fast fluence in Figure 5.9-2 confirms good agreement over the whole fast fluence range.

a,b,c

Figure 5.9-1 ZIRLO Cladding Rod Growth Data and PAD5 ZIRLO Cladding Rod Growth Model

a,b,c

Figure 5.9-2 PAD5 ZIRLO Cladding Rod Growth Model Predicted Minus Measured Residual Plot

5.9.2 *Optimized ZIRLO* Cladding Material

[

]a,b,c

Table 5.9-2 *Optimized* ZIRLO Cladding Fuel Rod Growth Data Base	
Plant	**Number of Measurements**

a,b,c

The PAD5 **Optimized ZIRLO** cladding growth model has the same form as the PAD 4.0 rod growth model, but the coefficients are adjusted to get the PAD5 **Optimized ZIRLO** cladding growth model.

Equations (5-45) through (5-47) describe the **Optimized ZIRLO** cladding growth model developed.

a,c

(5-45)

a,c

(5-46)

a,c

(5-47)

where:

$\left(\Delta L/L\right)_{BE}$ = Best Estimate (BE) fuel rod average growth (%)

$\left(\Delta L/L\right)_{UB}$ = Upper Bound (UB) (95% bound) fuel rod average growth (%)

$\left(\Delta L/L\right)_{LB}$ = Lower Bound (LB) (95% bound) fuel rod average growth (%)

Φ = fuel rod average fluence (E> 1MeV) (10^{21} × n/cm^2)

The PAD5 **Optimized ZIRLO** cladding growth model is plotted with the measured **Optimized ZIRLO** cladding growth as a function of fast fluence in Figure 5.9-3. Predicted minus measured **Optimized ZIRLO** cladding growth is plotted as a function of fast fluence in Figure 5.9-4.

a,b,c

Figure 5.9-3 ***Optimized ZIRLO*** **Cladding Rod Growth Data and PAD5 ZIRLO Cladding Rod Growth Model**

a,b,c

Figure 5.9-4 PAD5 *Optimized ZIRLO* Cladding Rod Growth Model Predicted Minus Measured Residual Plot

5.9.3 Zircaloy-4 Cladding Material

The Zircaloy-4 cladding growth model was developed in PAD 3.4 (Reference 5.7) by regression analysis of peripheral rod growth data from assemblies irradiated in the Plant AB, Plant E, and Plant AC reactors. The rod growth data base is summarized in Table 5.9-3. This data base extends to fast fluence levels of 11.8×10^{21} n/cm^2, E > 1 MeV. The rod growth model for Zircaloy-4 cladding is:

a,c

(5-48)

where:

$\frac{\Delta L}{L}$ = fractional rod length change (%)
Φ = neutron fast fluence (n/cm^2, E > 1 MeV)

Table 5.9-3 Zircaloy-4 Cladding Fuel Rod Growth Data Base						
		Creepdown Data				
Reactor	Assembly	EOC1	EOC2	EOC3	EOC4	EOC5

a,b,c

5.10 SECTION 5 REFERENCES

5.1 WCAP-15063-P-A Revision 1, with Errata, (Proprietary) and WCAP-15064-NP-A Revision 1, with Errata, (Non-Proprietary), "Westinghouse Improved Performance Analysis and Design Model (PAD 4.0)," July 2000.

5.2 M. Oguma, "Cracking and Relocation Behavior of Nuclear Fuel Pellets during Rise to Power," Nuclear Engineering and Design 76 (1983) 35-45.

5.3 CENPD-139-P-A, (Proprietary) and CENPD-139-A, (Non-Proprietary), "Fuel Evaluation Model," C-E Fuel Evaluation Model Topical Report, July 1974.

5.4 EPRI NP-5100-A, "ESCORE – the EPRI Steady-State Core Reload Evaluator Code: General Description," Final Report, April 1991.

5.5 L. Caillot, et al, "Impact of Fuel Pellet Fragmentation on Pellet-Cladding Interaction in a PWR Fuel Rods: Results of the RECOR Experimental," Transactions of the 14th International Conference on Structural Mechanics in Reactor Technology (SMiRT 14), Lyon, France, August 17-22, 1997.

5.6 Regulatory Guide 1.126, Revision 2, "An Acceptable Model and Related Statistical Methods for the Analysis of Fuel Densification," March 2010.

5.7 WCAP-10851-P-A, (Proprietary) and WCAP-11873-A, (Non-Proprietary), "Improved Fuel Performance Models for Westinghouse Fuel Rod Design and Safety Evaluations," August 1988.

5.8 DOE/ET/34010-10, CEND-414, "The Evaluation and Demonstration of Methods for Improved Fuel Utilization," October 1983.

5.9 DOE/ET/34030-11, CEND-427, "Hot Cell Examination of Extended Burnup Fuel From Fort Calhoun," September 1986.

5.10 DOE/ET/34013-15 UC-523, CEND-432, "The Evaluation and Demonstration of Methods for Improved Nuclear Fuel Utilization, Final Report," August 1994.

5.11 EPRI TR-103302-V2, CE NPSD-780-P, "Hot Cell Examination of Extended Burnup Fuel from Calvert Cliffs-1, Final Report Volume 2," May 1994.

5.12 WCAP-8720 (Proprietary), "Improved Analytical Models Used in Westinghouse Fuel Rod Design Computations," October 1976.

5.13 NUREG/CR-6150, Volume 4, Rev. 2, INEL-96/0422, "SCDAP/RELAP5/MOD3.3 Code Manual: MATPRO - A Library of Materials Properties for Light-Water-Reactor Accident Analysis," January 2001.

5.14 M. Mogensen, et al, "Local Fission Gas Release and Swelling in Water Reactor Fuel During Slow Power Transients," Journal of Nuclear Materials, 131 (1985) 162-171.

6 FUEL AND CLAD MATERIAL PROPERTIES

Section 6.1 describes the PAD5 UO_2, UO_2-Gd_2O_3, and UO_2-Er_2O_3 fuel material properties for:

- Density,
- Thermal conductivity,
- Thermal expansion,
- Specific heat,
- Melting point,
- Young's modulus, and
- Poisson's ratio.

Section 6.2 describes PAD5 treatment of ZrB_2 coating on UO_2 fuel.

Section 6.3 provides descriptions of the Zircaloy, ZIRLO and **Optimized ZIRLO** cladding models for:

- Density,
- Thermal conductivity,
- Thermal expansion,
- Specific heat and enthalpy,
- Young's modulus,
- Poisson's ratio,
- Yield strength,
- Ultimate tensile strength,
- Irradiation hardening

The fill gas and fission gas thermal conductivity expressions are provided in Section 6.4.

Lastly, the applicability of the material property models to rod average burnup up to [ ]^{a,c} is supported in Section 6.5.

6.1 FUEL: UO_2/UO_2-GD_2O_3/UO_2-ER_2O_3

6.1.1 Density

The density for UO_2 and UO_2-Gd_2O_3 is the same as what is in PAD 4.0. The density for UO_2-Er_2O_3 is new for PAD5, but the same as what was used in FATES3B.

ρ_o theoretical density (T. D., g/cm^3)

UO_2 (Reference 6.1)

$$\rho_o = 10.96 \text{ g/cm}^3 \quad (6\text{-}1)$$

UO_2-Gd_2O_3

[ ]^{a,c} (6-2)

[ ]^{a,c}

UO_2-Er_2O_3 (Reference 6.3)

[ ]^{a,c} (6-3)

[ ]^{a,c}

6.1.2 Thermal Conductivity

The model for UO_2 and UO_2-Gd_2O_3 are updated for PAD5. The model for UO_2-Er_2O_3 is new for PAD5.

UO_2

The fuel thermal conductivity model used in PAD 4.0 (Reference 6.1) was updated to incorporate thermal conductivity degradation with burnup. The burnup dependent term, f(BU), is modeled after the [ ]^{a,c}, to account for thermal conductivity degradation as a function of burnup. The model coefficients were updated based on calibration to measured fuel centerline temperatures. The updated model is:

[ ]^{a,c} (6-4)

where:

[ ]^{a,c} (6-5)

K_{95} = thermal conductivity for fuel with 95% theoretical density (W/cm-°C)
Bu = local burnup (GWd/MTU)
TC = fuel temperature (°C)

For thermal conductivity for fuel with any other density,

$$K_{density} = \frac{1-P}{1+\beta P} K_{100} = \left(\frac{1-P}{1+\beta P}\right) \times 1.08 \times K_{95} \quad (6\text{-}6)$$

where:

P = Fractional porosity of the fuel ring (1-density)
β = a coefficient which is equal to 0.5 for P≤ 0.05 and which is equal to 1.0 for P> 0.05
K_{100} = thermal conductivity for fuel with 100% theoretical density

Additional details on the calibration of PAD5 to measured fuel centerline temperature data are presented in Appendix A.

UO_2-Gd_2O_3 and UO_2-Er_2O_3

The thermal conductivity model for fresh urania-gadolinia/erbia used in PAD5 is developed from the same data and using the same methodology as was the CE urania- gadolinia/erbia thermal conductivity model licensed for use in the FATES3B code (Reference 6.3).

The PAD5 model is based on measured thermal conductivity data of urania/erbia and verified for gadolinia using the same measured gadolinia thermal conductivity data used to bench mark the FATES3B urania-erbia/gadolinia thermal conductivity model.

Figure 6.1-1 compares the predicted values versus the measured data for the urania-erbia/gadolinia model. Excellent agreement was obtained between the measured and predicted values. Figure 6.1-2 and 6.1-3 are plots of the residuals (measured minus predicted value) versus erbia/gadolinia content and temperature.

a,b,c

Figure 6.1-1 Predicted vs. Measured Data for the PAD5 Urania-erbia/Gadolinia Thermal Conductivity Model

a,b,c

Figure 6.1-2 Residuals (Measured Minus Predicted Values) Versus Erbia/Gadolinia Content

a,b,c

Figure 6.1-3 Residuals (Measured Minus Predicted Values) Versus Temperature

The burnup dependent term for the urania-erbia/gadolinia model is the same as for the urania model in Equation (6-5). The final derived urania-erbia/gadolinia thermal conductivity model for PAD5 is: a,c

[ ] (6-7)

[

]a,c

6.1.3 Thermal Expansion

This model is the same as what is in PAD 4.0

UO_2 (Reference 6.1)

$$\Delta L/L_o = 6.797 \times 10^{-6}T + 2.896 \times 10^{-9}T^2 - 1.723 \times 10^{-4} \text{ (in/in)} \quad (6\text{-}8)$$

where T is temperature, in °C, for 25°C < T < melting temperature.

UO_2-Gd_2O_3

Thermal expansion of UO_2 with low Gd_2O_3 concentrations is approximated by that of pure UO_2 (Reference 6.2), which is:

$$\Delta L/L_o = 6.797 \times 10^{-6}T + 2.896 \times 10^{-9}T^2 - 1.723 \times 10^{-4} \text{ (in/in)} \quad (6\text{-}9)$$

for 25°C ≤ T ≤ melting temperature, and [ ]a,c

UO_2-Er_2O_3 (Reference 6.3)

Considering the similarity between erbia and gadolinia, the thermal expansion of a urania-erbia mixture is concluded to be the same as that of urania gadolinia mixtures and, therefore, identical to the thermal expansion of pure urania (Reference 6.1):

$$\Delta L/L_o = 6.797 \times 10^{-6}T + 2.896 \times 10^{-9}T^2 - 1.723 \times 10^{-4} \text{ (in/in)} \quad (6\text{-}10)$$

for 25°C < T < melting temperature, and [ ]a,c

6.1.4 Specific Heat

This model is the same as what is used with PAD 4.0.

UO_2 (Reference 6.1)

The relationship derived by Kerrisk and Clifton (Reference 6.6) is used for calculating the specific heat for UO_2.

$$Cp(UO_2) = \frac{5.486\times10^6 \exp\left(\frac{535.3}{T}\right)}{T^2\times\left(\exp\left(\frac{535.3}{T}\right)-1\right)^2} + 1.569\times10^{-3}\times T + \frac{1.0707\times10^{11}}{T^2}\exp\left(\frac{-1.897\times10^4}{T}\right) \text{ (cal/mole·K)} \quad (6\text{-}11)$$

T= temperature, K, for 298 K< T < melting temperature

UO_2-Gd_2O_3

Specific heat determinations for urania with small additions of gadolinia indicate a small increase over the specific heat of urania. These [ ]^{a,c}. The relationship for the specific heat of UO_2-Gd_2O_3 solid solutions is given below (Reference 6.2):

[ ]^{a,c} (6-12)

where:

C_p (UO_2-Gd_2O_3) = Specific heat of UO_2-Gd_2O_3 mixture, cal/mole· K
W_g = Weight percent of Gd_2O_3, [ ]^{a,c}
C_p(UO_2) = Specific heat of UO_2, cal/mole· K, and is given in Equation (6-11):

UO_2-Er_2O_3

The specific heat of dilute mixtures of urania-erbia is expected to behave similarly to the urania-gadolinia data (Reference 6.3). Hence, a [ ]^{a,c} is applicable for calculating the specific heat of urania-erbia mixtures.

[ ]^{a,c} (6-13)

where:

C_p (UO_2-Er_2O_3) = Specific heat of UO_2-Er_2O_3 mixture, cal/mole· K
W_E = Weight percent of Er_2O_3, [ ]^{a,c}
C_p(UO_2) = Specific heat of UO_2, cal/mole· K, and is given in Equation (6-11)

6.1.5 Melting Point

The melting point for fresh UO_2 is the same as what is used with PAD 4.0. [

]^{a,c}

UO_2 (Reference 6.1)

The improved melting temperature model with an updated burnup dependence term (References 6.7 and 6.8) is used in PAD5:

[ ]^{a,c} (6-14)

where:

T_m = Melting temperature in °C
Bu = Burnup in GWd/MTU.

UO_2-Gd_2O_3

The published experimental data indicate small Gd_2O_3 additions to UO_2 only slightly depress the melting temperatures. The following conservative correlation is used for the melting point of a UO_2-Gd_2O_3 solid solution (Reference 6.2):

[ ]^{a,c} (6-15)

where:

Wg = wt. % Gd_2O_3, for [ ]^{a,c}
T_m = temperature in °C
Bu = fuel burnup in GWd/MTU.

UO_2-Er_2O_3

The expression for melt temperature as a function of erbia content (Reference 6.2 and 6.3) and burnup (References 6.7 and 6.8) is:

[ ]^{a,c} (6-16)

where:

$T_{melt, erbia}$ is the melting point of urania-erbia, °C
W_E = wt% erbia, [ ]^{a,c}
Bu = burnup in GWd/MTU.

6.1.6 Young's Modulus

This model is the same as what is in PAD 4.0.

The model for the Young's modulus of UO_2 (Reference 6.1) is given as follows:

$$E = (32.548 \times 10^6 - 1.859 \times 10^3 TF_o)(1 - 2.277P_o) \text{ (psi)} \quad (6\text{-}17)$$

where:

P_o is the volume fraction of porosity;
TF_o is the temperature in °F

The Young's modulus for UO_2-Gd_2O_3 and UO_2-Er_2O_3 fuel is the same as for UO_2 fuel. The Young's modulus depends on the inter-atomic forces between neighboring atoms of the major ceramic component.

6.1.7 Poisson's Ratio

This model is the same as what is in PAD 4.0.

The recommended model for the Poisson's Ratio of UO_2 (Reference 6.1) is given as follows:

$$\mu = (0.361 - 1.439P_o) / (1 - 1.660P_o) \quad (6\text{-}18)$$

where:

P_o is the porosity fraction

Poisson's ratio for UO_2-Gd_2O_3 and UO_2-Er_2O_3 fuel is the same as for UO_2 fuel. The Poisson's ratio depends on the inter-atomic forces between neighboring atoms of the major ceramic component.

6.2 ZIRCONIUM DIBORIDE INTEGRAL FUEL BURNABLE ABSORBER (IFBA)

Zirconium diboride (ZrB_2) Integral Fuel Burnable Absorber (IFBA) can be used in all of the Westinghouse fuel rod designs. The ZrB_2 is applied as a thin coating layer onto the outer surface of the uranium dioxide (UO_2) fuel pellet stack prior to loading into the fuel rod cladding tubes rather than being mixed with the UO_2 as is done with other absorber materials (e.g., erbia or gadolinia). As the B^{10} isotope in the ZrB_2 IFBA absorber burns out, the fuel rod is left with no residual absorber, unlike other absorber materials like erbium or gadolinium. The burnout of the B^{10} absorber results in production of helium gas which is released into the fuel rod plenum, increasing internal gas pressure. [ ]^{a,c}. The helium production effect on internal gas pressure and gas conductivity is taken into account in the design and safety evaluations for Westinghouse fueled PWRs. Neutronics codes already contain the capability to predict neutronics related behavior of the ZrB_2 IFBA absorber. In the PAD code only a ZrB_2 IFBA helium generation and release model is required. Although PAD predicted fuel rod internal conditions (pressures, temperatures, etc.) are ZrB_2 IFBA

specific for input to other analyses, no coding modifications are required for other design and safety analysis codes.

The ZrB_2 coating currently used in all Westinghouse ZrB_2 IFBA designs contains boron that has been enriched in the B^{10} isotope. [

]^{a,c} The ZrB_2 IFBA coating is applied over the center of the UO_2 pellet stack length and does not extend to either end of the fuel rod. The ends without ZrB_2 IFBA are referred to as cutback regions. The fuel pellets in the cutback regions may be solid, annular, or a combination of solid and annular geometry (i.e., solid pellet at the bottom of the pellet stack with annular pellets at the top of the pellet stack) and may be at reduced U^{235} enrichment (blankets). However, the ZrB_2 IFBA coating is applied only to the central solid fuel pellet stack. ZrB_2 IFBA fuel rods are loaded into an assembly in specific fuel rod locations as a matrix of ZrB_2 IFBA and UO_2 fuel rods.

The thickness of the ZrB_2 IBFA coating [

]^{a,c}

The stability of the B^{10} depleted ZrB_2 layer has been confirmed through hotcell examinations of commercial rods ranging in burnup from [ ]^{a,c}. No increase in pellet roughness is observed in irradiated ZrB_2 coated fuel compared to UO_2 fuel of similar burnups.

6.3 CLADDING: ZIRCALOY/ZIRLO/*OPTIMIZED ZIRLO*

6.3.1 Density

This model is the same as what is in PAD 4.0.

The density (References 6.11 and 6.12) for Zircaloy, ZIRLO or **Optimized ZIRLO** alloy at 25°C is:

$$\rho_o = 6.56 \pm 0.02 \text{ g/cm}^3 \quad (6\text{-}19)$$

6.3.2 Thermal Conductivity

This model is the same as what is in PAD 4.0.

Zircaloy-4 (Reference 6.13)

[ ]^{a,c} (6-20)

where:

k = thermal conductivity in (W/cm-°C)
T = temperature in °C, [ ]^{a,c}

ZIRLO Cladding/*Optimized ZIRLO* cladding (References 6.11, 6.12 and 6.13)

[ ]^{a,c} (6-21)

where:

k = thermal conductivity in (W/cm-°C)
T = temperature in °C, [ ]^{a,c}

CRUD (Reference 6.14)

The following are typical values used in PAD5.

K_f=0.5 (BTU/hr-ft-°F) for forced convection without boiling (Reference 6.15) (6-22)

K_b=4.0 (BTU/hr-ft-°F) for nucleate boiling through a crudded surface (Reference 6.16) (6-23)

K_b=0 (BTU/hr-ft-°F) for nucleate boiling from an essentially clean surface (Reference 6.17) (6-24)

ZrO_2

For thermal calculations (Reference 6.13 and 6.18):

[ ]^{a,c} (6-25)

6.3.3 Thermal Expansion

This model is the same as what is in PAD 4.0.

The thermal expansion models for Zircaloy-4, ZIRLO cladding and **Optimized ZIRLO** cladding are (References 6.1, 6.9, 6.11 and 6.12):

$$\Delta L/L\,(axial) = (2.92\times10^{-6})\times(T-70) \quad (6\text{-}26)$$

$$\frac{\Delta R}{R_0}(radial) = (3.22\times10^{-6})(T-70) \quad (6\text{-}27)$$

where:

T is temperature in °F, 70°F < T < 800°F

6.3.4 Specific Heat and Enthalpy

This model is the same as what is used with PAD 4.0.

For approximate calculations, the following values are used up to the temperature where the alpha-to-beta phase change starts to occur. The specific heat of ZIRLO cladding is different from that of Zircaloy-4 primarily because of the difference in the temperature range over which the alpha-to-beta phase change occurs for the two alloys.

For Zircaloy-4 (References 6.1 and 6.18):

Enthalpy

H_0^t = -0.379 + 0.0738T (cal/g), T in °C (0°–492°C), (32°–918°F) (6-28)

H_0^t = -6.607 + 0.08648T (cal/g), T in °C (492°–823°C), (918°–1513°F) (6-29)

Specific Heat

C_p = 0.0738 (cal/(g*K)) (0°–492°C), (32°–918°F) (6-30)

C_p = 0.08648 (cal/(g*K)) (492°–823°C), (918°–1513°F) (6-31)

For ZIRLO cladding and **Optimized ZIRLO** cladding (References 6.11 and 6.12):

Enthalpy

H_0^t = -0.379 + 0.073T (cal/g), T in °C (0°–516°C), (32°–961°F) (6-32)

H_0^t = -6.607 + 0.0878T (cal/g), T in °C (516°–751°C), (961°–1384°F) (6-33)

Specific Heat

C_p = 0.073 (cal/(g*K)) (0°–516°C), (32°–961°F) (6-34)

C_p = 0.0878 (cal/(g*K)) (516°–751°C), (961°–1384°F) (6-35)

6.3.5 Young's Modulus

This model is the same as what is in PAD 4.0.

For temperatures from 0° to 1200°F, the Young's modulus for Zircaloy-4, ZIRLO cladding and **Optimized ZIRLO** cladding is (References 6.1, 6.9, 6.12 and 6.20):

Circumferential elastic modulus:

[ ]^{a,c} (6-36)

Longitudinal elastic modulus:

[ ]^{a,c} (6-37)

6.3.6 Poisson's Ratio

This model is the same as what is in PAD 4.0.

For temperatures from 0° to 1200°F, the Poisson's ratio for Zircaloy-4, ZIRLO cladding and **Optimized ZIRLO** cladding is (References 6.1, 6.9, 6.12 and 6.20):

for the Poisson's ratio (circumferential strain /imposed longitudinal strain):

[ ]^{a,c} (6-38)

for the Poisson's ratio (radial strain/imposed longitudinal strain):

[ ]^{a,c} (6-39)

6.3.7 Yield Strength

This model is the same as what is in PAD 4.0.

a. Cold Worked Stress Relieved Anneal (SRA) Zircaloy-4

1. Best estimate unirradiated (Reference 6.1)

$\sigma_y = 92300 - 52.571$ TF (psi) for TF $\leq$ 700°F (6-40)

$\sigma y = 137750 - 117.500$ TF (psi) for 700 <TF$\leq$ 900°F (6-41)

2. Best estimate irradiated (Reference 6.1)

[ ]^{a,c} (6-42)

[ ]^{a,c} (6-43)

[ ]^{a,c}

b. Cold Worked Stress Relieved Anneal (SRA) ZIRLO Cladding

1. Best estimate unirradiated (Reference 6.9)

[ ]^{a,c} (6-44)

[ ]^{a,c} (6-45)

2. Best estimate irradiated

[ ]^{a,c} (6-46)

[ ]^{a,c} (6-47)

[ ]^{a,c}

c. Partially Recrystallized *Optimized ZIRLO* Cladding

1. Best estimate unirradiated

[ ]^{a,c} (6-48)

2. Best estimate irradiated

[ ]^{a,c} (6-49)

[ ]^{a,c} (6-50)

[ ]^{a,c}

6.3.8 Ultimate Tensile Strength

This model is the same as what is used with PAD 4.0.

a. Cold Worked Stress Relieved Anneal (SRA) Zircaloy-4

1. Best estimate unirradiated

[ ]^{a,c} (6-51)

[ ]^{a,c} (6-52)

2. Best estimate irradiated

[ ]^{a,c} (6-53)

[ ]^{a,c} (6-54)

[ ]^{a,c}

b. Cold Worked Stress Relieved Anneal (SRA) ZIRLO Cladding

1. Best estimate unirradiated

[ ]^{a,c} (6-55)

[ ]^{a,c} (6-56)

2. Best estimate irradiated

[ ]^{a,c} (6-57)

[ ]^{a,c} (6-58)

[ ]^{a,c}

c. Partially Recrystallized *Optimized ZIRLO* Cladding

1. Best estimate unirradiated

[ ]^{a,c} (6-59)

2. Best estimate irradiated

[ ]^{a,c} (6-60)

[ ]^{a,c} (6-61)

[ ]^{a,c}

6.3.9 Irradiation Hardening

This model is new for PAD5.

An irradiation hardening model in the form of, [ ]^{a,c}, has been developed based on published data (References 6.22, 6.23, and 6.24) to take into account the phenomenon of irradiation hardening that occurs at the beginning of life. The database contains literature data at different test temperatures and starting material conditions. To simplify data analysis, the data were normalized by [ ]^{a,c}. An exponential form, [ ]^{a,c}, was selected to approximate the irradiation hardening phenomena. This exponential form is fitted to the normalized data and a coefficient of [ ]^{a,c} is obtained. The normalized data along with the curve fit are plotted in Figure 6.3-1. The model can be applied as a multiplier to the fully irradiation hardened mechanical strength model in the following manner:

[ ]^{a,c} (6-62)

where:

σ_o is the unirradiated cladding yield strength or ultimate tensile strength (psi or MPa)
σ_f is the fully hardened irradiated cladding yield strength or ultimate tensile strength (psi or MPa)
Φ is the fast neutron fluence (n/cm^2, E > 1 MeV)

The model above is applicable to zirconium based alloys with a maximum of 3 percent alloying elements. The same functional form will be used for ZIRLO and **Optimized ZIRLO** cladding.

a,b,c

Figure 6.3-1 Zircaloy Irradiation Hardening Data Plotted with Proposed Irradiation Hardening Model

6.4 FILL GAS & FISSION GAS MATERIAL PROPERTIES

This model is the same as what is in PAD 4.0.

The thermal conductivity equations of fission gases xenon and krypton (Reference 6.14) were fit to the correlated data of Gandhi and Saxena (Reference 6.21):

$$K_{Xe} = 1.395 \times 10^{-5} T^{0.872} \quad \text{BTU /hr-ft-°F} \qquad (6\text{-}63)$$

$$K_{Kr} = 1.588 \times 10^{-5} T^{0.92331} \quad \text{BTU /hr-ft-°F} \qquad (6\text{-}64)$$

where T is in degrees Rankine. It is assumed that [

]^{a,c}.

The thermal conductivity equations for air, nitrogen, and hydrogen used in the PAD5 code are:

$$K_{air} = 7.35 \times 10^{-5} T^{0.846} \quad \text{BTU /hr-ft-°F} \qquad (6\text{-}65)$$

$$K_{N2} = 7.35 \times 10^{-5} T^{0.846} \quad \text{BTU /hr-ft-°F} \qquad (6\text{-}66)$$

$$K_{H2} = 5.834 \times 10^{-4} T^{0.8213} \quad \text{BTU /hr-ft-°F} \qquad (6\text{-}67)$$

where:

T is in degrees Rankine.

For fill gas argon, the thermal conductivity is given by:

[ ]^{a,c} (6-68)

[ ]^{a,c} (6-69)

The thermal conductivity of fill and fission gas helium is based on the results presented by Tsederberg (Reference 6.4). The equation, which is a function of pressure and temperature, is:

[ ]^{a,c} (6-70)

where:

T = gas temperature, in degrees Rankine, and
P = gas pressure, in psia.

For the thermal conductivity of water vapor, the steam tables are used.

6.5 APPLICABILITY OF MATERIAL MODELS TO HIGH BURNUP

The models in PAD5 are applicable to a burnup of [ ]^{a,c} and the material performance supports burnups of [ ]^{a,c} for **Optimized ZIRLO** clad fuel rods. The materials properties for **Optimized ZIRLO** cladding are applicable to burnups of [ ]^{a,c} based on evaluation of post irradiation exam data. The evaluation of poolside and hotcell data collected to a maximum fuel rod burnup of [ ]^{a,c} indicates that there is a consistent behavior for the fuel rods in general, but especially with respect to cladding corrosion, cladding yield, ultimate tensile strength (UTS) and cladding ductility.

In Figure 6.5-1, corrosion data for ZIRLO and **Optimized ZIRLO** cladding are plotted as a function of rod average burnup (Reference 6.10). Figure 6.5-2 plots irradiated clad yield strength for ZIRLO and **Optimized ZIRLO** cladding as a function of fast neutron fluence. Figure 6.5-3 plots irradiated clad UTS for ZIRLO and **Optimized ZIRLO** cladding as a function of fast neutron fluence. In the latter two cases there is no distinct trend with increasing burnup (fluence).

Since the maximum waterside oxide thickness associated with the cladding corrosion increases with burnup, the maximum cladding hydrogen content will also increase with burnup. There is some decrease in ductility with increasing hydrogen, but the dominant impact on the cladding irradiated ductility is due to irradiation damage. This can be observed in Figure 6.5-4 where cladding uniform plastic strain is plotted as a function of cladding metal hydrogen content. Only a slight decrease in uniform strain is observed as hydrogen increases.

The evaluation of the data indicates that the **Optimized ZIRLO** cladding will maintain sufficient mechanical capability to insure that no unanticipated failure modes will occur at burnups of [ ]^{a,c}.

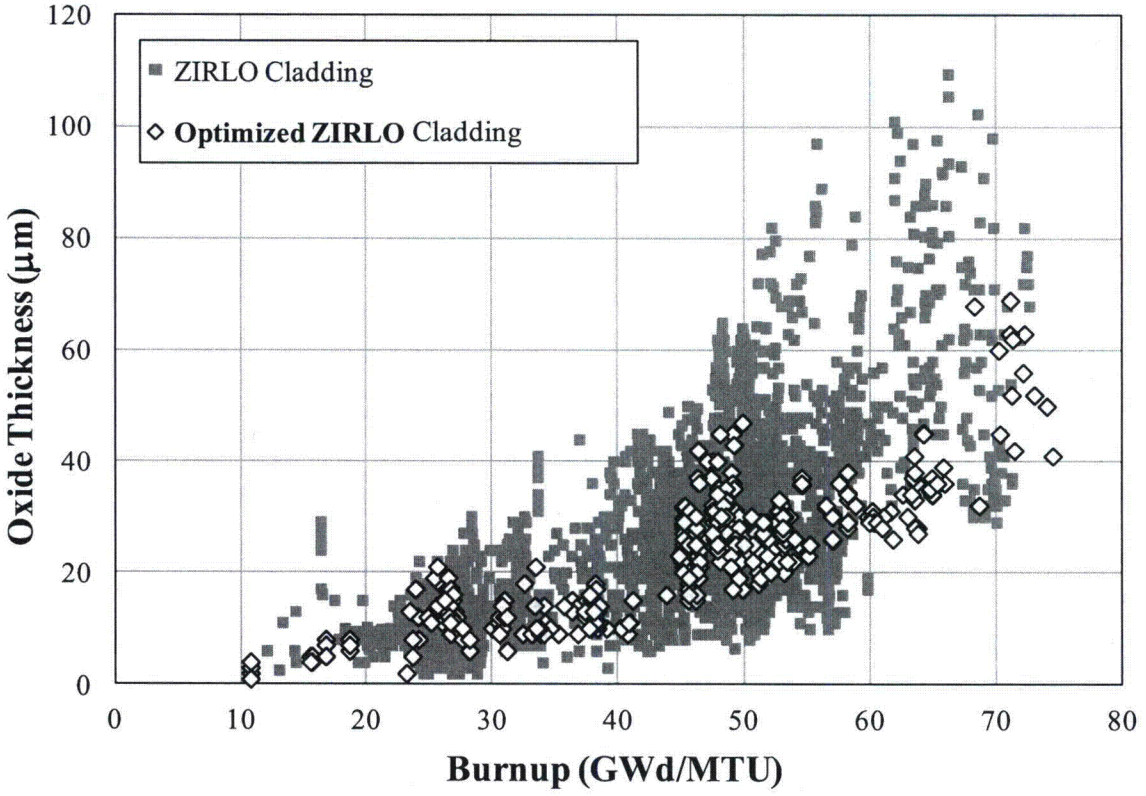

Figure 6.5-1 ZIRLO and *Optimized ZIRLO* Cladding Corrosion Waterside Oxide Thickness as a Function of Burnup

a,b,c

Figure 6.5-2 ZIRLO and *Optimized ZIRLO* Cladding High Temperature Yield Stress as a Function of Rod Average Fast Fluence

a,b,c

Figure 6.5-3 ZIRLO and *Optimized ZIRLO* Cladding High Temperature Ultimate Tensile Strength as a Function of Rod Average Fast Fluence

a,b,c

Figure 6.5-4 ZIRLO and *Optimized ZIRLO* Cladding Uniform Plastic Strain as a Function of Hydrogen Content of the Cladding Metal

6.6 SECTION 6 REFERENCES

6.1 WCAP-9179 (Proprietary), Revision 1, and WCAP-9224 (Non proprietary) "Properties of Fuel and Core component Materials,", July 1978.

6.2 CENPD-275-P, Revision 1-P, Supplement 1-P-A (Proprietary) and CENPD-275-NP, Revision 1-NP, Supplement 1-NP-A (Non-Proprietary), "C-E Methodology for PWR Core Designs Containing Gadolinia-Urania Burnable Absorbers," April 1999.

6.3 CENPD-382-P-A (Proprietary) and CENPD-382-NP-A (Non-Proprietary), "Methodology for Core Designs Containing Erbium Burnable Absorbers," August 1993.

6.4 N. V. Tsederberg, "Thermal conductivity of Gases and Liquids," the M.I T. Press., Cambridge, Mass., 1965.

6.5 HWR-469, "Assessment of UO2 Conductivity Degradation based on in-pile temperature data," OECD Halden Reactor Project, April 1996.

6.6 J. F. Kerrisk and D. G. Clifton, "Smoothed Values of the Enthalpy and Heat Capacity of UO_2," Nucl. Technol. 16, 531-535 (1972).

6.7 S.G. Popov, J.J. Carbajo, V.K. Ivanov, and G.L. Yoder, "Thermalphysical Properties of MOX and UO2 Fuels Including the Effects of Irradiation," ORNL/TM-2000/351, (2000).

6.8 J.J. Carbajo, G.L. Yoder, S.G. Popov, V.K. Ivanov, "A review of the thermalphysical properties of MOX and UO2 Fuels," Journal of Nuclear Materials, 299, 181, (2001).

6.9 CENPD-404-P-A (Proprietary) and CENPD-404-NP-A (Non-Proprietary), Revision 0, "Implementation of ZIRLO™ Cladding Material in CE Nuclear Power Fuel Assembly Designs," November 2001.

6.10 G. Pan, A. M. Garde, and A. R. Atwood, "High Burnup **Optimized ZIRLO™** Cladding Performance," 2013 LWR Fuel Performance/ TopFuel, Charlotte, North Carolina, USA, September 15-19, 2013.

6.11 WCAP-12610-P-A (Proprietary), and WCAP-14342-A (Non-Proprietary), "VANTAGE+ Fuel Assembly Reference Core Report," April 1995.

6.12 WCAP-12610-P-A & CENPD-404-P-A, Addendum 1-A (Proprietary) and WCAP-14342-A & CENPD-404-NP-A, Addendum 1-A, (Non-Proprietary), "**Optimized ZIRLO™**," July 2006.

6.13 WCAP-15063-P-A Revision 1, with Errata, (Proprietary) and WCAP-15064-NP-A Revision 1, with Errata, (Non-Proprietary), "Westinghouse Improved Performance Analysis and Design Model (PAD 4.0)," July 2000.

6.14 NS-SL-521, NS-SL-524, and NS-SL-543, (Proprietary), and NS-SL-527, and NS-SL-544, (Non Proprietary), Supplemental information on fuel design transmitted from R. Salvatori, Westinghouse, to D. Knuth, AEC, January 1973.

6.15 F. W. Dittus, and 1. M. K. Boelter, University of California Publications in Engineering, 2, 443, 1930.

6.16 L. S. Tong, "Heat-Transfer Mechanism in Nucleate and Film Boiling," Nuc. Engs. & Des., 21 (1972),1-25.

6.17 J. R. S. Thom, W. M. Walker, T. A. Fallon, and G. F. S. Reising, "Boiling in Sub-cooled Water During Flow Up Heated Tubes or Annuli," Proceedings of the Institution of Mechanical Engineers, Pt, vol. 180, 3C, 1966, p.226-246.

6.18 WCAP-12610-P-A & CENPD-404-P-A, Addendum 2, "Westinghouse Clad Corrosion Model for ZIRLO™ and **Optimized ZIRLO™**," November 2008.

6.19 C. R. Brooks and E. E. Stansbury, "The Specific Heat of Zircaloy-2 from 50°C to 700°C," J. Nucl. Mater., pp. 233-34 (1966).

6.20 D. B. Scott, "Physical and Mechanical Properties of Zircaloy-2 and -4," WCAP-3269-41, May 1965.

6.21 J. M. Gandhi and S. C. Saxena, "Correlated Thermal Conductivity Data of Rare Gases and their Binary Mixtures at Ordinary Pressures," Journal of Chemical and Eng. Data, Vol. 13, No. 3, July 1968.

6.22 A.L. Bement, Jr. "Radiation Damage in Hexagonal Close-Packed metals and Alloys," in Symposium on Radiation Effects, Asheville, NC, Sept. 1965, AIME Vol 37, American Institute of Mining Metallurgical, and petroleum Engineers, Gordon and Breach, p 671, 1967.

6.23 K. Pettersson, G. Vesterlund, and T. Andersson, "Effect of Irradiation on the Strength, Ductility, and Defect Sensitivity of Fully Recrystallized Zircaloy Tube," Zirconium in the Nuclear Industry (Fourth Conference), ASTM STP 681, ASTM, P155, 1979.

6.24 P. Moriz, J. Baicry, and J.P. Mardon, "Effect of Irradiation at 588K on Mechanical Properties and Deformation behavior of Zirconium Alloy Strip", Proceedings of 7th Zirconium in the Nuclear Industry International Symposium, ASTM STP 939, pp101119, June 1985.

7 FUEL ROD DESIGN CRITERIA AND EVALUATION METHODOLOGY

7.1 INTRODUCTION

This section describes the design bases and functional requirements used in the Westinghouse fuel rod design. The design bases support the fundamental criteria that must be met using approved analytical tools and methods. With the implementation of PAD5, the fuel rod design processes for both Westinghouse Nuclear Steam Supply System (NSSS) and Combustion Engineering (CE) NSSS applications are integrated, so that the fuel rod design bases and criteria presented in this section apply to all Westinghouse United States (US) Pressurized Water Reactor (PWR) fuel rod analyses. These design criteria and associated application methods supersede prior approved design criteria applied to Westinghouse and CE NSSS plant analyses when PAD5 is applied.

PAD5 is the primary Westinghouse fuel rod design tool. It incorporates all relevant fuel performance phenomena, including fuel thermal conductivity degradation with burnup and enhanced fission gas bubble swelling at high burnup, as an integrated set of interrelated performance models. Using appropriate input describing fuel rod operating conditions, PAD5 calculates key fuel performance parameters such as cladding stress, strain, oxidation and hydriding, fuel temperature and volume changes, and rod internal pressure. Section 7.2 provides additional discussion of the typical fuel rod design interfaces and the types of input that are required for fuel rod design analyses.

The primary objectives of the fuel design and safety analyses are to provide assurance that:

1. The fuel system is not damaged as a result of normal operation and anticipated operational occurrences;

2. Fuel system damage is never so severe as to preclude control rod insertion when required;

3. The number of fuel rod failures is not underestimated for postulated accidents; and

4. Coolability is always maintained.

General Design Criteria (GDC) 10, in Appendix A to 10 CFR Part 50, states that "The reactor core and associated coolant, control, and protection systems shall be designed with appropriate margin to assure that specified acceptable fuel design limits are not exceeded during any condition of normal operation, including the effects of anticipated operational occurrences." Section 7.3 provides an overview of fuel rod design analysis methods for addressing the acceptance limits, including a discussion of how limiting rods are defined, how fuel rod power histories are developed to model the limiting rods, and how uncertainties in fabrication parameters, fuel performance models and operating system parameters are addressed in design. The fuel rod design criteria presented in Section 7.4 establish the Westinghouse acceptance limits that must be satisfied for Condition I and Condition II operation by the fuel rod design to address the requirements of Section 4.2 of the Standard Review Plan (SRP), Reference 7.1.

Standard classifications of reactor operating conditions have been defined in both the SRP Section 15 (Reference 7.2) and in published American National Standards Institute (ANSI) standards (References 7.3 and 7.4), as summarized in Table 7.1-1. This table also indicates the relationship between the two classification sets as established in the SRP Section 15. As noted in SRP Section 15, either classification set may be used. Westinghouse fuel system designs have typically employed the ANS 51.1/ANSI 18.2 classification which uses 4 classifications: Condition I for normal operation and Conditions II, III and IV for transient events of varying probability or frequency of occurrence. The breakdown of events by frequency of occurrence as defined in the ANS 51.1/ANSI 18.2 standard is consistent with the event frequency classifications in Chapter 15 of US NRC Regulatory Guide 1.70 (Reference 7.5).

The Westinghouse fuel rod design process assures good fuel performance during Condition I (normal operation) and Condition II (events of moderate frequency) operation by confirming that all of the design criteria in Section 7.4 are satisfied. Condition III (infrequent events) and Condition IV (limiting faults) events, which allow for some fuel rod failure provided that radiological dose limits are satisfied, are addressed by Westinghouse safety analysis groups. PAD5 may be used to provide input to these safety analyses, however, as described in Section 7.5.

Examples of plant operating conditions or events considered as Condition I, Condition II, Condition III or Condition IV operation are provided in Tables 7.1-2, 7.1-3, 7.1-4 and 7.1-5, respectively. Under the SRP classifications, Condition I is equivalent to Normal Operation (NO), Condition II events are Anticipated Operational Occurrences (AOOs), Condition III events are either AOOs or Postulated Accidents, and Condition IV events are Postulated Accidents (PA).

Table 7.1-1 SRP Section 15 and ANSI18.2 /ANS 51.1 Operating Condition Classifications

SRP Section 15 Operating Conditions	ANSI 18.2/ANS 51.1 Operating Conditions
Normal Operation (NO) – Frequent and/or expected modes of operation that occur in the normal course of plant operation.	Condition I Operation – Normal operation and operational transients.
Anticipated Operational Occurrences (AOO) – Conditions expected to occur one or more times during the life of a nuclear power plant.	Condition II Operation – Events of moderate frequency, i.e., an event could occur once per cycle of operation.
	Condition III Operation – Infrequent incidents, i.e., an event that may occur on a frequency of once during the life of the plant. Some limited fuel failures may occur but are accounted for in radiological dose calculations.
Postulated Accidents (PA) – Postulated events not expected to occur during the life of a nuclear power plant.	
	Condition IV Operation – Limiting faults, i.e., design basis events that are not expected to occur during the life of the plant.

Table 7.1-2 Plant Conditions for Condition I Operation
Condition I occurrences are operations that are expected frequently or regularly in the course of power operation, refueling, maintenance, or maneuvering of the plant. Examples include:
• Steady-state and shutdown operations — Power operation (~15 to 100% of full power) — Startup (or standby) (critical, 0 to 15% of full power) — Hot shutdown (subcritical, Residual Heat Removal System isolated) — Cold shutdown (subcritical, Residual Heat Removal System in operation) — Refueling
• Operational transients including load follow — Plant heatup and cooldown (up to 100°F/hour for the Reactor Coolant System) — Step load changes (up to 10%) — Ramp load changes (up to 5%/minute) — Load rejection up to and including design load rejection transient

Table 7.1-3 Condition II Operation – Incidents of Moderate Frequency
Condition II events shall be accommodated with, at most, a shutdown of the reactor with the plant capable of returning to operation after corrective action. Examples of Condition II events (References 7.5 and 7.6) include:
• Feedwater Malfunctions Causing a Decrease in Feedwater Temperature
• Feedwater Malfunction Causing an Increase in Feedwater Flow
• Excessive Increase in Secondary Steam Flow
• Inadvertent Opening of a Steam Generator (SG) Safety or Relief Valve
• Loss of Electrical Load and/or Turbine Trip
• Loss of Non-Emergency Alternating Current (AC) Power
• Loss of Normal Feedwater
• Partial Loss of Forced Reactor Coolant Flow
• Uncontrolled Rod Cluster Control Assembly (RCCA) Bank Withdrawal from a Subcritical Condition
• Uncontrolled RCCA Bank Withdrawal at Power
• RCCA Mis-Operation (RCCA Misalignment, Rod Drop)
• Startup of an Inactive Reactor Coolant Loop
• Uncontrolled Boron Dilution
• Inadvertent Emergency Core Cooling System (ECCS) Actuation at Power
• Chemical and Volume Control System (CVCS) Malfunction Causing an Increase in Reactor Coolant Inventory
• Inadvertent Opening of a Pressurizer Safety or Relief Valve

Table 7.1-4 Condition III Faults – Infrequent Incidents
Condition III occurrences are faults which may occur very infrequently during the life of a plant. Examples of Condition III events (References 7.5 and 7.6) include:
• Minor Reactor Coolant System Pipe Ruptures
• Minor Secondary System Pipe Breaks
• Complete Loss of Forced Reactor Coolant Flow
• Single Rod Cluster Control Assembly Withdrawal at Power
• Inadvertent Loading of a Fuel Assembly in an Improper Location

Table 7.1-5 Condition IV Faults – Limiting Faults
Condition IV occurrences are faults which are not expected to take place, but are postulated because their consequences would include the potential for the release of significant amounts of radioactive material. Examples of Condition IV faults (References 7.5 and 7.6) include:
• Major Reactor Coolant System Pipe Ruptures
• Major Rupture of a Main Steam Line
• Major Rupture of a Main Feedwater Pipe
• Single Reactor Coolant Pump Locked Rotor
• Rupture of a Control Rod Drive Mechanism Housing (RCCA Ejection)

7.2 FUEL ROD DESIGN INTERFACES REVIEW

Figure 7.2-1 provides a schematic illustration of typical fuel rod design interfaces. Interfaces that provide input to the fuel rod design are described in subsection 7.2.1. Interfaces that receive output from the fuel rod design process are described in section 7.2.2.

a,c

Figure 7.2-1 Schematic Illustration of Typical Fuel Rod Design Interfaces

7.2.1 Fuel Rod Design Input Interfaces

Design input is required from several sources in order to perform fuel rod design analyses using the PAD5 code. In this section, the primary sources of design related input are identified along with a description of the input data that each discipline provides.

7.2.1.1 Product Design & Manufacturing

The fuel rod and fuel assembly mechanical design function establishes the physical parameters required to define the fuel rod. Several components comprise the fuel rod system: the fuel tube, top and bottom end plugs, the fuel pellet stack, spacer components, if required, and pellet stack hold down springs. Figure 7.2-2 illustrates the mechanical components of a fuel rod. Figure 7.2-3 illustrates the **AP1000®** PWR fuel rod lower plenum design. While not an integral part of a fuel rod, the fuel assembly structural grid design is also important for establishing, among other things, the flow channel spacing between fuel rods. The assembly design establishes the spacing between the ends of the fuel rods and the top and bottom nozzles.

The critical dimensions for these components that are needed for PAD5 input are obtained from design drawings for each assembly and all of the components that make up that assembly, including the fuel rods, grids and assembly skeleton. These drawings provide both the nominal dimensions used in fuel rod design and the tolerances that must be considered in the analysis of uncertainties. The types of fuel pellets contained within each rod are also specified. These would include whether there are annular axial blanket pellets in the fuel rod and whether the fuel pellets are UO_2, ZrB_2 coated UO_2, Gd_2O_3-UO_2 or Er_2O_3-UO_2. Information on fuel rod fill gas pressure, pellet U^{235} enrichment, details on integral fuel burnable absorber pellet compositions and nominal fuel density is also obtained from product design documents.

Product and process specifications are another source of design input. Data such as fuel density, fuel pellet sintering temperature, and fill gas composition are obtained from these specifications, including allowances for variability.

When analyses are performed for fuel that has already been fabricated, quality assurance inspection data obtained during the fuel fabrication process may be used as a source of actual component dimensions and associated uncertainties. Measured data are typically available for fuel pellet density, sintering temperature, pellet and cladding diameters and fuel rod plenum length. Other tests, such as pellet thermal stability testing, may also provide input to PAD5.

Westinghouse fuel and cladding fabrication processes are stable and controlled. Quality assurance and process control measurements provide an established characterization of process variability. These historical data may be used to characterize the distributions for key parameters such as pellet and cladding diameter, ZrB_2 coating thickness and B^{10} content, fuel pellet density, plenum length and backfill pressure.

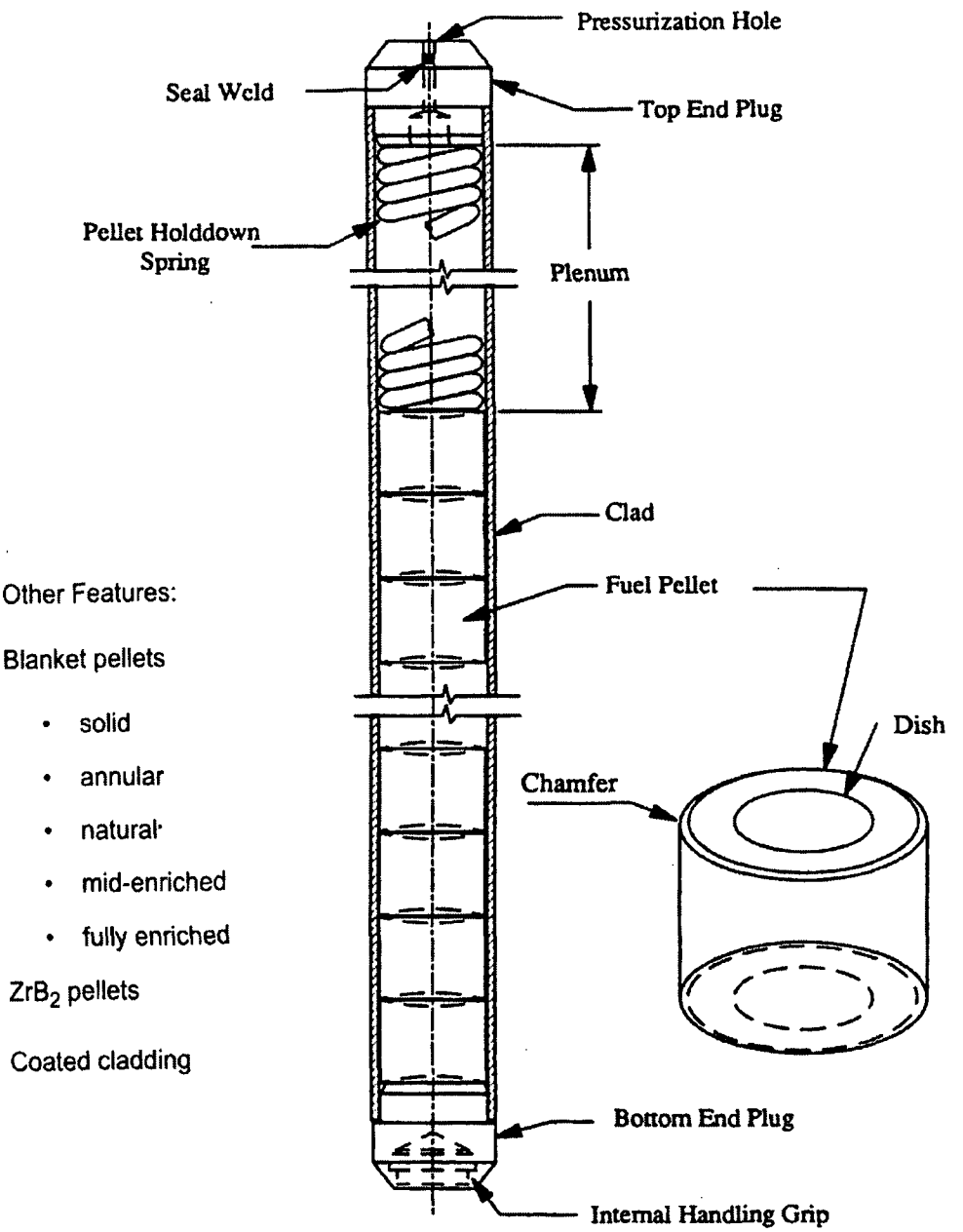

Figure 7.2-2 Illustration of Typical Westinghouse Fuel Rod Components

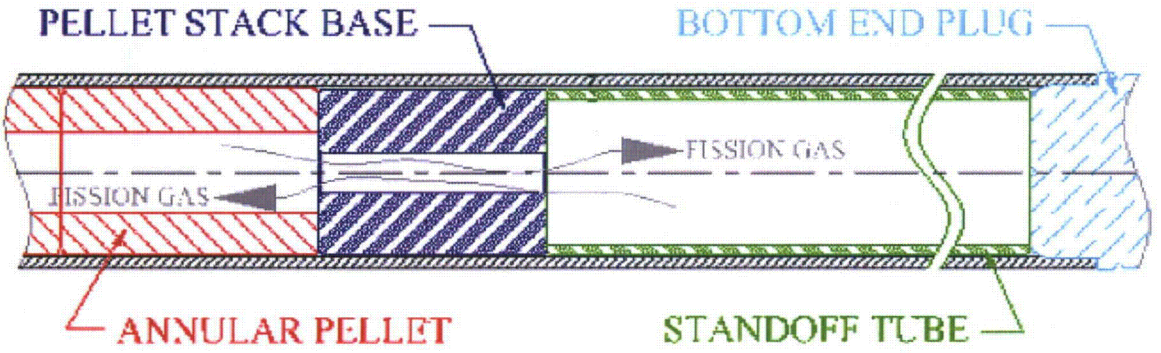

Figure 7.2-3 *AP1000* PWR Fuel Rod Lower Plenum Design

7.2.1.2 Thermal/Hydraulic Design

The core thermal-hydraulic design provides plant operating conditions such as the system pressure, core inlet temperature and coolant mass flow rate. These values may also be obtained or confirmed from plant operation data.

The Thermal/Hydraulic design also identifies Departure from Nucleate Boiling (DNB) transients that are evaluated with respect to the potential for DNB propagation when the rod internal pressure is predicted to exceed the reactor coolant system pressure. DNB transient duty data are used to confirm that maximum cladding strain due to ballooning does not exceed established limits to preclude DNB propagation to neighboring fuel rods, or if some limited DNB propagation is predicted, to account for the radiological dose consequences with consideration of the number of additional rods in DNB due to propagation.

7.2.1.3 Plant Operation

The fuel rod design must account for both the planned operation of fuel in the design cycle and for the past operation of fuel in prior cycles.

Data that may be obtained from prior plant operation includes measured core power, core coolant flow, coolant inlet temperature and core and vessel coolant average temperatures. In the event that a prior operating cycle experienced a Condition II overpower transient, this event may also be accounted for in the fuel rod design.

7.2.1.4 Nuclear Design

Plant operation requirements, such as cycle energy requirements, cycle lengths, number of feed fuel assemblies and feed fuel enrichments are provided to fuel rod design through the interface with the nuclear design function.

In addition, the nuclear design provides the following types of information to the fuel rod design:

- Fuel management data
- Steady state power history data
- Transient power duty
- Fast (E > 1.0 MeV) neutron flux and fluence data, and
- Fuel pellet radial power distribution data

7.2.1.4.1 Fuel Management Data

The nuclear design parameters and the fuel cycling scheme provided by nuclear design form the basis for the anticipated fuel duty over the lifetime of the fuel for the fuel rod design criteria evaluations. The nuclear design parameters specify basic assumptions, such as Technical Specification peaking factor limits (such as $F\Delta H$ and FQ), core average linear heat generation rate, core control strategy, such as Relaxed Axial Offset Control (RAOC) or Constant Axial Offset Control (CAOC), core axial power distribution limits, such as Axial Offset (AO), ΔI or Axial Shape Index (ASI) bands, and cycle lengths (projected for current and design cycles and actual for prior cycles). These parameters are provided for all cycles for which fuel assemblies specified in the design core loading plan have operated.

The upcoming or design cycle loading pattern specifies the fuel assemblies to be included in the core inventory, including the number of assemblies in each fuel batch, U^{235} enrichment(s), and burnable absorber (ZrB_2, Gd_2O_3-UO_2 or Er_2O_3-UO_2) design details. The operating history of each burned fuel assembly (prior cycles in which the fuel assemblies operated) is also identified.

7.2.1.4.2 Steady State Power History Data

Fuel rod power history information provided by nuclear design includes the characterization of time or burnup dependent fuel rod powers and time or burnup dependent axial power shapes. Both are required to establish the steady state fuel rod operating history.

For design and safety analyses, steady state power history data for Westinghouse PWR fuel operation are generated using NRC approved nuclear design codes, such as the Westinghouse Advanced Nodal Code (ANC), Reference 7.7. [

]^{a,c}

[

]^{a,c}

The combination of time dependent rod average powers and time dependent axial power shapes define the steady state power duty expected for each fuel rod or sub-grouping of fuel rods.

a,c

Figure 7.2-4 Illustration of Composite Bounding Power History and Bounding Power History Envelope

7.2.1.4.3 Transient Power Duty

The fuel rod design addresses fuel rod operation under both Condition I and Condition II operation. Condition I and Condition II operational transients are defined to enable the fuel rod design to adequately address the transient fuel duty impact with respect to design limits. The fuel rod design for [

]^{a,c} The nuclear design process provides the input required to model these transients in fuel rod design. The process for generating these transient fuel duty inputs for use in fuel rod design with PAD5 is based on the process described in the licensing for PAD 3.4, Reference 7.8.

A. Condition I Xenon Events

[

]^{a,c}

B. Condition II Transient Duty

[

]^{a,c}

[

]a,c

7.2.1.4.4 Fast Neutron Flux and Fluence Data

Fast neutron flux and fluence (E > 1.0 MeV) input is required for PAD5 to model cladding performance models such as clad axial growth and clad creep. Fast neutron flux data are generated by nuclear design using NRC approved nuclear design codes (such as ANC, Reference 7.7).

7.2.1.4.5 Fuel Pellet Radial Power Distribution Data

As described in Section 3.10, fuel pellet radial power distributions [

]a,c

7.2.2 Fuel Rod Design Output Interfaces

This section provides a summary overview of the flow of fuel rod design analysis results to interfacing disciplines.

7.2.2.1 Nuclear Design

The fuel rod design provides confirmation to nuclear design that the cycle under design can satisfy all fuel rod design criteria, as described in Section 7.4. This confirms the acceptability of the core loading pattern and planned cycle operation with respect to fuel rod design limits.

The fuel rod design may also provide information to nuclear design on available margins to fuel rod design limits to be used in establishing core operating limits. For example, the fuel rod design establishes power to fuel melt limits as a function of burnup that may be used to evaluate the no fuel melting criterion under normal and transient duty conditions. [

]^{a,c}

7.2.2.2 Thermal/Hydraulic Design

Fuel temperature data generated from PAD5 may be used as input for initialization of VIPRE transient calculations performed by Thermal/Hydraulic design, References 7.10 through 7.12.

7.2.2.3 Safety Analysis

The fuel rod design provides input to plant safety analyses. These inputs, described below, are typically provided on a conservative basis for use in bounding safety analyses, and they are then confirmed to remain applicable on a cycle specific basis to ensure that safety analyses of record (AOR) remain valid. Should cycle specific assessments indicate that the fuel rod design inputs used in the AOR are no longer bounding, updated inputs are provided for evaluation and reanalysis, as required, in reload specific safety analyses.

7.2.2.3.1 Non-LOCA

To support non-LOCA safety analyses, the fuel rod design may provide the following data for [

]^{a,c}

[

]^{a,c}

7.2.2.3.2 LOCA

To support loss of coolant accident (LOCA) safety analyses, the fuel rod design may provide the following data for [

]^{a,c}

7.2.2.3.3 Containment & Radiological Analyses

In addition to the fuel temperature data identified above provided for LOCA and Non-LOCA safety analyses, the fuel rod design may provide the following data for each fuel rod type in the core as input to containment and radiological safety analyses:

[

]^{a,c}

[

]^{a,c}

These data may be used as inputs to core mass and energy release calculations and radiological dose calculations.

7.2.2.4 Product Design & Manufacturing

The fuel rod design analyses for new fuel rod designs provide confirmation to product design that fuel rod design limits can be satisfied for the proposed design. For reload fuel designs, fuel rod design specifies the design fill gas pressure for the feed fuel region to manufacturing.

The PAD5 code may also be used to [

]^{a,c}.

7.2.2.5 Fuel Licensing

The fuel rod design provides confirmation to fuel licensing that the fuel rod design satisfies all licensed acceptance limits. Typically this is documented in the reload safety evaluation document or its equivalent.

7.3 FUEL ROD DESIGN METHODS OVERVIEW

The primary function of a fuel rod is to generate and transfer heat to the reactor coolant. In the process of generating this heat via fissioning, both radioactive and stable fission products are produced in the fuel. A second critical function of the fuel rod is to contain these fission products within the rod so that the reactor coolant does not become contaminated. To meet this goal, the structural integrity of the fuel rod must be maintained (i.e., fuel damage or penetration of fuel rod clad is to be precluded).

The integrity of the fuel rods during Condition I and Condition II modes of operation is ensured by designing the fuel rods so that specific design criteria are satisfied. The design process must consider the effects of variations and fluctuations in core and local power, and in reactor coolant temperature, pressure and flow which occur during these Condition I and II modes of operation.

Extremely low probability occurrences which have the potential to cause significant fuel damage are classified as Condition III and Condition IV events. Examples of Condition III events include a small break loss of coolant accident (LOCA), small steam line break, and complete loss of flow. Examples of Condition IV occurrences include the large break LOCA, large steam line break, and rod ejection accident. Fuel rod integrity cannot be guaranteed during these hypothetical occurrences. For these occurrences, analyzed by nuclear safety analysis groups, a failure analysis is conducted and offsite dose calculations are performed as needed to confirm that regulations on radioactive release are satisfied.

This section provides an overview of how Westinghouse fuel rod design methods identify potentially limiting fuel rods for each design criterion, how steady state power histories and transient fuel duty are considered in the fuel rod design, and how uncertainties may be addressed in the fuel rod design.

7.3.1 General Design Considerations

7.3.1.1 Definition of Limiting Rods

Each plant and cycle under design must consider all of the individual fuel rods included in the operation of that cycle. Each fuel rod is defined by the fuel mechanical design, which establishes the initial fuel rod geometry, fuel enrichment, and, if applicable, integral fuel burnable absorber type, and by the operating history of the rod, which is established by the reactor coolant conditions and by the nuclear design for each cycle in which a fuel rod has operated. For each cycle, thousands of fuel rods are considered by fuel rod design, but not every rod is expected to be a limiting rod, and a rod that is limiting for one criterion may not be limiting for other criteria.

Limiting rods are defined as those rods whose predicted performance provides the minimum margin to each of the design criteria. For a number of design criteria a limiting rod is a rod with the maximum power at all times in life or a rod with the maximum accumulated rod average burnup at end of cycle. In other instances it may be a rod with a large power increase from one cycle to the next. In general, no single rod is limiting with respect to all design criteria. The fuel rod design must consider the spectrum of all rod power histories to determine the limiting rods.

7.3.1.2 Allowance for Uncertainties

Uncertainties are accounted for in the design analyses for each of the design criteria. The treatment of uncertainties may utilize one of three possible approaches for each design criterion presented in this section. All proposed approaches are applied in a manner which assures that adequate margin to design limits is maintained.

1. [

]^{a,c}

2. [

]^{a,c}

3. [

]^{a,c}

Westinghouse typically applies a [

]^{a,c}.

7.3.2 Power History Considerations

Subsection 7.2.1.4.2 discussed how the database of fuel rod power histories to be used in fuel rod design is obtained from the interface with nuclear design. Fuel rod design analyses may be performed for [

]^{a,c}

[

]^{a,c}

[

]^{a,c}

7.4 FUEL ROD DESIGN CRITERIA/EVALUATION METHODS

For each fuel rod design criterion, the Design Category, Design Parameter, Design Basis, Acceptance Limit, and Design Evaluation Methodology are summarized. The definitions of these items are:

Design Category – The NRC groups acceptance criteria for design limits into three categories in the SRP (Reference 7.1): Fuel System Damage, Fuel Rod Failure, and Fuel Coolability.

Design Parameter – The specific parameter that will be evaluated.

Design Basis – The reason that the design parameter needs to be considered in the safety evaluation

Acceptance Limit – The acceptance limit is the value that must be demonstrated to be satisfied to satisfy the requirements of SRP Section 4.2 to provide an acceptable margin to fuel failure.

Design Evaluation – A description of the evaluation methods that may be used to evaluate the design or acceptance limits.

7.4.1 Clad Stress

Design Category – Fuel System Damage

Design Parameter – Clad Stress

Design Basis – The fuel system will not be damaged due to excessive fuel clad stress.

Acceptance Limit – Per the NRC approved clad stress criteria for Westinghouse PWR fuel (Reference 7.13), maximum cladding stress intensities excluding pellet clad interaction (PCI) induced stress will be evaluated using American Society of Mechanical Engineers (ASME) boiler and pressure vessel guidelines (Reference 7.14). Cladding corrosion is accounted for as a loss of load carrying material. Stresses are combined to calculate a maximum stress intensity which is then compared to criteria based on the ASME code.

Criteria:

Sm = the minimum of:

- 1/3 σ_{ult} minimum specified at room temperature,
- 1/3 σ_{ult} value at temperature,
- 2/3 σ_y minimum specified at room temperature,
- 2/3 σ_y value at temperature.

Su = the minimum of:

- σ_{ult} minimum specified at room temperature,
- σ_{ult} value at temperature.

where:

σ_y is the 0.2% offset yield strength, with consideration of temperature and irradiation.

σ_{ult} is the ultimate tensile strength, with consideration of temperature and irradiation.

Stress Intensity Limits		
Loading Conditions	**Description**	**Limit**
Pm	Primary Membrane	Sm
Pm + Pb	Primary Membrane + Bending	1.5 Sm
Pm + Pb + Pl	Primary Membrane + Bending + Local	1.5 Sm
Pm + Pb + Pl + Q	Primary Membrane + Bending + Local + Secondary	3.0 Sm

Design Evaluation – These clad stress criteria have been approved by the NRC for Westinghouse PWR applications (Reference 7.13). With the implementation of PAD5, these clad stress criteria will be applied to all US Westinghouse PWR fuel rod designs, with consideration of both Condition I and Condition II operations. These stress criteria conform to the requirements in the SRP, Section 4.2 (Reference 7.1).

The stresses to be considered and the stress category are listed below:

Stress Due To	Stress Category
Differential Pressure	Primary Membrane
Ovality	Primary Bending
Flow Induced Vibration	Primary Bending
Fuel Assembly Bow	Primary Bending
Fuel Rod Bow	Primary Bending
Spacer Grid Contact Force	Primary Local
Thermal Differential across the Cladding	Secondary

The PAD5 fuel performance code documented herein provides input to define the clad stress due to differential pressure considered in this analysis. Rod internal pressure analyses for the limiting fuel rod in the core, with consideration of model, fabrication and operational uncertainties, define the limiting internal pressures at hot and cold conditions for calculation of the primary membrane stress due to

differential pressure. [

]^{a,c}

7.4.2 Clad Strain

Design Category – Fuel Rod Failure/Fuel System Damage

Design Parameter – Clad Strain

Design Basis – The fuel rod will not fail due to excessive fuel clad strain.

Acceptance Limit – The design limit for the fuel rod clad strain is that the total tensile strain, elastic plus plastic, due to uniform cylindrical fuel pellet deformation during any single Condition I or II transient is less than 1% from the pre-transient value.

Design Evaluation – The Westinghouse PAD5 fuel performance code described herein will be used to evaluate margin to clad strain limits. Fuel rod design analyses for clad strain consider the total elastic plus plastic strain calculated based on transient fuel power duty provided by nuclear design, with consideration of model, fabrication and operational uncertainties. [

]^{a,c}

7.4.3 Rod Internal Pressure

Design Category – Fuel System Damage

Design Parameter – Rod Internal Pressure

Design Basis – The fuel system will not be damaged due to excessive fuel rod internal pressure.

Acceptance Limit – The internal pressure of the lead fuel rod in the reactor will be limited to a value below that which could cause the diametral gap to increase due to outward cladding creep during normal (Condition I) operation (Reference 7.15). Extensive DNB propagation will be precluded (References 7.16, 7.17 and 7.18), and the impact of any limited number of fuel rods calculated to be in DNB due to DNB propagation will be included in the radiological dose calculations.

Design Evaluation – The Westinghouse PAD5 fuel performance code described herein will be used to evaluate margin to the rod internal pressure no gap reopening (or gap increasing) limit. [

]^{a,c}

The Westinghouse evaluation of DNB propagation is performed on a mechanistic basis, as approved for Westinghouse NSSS fuel rod designs (Reference 7.16) and for CE NSSS fuel rod designs (References 7.17 and 7.18). Per this methodology, the maximum cladding strain that can occur during a Condition III or Condition IV DNB event is limited to less than [

]^{a,c}. Should DNB propagation be predicted to occur, the additional rods in DNB due to propagation are accounted for in radiological dose calculations. With the implementation of PAD5, mechanistic methods for DNB propagation (Reference 7.16) will be used for all Westinghouse PWR fuel rod designs.

7.4.4 Clad Fatigue

Design Category – Fuel System Damage

Design Parameter – Clad Fatigue

Design Basis – The fuel system will not be damaged due to fatigue.

Acceptance Limit – The fatigue life usage factor is limited to less than 1.0 to prevent reaching the material fatigue limit, considering a safety factor of 2 on stress amplitude or a safety factor of 20 on the number of cycles, whichever is more limiting (Reference 7.19).

Design Evaluation – The PAD5 fuel performance code will be used to determine the cyclic strain ranges for the fatigue life usage analysis. The evaluation of the fatigue limit assumes conservative load follow scenarios over the life of the fuel rod. The Langer O'Donnell fatigue model (Reference 7.20) is used in the fatigue analysis, with the empirical factors of their fatigue model correlation modified in order to conservatively bound the results of Westinghouse testing programs. Design fatigue life was initially based on Westinghouse fatigue test programs for Zircaloy-4 cladding (Reference 7.21) and later validated for ZIRLO (Reference 7.22) and **Optimized ZIRLO** cladding (Reference 7.23). The design equations follow the concept for the fatigue design criterion described in the ASME Boiler and Pressure Vessel Code, Section III.

The PAD5 analyses for clad fatigue include consideration of local cladding defects typically up to
[
]^{a,c}. This local defect is accounted for as a local stress concentration.

7.4.5 Clad Oxidation

Design Category – Fuel System Damage

Design Parameter – Clad Oxidation

Design Basis – The fuel system will be not be damaged due to excessive fuel clad oxidation.

Acceptance Limit – The predicted best estimate, circumferentially averaged oxide thickness of the most limiting axial node shall be no greater than 100 microns, (References 7.24 and 7.25). The maximum Thermal Reaction Accumulated Duty (TRD) for ZIRLO and **Optimized ZIRLO** cladding is restricted to numbers corresponding to a cladding corrosion amount of 100 microns for licensing applications.

Design Evaluation – The cladding oxide thickness is calculated based on the corrosion models summarized in Section 3. These models are incorporated in the PAD5 code, so that the oxide thickness and TRD, if appropriate, are calculated for every axial node as a function of time in PAD5. Analyses to confirm that the acceptance limit is met are performed on a best estimate basis, i.e., using best estimate models and operating conditions. The thermal and mechanical impacts of oxide buildup on the cladding are accounted for in fuel rod design analyses performed with the PAD5 code.

The corrosion model and associated thermal hydraulic models are only a small subset of the models included in the PAD5 code, since the oxide calculation does not require any modeling of fuel and cladding dimensional changes. Clad corrosion analyses may therefore be performed outside of PAD5 using only the thermal models for heat transfer from the clad surface to the coolant and the oxide model to predict clad oxide thickness.

[

]^{a,c}

7.4.6 Clad Hydrogen Pickup

Design Category – Fuel System Damage/Fuel Rod Failure

Design Parameter – Clad Hydrogen Pickup

Design Basis – The fuel system will be operated to prevent significant degradation of mechanical properties of the clad at low temperatures, as a result of hydrogen embrittlement caused by the formation of zirconium hydride platelets.

Acceptance Limit – The best estimate, volume average hydrogen pickup level in the most limiting clad axial node will be less than or equal to [ ]^{a,c} ppm (References 7.24 and 7.25) at the end of fuel operation.

Design Evaluation – The cladding hydrogen content is calculated based on the corrosion and hydrogen pickup models presented in Section 3. These models are incorporated into the PAD5 code, so that the cladding hydrogen is calculated for every axial node as a function of time in PAD5. Best estimate models and operating conditions are used consistent with the acceptance limit definition.

The corrosion and hydrogen pickup models and associated thermal hydraulic models are only a small subset of the models included in the PAD5 code, since the oxide calculation does not require any modeling of fuel and cladding dimensional changes. Clad corrosion and clad hydrogen analyses may therefore be performed outside of PAD5 using only the thermal models for heat transfer from the clad surface to the coolant, the oxide model to predict clad oxide thickness and the hydrogen pickup model to calculate the clad hydrogen based on the oxide thickness.

7.4.7 Fuel Rod Axial Growth

Design Category – Fuel System Damage

Design Parameter – Fuel Rod Axial Growth

Design Basis – The fuel system will be not be damaged due to excessive axial interference between the fuel rods and the fuel assembly structure.

Acceptance Limit – The fuel rods will be designed with adequate clearance between the fuel rod and the top and bottom nozzles to accommodate the differences in the growth of fuel rods and the growth of the assembly without interference.

Design Evaluation – The fuel rod growth models described in Section 5 are used as input to the analyses performed to confirm that the fuel rod axial growth limit is satisfied. Fuel rod growth analyses confirm that sufficient clearance between the fuel rods and the assembly structure will be maintained for the life of the fuel, with consideration of fuel assembly growth and individual component fabrication parameters and associated model uncertainties and manufacturing tolerances.

7.4.8 Clad Flattening

Design Category – Fuel Rod Failure

Design Parameter – Clad Flattening

Design Basis – Fuel rod failures will not occur due to clad flattening.

Acceptance Limit – The fuel rod design shall preclude clad flattening during projected exposure.

Design Evaluation –Westinghouse fabricated fuel is sufficiently stable with respect to fuel densification such that the axial column gaps that can form as a result of fuel densification and axial shrinkage are too small to allow clad flattening to occur and that axial column gaps that could occur are sufficiently small that a densification power spike factor of 1.0 is appropriate (Reference 7.26). These conclusions were based on extensive in-reactor operating experience, with associated on-site (visual examination and flux detector traces) and hot cell (gamma scanning) measured data. It was shown that Westinghouse fabrication processes are well controlled with respect to the parameters that impact fuel densification, such as fuel density, grain size and pore size distribution, such that adverse fuel performance issues associated with fuel densification (clad flattening), as observed in very early PWR fuel operation with densifying UO_2 fuel do not occur.

These conclusions are applicable to current Westinghouse manufactured fuel. The approved (Reference 7.26) process for extending these conclusions to new fuel designs will be implemented based on PAD5 analyses for time of pellet-clad gap closure.

7.4.9 Fuel Pellet Overheating (Power to Melt Only)

Design Category – Fuel Rod Failure

Design Parameter – Fuel Pellet Overheating

Design Basis – The fuel rods will not fail due to fuel centerline melting for Condition I and Condition II events.

Acceptance Limit – The fuel rod centerline temperature shall not exceed the fuel melt temperature during Condition I and II operations, accounting for degradation of the melt temperature due to burnup and the addition of integral burnable absorbers.

Design Evaluation – The Westinghouse PAD5 fuel performance code may be used to evaluate fuel rod centerline temperatures. Analyses are performed to predict best estimate and upper bound fuel centerline temperatures as a function of rod local burnup and power based on a limiting steady state power history. [

]^{a,c} This burnup dependent power to melt limit is used by nuclear design to confirm that fuel centerline melt does not occur during Condition I and II operation.

7.4.10 Pellet/Clad Interaction (PCI)

Design Category – Fuel Rod Failure

Design Parameter – Clad strain and fuel pellet overheating

Design Basis – The fuel rod will not fail due to pellet clad interaction.

Acceptance Limit – The NRC SRP does not require a specific design criterion for PCI. Two related criteria, the one percent clad strain criterion (subsection 7.4.2) and the fuel overheating (no centerline fuel melt) criterion (subsection 7.4.9), must be met.

Design Evaluation – The NRC SRP states that no criterion for fuel failure due to PCI or pellet/clad mechanical interaction (PCMI) currently exists. PCI addresses stress corrosion cracking mechanisms due to fission product embrittlement of the cladding, while PCMI is a stress driven failure mechanism. The one percent uniform clad strain criterion limits the clad strain during a transient to a range where the cladding has sufficient ductility to preclude strain related fuel failures. The fuel pellet overheating criterion precludes fuel melting. The large volume increase in the fuel due to the phase change could result in excessive cladding stresses. Pellet/cladding interaction has not been observed as an active fuel failure mechanism in commercial PWR fuel operation.

7.5 INTERFACE TO SAFETY ANALYSES

The PAD5 code will be used to generate fuel temperature, rod internal pressure and additional fuel and cladding parameter inputs for LOCA and Non-LOCA safety analyses. [

]^{a,c}

This section provides a brief review of the evaluation methods used to generate these inputs.

7.5.1 Fuel Temperatures

[

]^{a,c}

7.5.2 Rod Internal Pressure

The LOCA safety analyses also require steady state fuel rod internal pressure input. For these analyses, [

]^{a,c}

7.5.3 Core Stored Energy

Core stored energy is defined as the amount of energy in the fuel rods in the core above the local coolant temperature. It is calculated based on [

]^{a,c} as required for input to containment analyses and other safety analyses.

7.5.4 Fuel Parameters

Fuel rod parameter data are also provided to nuclear safety. These parameters include [

]^{a,c} as required.

7.6 SECTION 7 REFERENCES

7.1 NUREG-0800, Standard Review Plan for the Review of Safety Analysis Reports for Nuclear Power Plants, Chapter 4.2, "Fuel System Design," March 2007.

7.2 NUREG-0800, Standard Review Plan for the Review of Safety Analysis Reports for Nuclear Power Plants, Chapter 15, "Introduction – Transient and Accident Analyses Review Responsibilities," March 2007.

7.3 ANSI/ANS 51.1-1983, "Nuclear Safety Criteria for the Design of Stationary Pressurized Water Reactor Plants" (replaces ANSI N18.2), Appendix B, 1983 (withdrawn in 1998).

7.4 ANSI N18.2-1973, "Nuclear Safety Criteria for the Design of Pressurized Water Reactor Plants," August 1973.

7.5 US NRC Regulatory Guide 1.70, Revision 3, "Standard Format and Content of Safety Analysis Reports for Nuclear Power Plants – LWR Edition," Section 15, November 1978.

7.6 WCAP-9272-P-A (Proprietary) and WCAP-9273-NP-A (Non-Proprietary), "Westinghouse Reload Safety Evaluation Methodology," July 1985.

7.7 WCAP-10965-P-A (Proprietary) and WCAP-10966-A (Non-Proprietary), "ANC: A Westinghouse Advanced Nodal Computer Code," September 1986.

7.8 WCAP-10851-P-A, (Proprietary) and WCAP-11873-A, (Non-Proprietary), "Improved Fuel Performance Models for Westinghouse Fuel Rod Design and Safety Evaluations," August, 1988.

7.9 WCAP-16045-P-A (Proprietary) and WCAP-16045-NP-A (Non-Proprietary), "Qualification of the Two-Dimensional Transport Code PARAGON," August 2004.

7.10 WCAP-14565-P-A (Proprietary) and WCAP-15306-NP-A (Non-Proprietary), "VIPRE-01 Modeling and Qualification for Pressurized Water Reactor Non-LOCA Thermal-Hydraulic Safety Analysis," October 1999.

7.11 WCAP-15806-P-A (Proprietary) and WCAP-15807-NP-A (Non Proprietary), "Westinghouse Control Rod Ejection Accident Analysis Methodology Using Multi-Dimensional Kinetics," October 2003.

7.12 WCAP-16259-P-A (Proprietary) and WCAP-16259-NP-A (Non-Proprietary), "Westinghouse Methodology for Application of 3-D Transient Neutronics to Non-LOCA Accident Analysis", August 2006.

7.13 WCAP-10125-P-A, Addendum 1-A, Revision 1-A (Proprietary) and WCAP-10125-NP-A, Addendum 1-A, Revision 1-A (Non-Proprietary), "Extended Burnup Evaluation of Westinghouse Fuel, Revision to Design Criteria," May 2005.

7.14 ASME Pressure Vessel Code Section III, Article NG-3000, 1998.

7.15 WCAP-8963-P-A (Proprietary) and WCAP-8964-A (Non-Proprietary), "Safety Analysis for the Revised Fuel Rod Internal Pressure Design Basis," August 1978.

7.16 WCAP-8963-P-A, Addendum 1-A, Revision 1-A (Proprietary) and WCAP-8964-A, Addendum 1-A, Revision 1-A (Non-Proprietary), "Safety Analysis for the Revised Fuel Rod Internal Pressure Design Basis (Departure from Nucleate Boiling Mechanistic Propagation Methodology)," June 2006.

7.17 CEN-372-P-A (Proprietary) and CEN-372-NP-A, "Fuel Rod Maximum Allowable Gas Pressure," May 1990.

7.18 CENPD-404-P-A (Proprietary) and CENPD-404-NP-A (Non-Proprietary), "Implementation of ZIRLO™ Cladding Material in CE Nuclear Power Fuel Assembly Designs," November 2001.

7.19 WCAP-10125-P-A (Proprietary) and WCAP-10126-NP-A (Non-Proprietary), "Extended Burnup Evaluation of Westinghouse Fuel," December 1985.

7.20 W. J. O'Donnell and B. F. Langer, "Fatigue Design Basis for Zircaloy Components," Nuclear Science and Engineering, 20, 1- 12, 1964.

7.21 WCAP-9500-A (Non-Proprietary), "Reference Core Report 17x17 Optimized Fuel Assembly," May 1982.

7.22 WCAP-12610-P-A (Proprietary)and WCAP-14342-A (Non-Proprietary), "VANTAGE+ Fuel Assembly Reference Core Report," April 1995.

7.23 WCAP-12610-P-A & CENPD-404-P-A, Addendum 1-A (Proprietary) and WCAP-14342-A & CENPD-404-NP-A, Addendum 1- A (Non-Proprietary), "**Optimized ZIRLO™**," July 2006.

7.24 WCAP-12610-P-A & CENPD-404-P-A, Addendum 2 "Westinghouse Clad Corrosion Model for ZIRLO™ and **Optimized ZIRLO™**," November 2008.

7.25 Letter from Sher Bahadur (US NRC) to James Gresham (Westinghouse), "Final Safety Evaluation for Westinghouse Electric Company (Westinghouse) Topical Report WCAP-12610-P-A & CENPD-404-P-A, Addendum 2/WCAP-14342-A & CENPD-404-NP-A, Addendum 2, 'Westinghouse Clad Corrosion Model for ZIRLO™ AND **Optimized ZIRLO™** ' (TAC Nos. ME0222 and ME2317)," July 18, 2013.

7.26 WCAP-13589-A (Proprietary) and WCAP-14297-A (Non-Proprietary) "Assessment of Clad Flattening and Densification Power Spike Factor Elimination in Westinghouse Nuclear Fuel," March 1995.

8 PAD5 MODELS AND METHODS IMPROVEMENT PROCESS

The PAD5 fuel performance models and associated evaluation methods described in the prior sections of this report represent the current state of the art for Westinghouse fuel rod design. It is desirable to maintain these models and methods to a high degree of accuracy, since they are the basis for fuel rod design and safety analysis input calculations. Fuel performance models have a theoretical basis, but are also based on a developing technical understanding of material behaviors in-reactor with fitting coefficients to best predict key performance parameters. While much of the empirical database is well established, new performance data are being accumulated due to healthy fuel examinations, ongoing vendor development programs, joint industry test programs, and detailed failed fuel examinations. These new data may reflect an extension of prior test conditions (e.g., power levels, coolant chemistry) or significant improvements in measurement accuracy due to advancing developments in measurement techniques and equipment. As new data are acquired and as in-reactor material behaviors become better understood, improvements in performance models and associated methods may be developed as required to reflect these industry developments. An improvement is defined as a change in a model or method that improves predictions for key performance parameters relative to qualified measured performance data. Improvements may be assessed in terms of bias, ability to match data trends, or scatter (e.g., standard deviation).

The standard model development and licensing process can result in significant delay between the time that new data or new technology are developed and when it can be reflected in design applications. An ongoing model improvement process could lead to multiple submittals of incremental changes to fuel performance models and associated methods. The full review and approval process requires extensive time and resources, making incremental improvements impractical. The consequence can be that once models are approved by the NRC they remain fixed until there is sufficient safety and/or commercial incentive to engage in the model improvement and licensing process.

Fuel performance model and method improvements are developed under a controlled process with established documentation and verification and internal review following the Westinghouse Quality Management System. This section defines how this process will be applied to provide for a streamlined Models and Methods Improvement Process (MMIP) for models and methods improvements that satisfy established applicability criteria. Improvements that satisfy these applicability criteria may be implemented in design applications following NRC notification of the model(s) and/or method(s) change. Improvements that don't satisfy the applicability criteria for the MMIP would follow the standard licensing process, requiring NRC review and approval prior to implementation.

Section 8.1 summarizes the Westinghouse fuel rod performance model and design application method improvement process. The MMIP applicability criteria for determining the appropriate approval path for model and method improvements are defined in Section 8.2. The model and method improvement licensing process flow is defined in more detail in Section 8.3.

This PAD5 MMIP provides an alternative to the Westinghouse Fuel Criteria Evaluation Process (FCEP) methodology for fuel and cladding model updates outlined in Chapter 7 of Reference 8.1. The FCEP will continue to be applied for implementing fuel design changes as explained in Reference 8.1.

8.1 FUEL PERFORMANCE MODEL AND METHOD IMPROVEMENT PROCESS

8.1.1 Process Fundamentals

The fundamental objective of Westinghouse fuel rod design is to assure that:

1. The fuel system is not damaged as a result of normal operation and anticipated operational occurrences;

2. Fuel system damage is never so severe as to preclude control rod insertion when required;

3. The number of fuel rod failures is not underestimated for postulated accidents; and

4. Core coolability is always maintained.

Section 7.4 identifies the acceptance limits that must be met by the fuel rod design during Condition I and Condition II operation. Condition III and IV events are addressed by Westinghouse safety analysis methods.

To perform design analyses, fuel and cladding material property and in-reactor performance models are developed and incorporated into integrated software (e.g., PAD5 as described in Sections 3 through 6) to predict key fuel and cladding performance parameters. These models are generally developed on a best estimate basis by adjusting the performance model coefficients to best fit qualified measured fuel and cladding performance data with minimal bias. (The data qualification process is discussed in more detail in subsection 8.1.2.) Model performance trends are evaluated to confirm that there are no systematic biases with respect to key model inputs (e.g., fuel burnup, temperature, fluence). Engineering judgment may be used to determine if it is appropriate to allow a conservative model bias, based on evaluation of the sufficiency and/or quality of the measured data. Following completion of model development, model uncertainties are defined to bound at least 95% of the qualified database (i.e., the upper bound model will predict a value greater than or equal to the measured value for at least 95% of the relevant measured data points). In some cases, the model uncertainty may include multiple contributors, when it is not possible to separate out the contributions of uncertainty components. For example, measurement uncertainty in fission gas release measurements may not be adequately defined to justify removing it from the total fission gas release uncertainty.

Design methods are established to specify how design and safety analyses are to be performed to ensure safe and reliable fuel operation. For each type of analysis, appropriate input requirements are defined, including consideration of operating duty. Interfaces with other design disciplines are established to assure that inputs used in the analysis are consistent with their intended use. Basic assumptions are stated to define the limits of applicability of the methods. The treatment of model, fabrication and operational uncertainties is defined to ensure that significant uncertainties are accounted for. For each design parameter (e.g., rod internal pressure or clad strain), sensitivity studies are performed to identify those uncertainties that significantly impact that parameter. These studies consider the typical range of operating duty over which design analyses are performed. All uncertainty parameters that produce a significant impact on the design parameter are included in the design application methods for analysis of that parameter.

The model and method development process is performed in a controlled manner, with appropriate internal documentation and verification as per the Westinghouse Quality Management System.

8.1.2 Development Process

Fuel rod performance models are verified and validated against qualified experimental data. Methods used to perform fuel rod design analysis and to generate inputs to safety analysis have been defined based on established performance code response to models, fuel and cladding fabrication parameters, and plant operation inputs, with appropriate consideration of established uncertainties.

It is the objective of the model and methods development process to maintain or improve the accuracy of the fuel rod performance models and associated methods, with consideration of new fuel and cladding performance data and associated technical development in the understanding of fuel and cladding performance mechanisms and modeling techniques.

New fuel performance data continue to be obtained by Westinghouse and the nuclear industry. Much of this data for commercial reactor fuel is the result of healthy fuel examinations that are intended to validate continued good fuel performance while providing a means to identify potential performance concerns before they impact fuel performance in reactor. More detailed fuel and cladding examinations may be performed when fuel rod failures occur to identify cause of failure. Vendor specific and joint industry test programs are also conducted to further establish current fuel and cladding performance trends under more challenging operating conditions, to provide confirmatory data to validate established performance trends, and to investigate new fuel and cladding material behaviors. All of these data sources are subject to measurement and operational uncertainties, such that the data must be qualified.

The initial step for data review and qualification is to assess the new data relative to known trends for each measured parameter of interest. Data that trends as expected provides added confirmation that current performance models are performing accurately. When data exhibit a deviation from expected trends, a more detailed review of the test series or measurement campaign may be required. The purpose of this review is to validate the experimental procedures, (i.e., calibration and data reduction) to confirm consistency with those used to establish the existing database. The operating history of the fuel rods under examination relative to the operating history for rods in the existing database is also reviewed to identify potential differences that could explain the deviation in the trends. Manufacturing information for the test rods may also be reviewed to verify consistency with the database. The objective of these initial reviews is to verify that the measured data are valid, to establish the relevance of the data with respect to design applications, and to further confirm whether the observations are consistent with the known uncertainties in the current performance models.

Data that exhibit unexpected trends may require further validation before being included in the model development database. Additional measurements or measurement campaigns may be conducted to obtain additional data under similar operating conditions to confirm that the initial observations are valid. The extent of these additional investigations is dependent on the potential significance of the observed performance trend. Once sufficient data have been accumulated that validates the initial observations, and appropriate reviews of the measurements have been completed and documented, the data are qualified for use in assessing fuel rod design and performance impacts. Westinghouse internal procedures, such as the Westinghouse corrective action process, are used as required to document and track the observations and

the resolution with respect to design and safety impacts. Any observations that could adversely impact nuclear safety would be addressed consistent with the requirements of 10 CFR 21.

In addition to new data acquisition, fuel and cladding performance modeling technology is also under development both within Westinghouse and throughout the industry. Westinghouse participates with utilities individually and collectively in the development of increased understanding of in-reactor material behaviors and improvement in fuel performance modeling. Joint industry projects that sponsor ongoing in-reactor test programs also provide a forum for the discussion and development of fuel performance modeling technology. New modeling approaches may be investigated to determine if the accuracy of the predictions may be improved by reducing the variability in predicted versus measured results for the existing database and/or for improving predictions for new qualified measurement data.

Modifications to existing analysis methods may also be developed as part of improvement in the database and fuel performance technology. These methods improvements may be initiated in response to model improvements or modifications to plant operation strategies, to improve the accuracy of design and safety analyses, or to reduce the cycle time for performing design analyses. Methods modifications may also be required to provide additional input to safety analysis in response to emerging issues or changes in regulatory requirements. The modified methods must still satisfy the fundamental objective of the design process which is to assure the all fuel rod design and safety limits are satisfied with appropriate consideration of all significant uncertainties.

As models and/or methods improvements are identified and developed, the potential impact of methods improvements on plant safety and operation is assessed. Improvements that could adversely impact design and/or safety margins are tracked using the Westinghouse corrective action process.

As improvements to fuel performance models and methods are developed, the licensing requirements for implementation of these improvements must be addressed. The first step in this evaluation is to apply the MMIP applicability criteria presented in Section 8.2 to determine whether the improvements can be implemented under the MMIP streamlined process. Under the streamlined MMIP, after the model and methods development is completed within Westinghouse with appropriate documentation, independent verification and internal review requirements satisfied, the model and/or method improvements are summarized in a notification letter that is transmitted to the US NRC. In addition to the description of the improvement to be implemented, this letter will identify when the improvements are expected to be implemented in design application. Explicit NRC review and approval is not required under the streamlined process. If the MMIP applicability requirements in Section 8.2 are not satisfied, appropriate NRC review and approval of the changes must be obtained prior to use in Westinghouse design applications.

8.2 STREAMLINED MMIP APPLICABILITY CRITERIA

The streamlined process for fuel performance model and method improvements may be followed provided that the following applicability criteria are satisfied:

- [ ]^{a,c}
- [ ]^{a,c}
- [ ]^{a,c}
- [ ]^{a,c}

8.3 MODEL & METHOD IMPROVEMENT PROCESS SUMMARY

Figure 8.3-1 provides a schematic illustration of the Westinghouse fuel performance model and method licensing process.

Potential model and method improvements are defined based on ongoing data acquisition and qualification efforts and fuel performance technology developments. The decision to pursue specific model and method improvements is the responsibility of Westinghouse management based on the safety significance of the proposed improvements and other considerations. Once an improvement is accepted for development, the proposed changes are evaluated relative to the MMIP applicability criteria to determine the required licensing path.

Model and / or method development is then completed, with all appropriate testing, documentation, independent verification, and internal reviews. This stage of the development process is the same regardless of the licensing path that is determined from the MMIP applicability criteria review.

The licensing phase follows completion of the development effort. If the standard licensing process is required based on the MMIP applicability criteria or if it is deemed appropriate to request explicit NRC review and approval, appropriate licensing documentation will be developed to present the improvements to the NRC. Implementation of the change would then follow the completion of the NRC review and approval. If the model and/or method improvements satisfy the streamlined process criteria, a letter summarizing the improvements and the implementation plan will be sent to NRC for information only. No explicit review and approval is required by the NRC under the streamlined process, though the NRC may elect to audit the improvement development process.

Following completion of licensing requirements, the model and method improvements will be implemented in Westinghouse PWR fuel rod design and safety analyses, typically on a forward fit basis. After this PAD5 topical report becomes part of a plant's licensing basis, an improvement implemented under the streamlined process described in this section is not considered to be a departure from a method of evaluation described in the Final Safety Analysis Report (FSAR) (as updated) used in establishing the design bases or in the safety analyses. Therefore, changes to PAD5 models or methods using the streamlined MMIP do not result in a departure from a method of evaluation as defined in 10 CFR 50.59(a)(2).

8.4 PROCESS APPLICATION

[

]^{a,c}

a,c

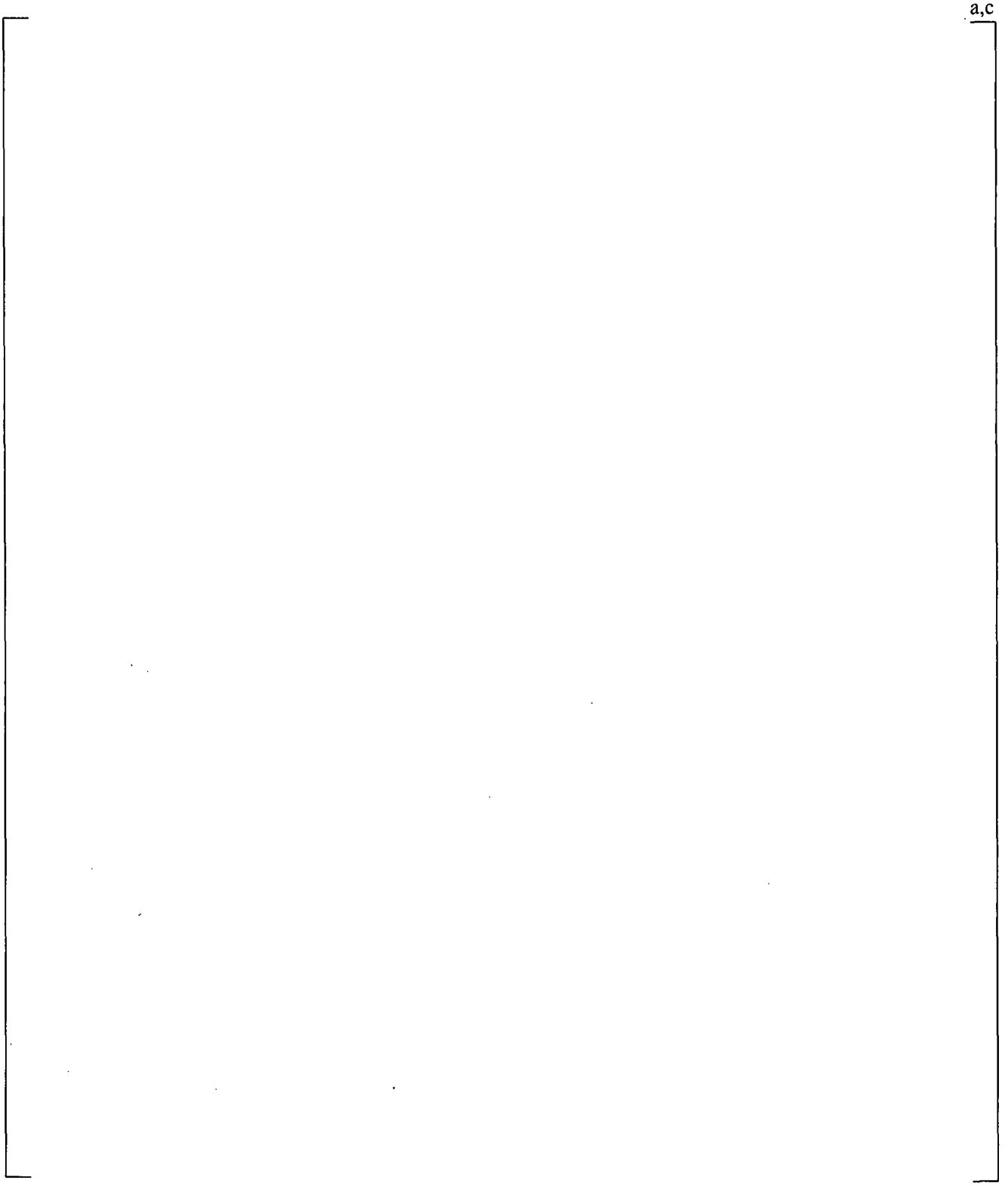

Figure 8.3-1 PAD5 Fuel Performance Models and Methods Improvement Licensing Process Map

8.5 SECTION 8 REFERENCES

8.1 WCAP-12488-A (Proprietary) and WCAP-14204-A (Non-Proprietary), "Westinghouse Fuel Criteria Evaluation Process," October 1994.

APPENDIX A
PAD5 CALIBRATION/VALIDATION/UNCERTAINTY RESULTS

A.1 CALIBRATION PROCESS

A.1.1 Description of the Model Calibration Process

Many fuel rod performance models and material properties can be independently validated against measured data because they do not depend on or are only weakly dependent on the interrelated effects of the other fuel rod models. No integral code calibration is required to validate these models and material properties. These models and material properties include the cladding Young's modulus, cladding Poisson's ratio, fuel and cladding thermal expansion, cladding yield strength and ultimate strength, cladding and oxide thermal conductivity, cladding oxide thickness, and rod growth. However, certain models are more strongly dependent on how the overall code responds, and thus will be validated by an integral code calibration. Such models each have a direct impact on the following important fuel rod performance parameters:

- Fuel centerline temperature
- Steady state and transient fission gas release
- Cladding creep and deformation
- Fuel rod internal void volume.

An integral code calibration was performed as described in this appendix by evaluating these fuel rod performance parameters. The models that most strongly influence the calibration for the specific fuel rod performance parameter are discussed below.

Table A.1-1 summarizes the detailed PAD5 integral calibration steps and describes which model is primarily used to tune and optimize the best estimate predictions. The dependent fuel rod performance parameters of interest listed above (e.g. fuel centerline temperature) have been considered over specific ranges of fuel rod condition (e.g. open fuel-cladding gap) and operation (e.g. burnup or during power ramps). Each primary model is tuned to predict the calibration database for the fuel performance parameter of interest on [

]^{a,c} The process is repeated as necessary to converge on the final set of calibrated models.

Table A.1-1 PAD5 Integral Calibration Strategy

Fuel Rod Performance Parameter	Primary Model Used for Code Calibration

a,c

Table A.1-1 PAD5 Integral Calibration Strategy (cont.)	a,c
Fuel Rod Performance Parameter	**Primary Model Used for Code Calibration**

The detailed calibration process for:

- fuel temperature,
- fission gas release,
- cladding creep,
- cladding diameter in response to ramp tests, and
- integral calibration confirmation
  - cladding outer diameter due to steady state operation to high burnup,
  - rod internal cold void volume at high burnup

is described in the following sections of this appendix. In each of these sections is an explanation of the calibration that has been performed, a description of the database used to perform the calibration, a presentation of the results of the calibration, and a description of the uncertainties, if appropriate, associated with the calibration.

The databases for each calibration category will be divided into calibration and validation sets, indicated by C and V in the tables listing the calibration and validation datasets in each fuel rod parameter calibration section that follows. [

]^{a,c}

A.1.2 Process for Generation of Model Uncertainties

The process of generating the PAD5 model uncertainties from the calibration data is based on the following process. For each fuel performance parameter or model for which an uncertainty is desired for

use in design analysis, [

]^{a,c}

This process is conservative because the resulting model uncertainties will [

]^{a,c}

The following sections of this appendix include a description of the uncertainties, if appropriate, associated with the calibration of the fuel performance parameter in that section.

A.2 CALIBRATION RESULTS

A.2.1 Fuel Temperatures

A.2.1.1 Thermal Database

The thermal database used to calibrate PAD5 fuel centerline temperatures has been significantly expanded from that used for PAD 4.0 (Reference A.34). New high burnup data has been included from [

]^{a,c} Table A.2.1-1 lists the available tests for the thermal calibration and validation of PAD5 and provides references to the reports where the experiments are described. While many rods have been added to the thermal database, others were excluded for a variety of reasons. These rods have been listed in Table A.2.1-2 along with justifications for their exclusion.

Table A.2.1-1 PAD5 Thermal Calibration Database Test Program Reports

Test	Number of Rods	Reference(s)

a,b,c

Table A.2.1-2 Rods Excluded from Thermal Database

Tests	Rod ID(s)	TC/ET	Reason for Exclusion

a,b,c

Table A.2.1-2 Rods Excluded from Thermal Database (cont.)

Tests	Rod ID(s)	TC/ET	Reason for Exclusion

a,b,c

[

]^{a,c} The resulting database is shown in Table A.2.1-3, along with rod design parameters relevant to temperature predictions. The PAD5 thermal database includes both thermocouple measurements and expansion thermometer measurements. The column labeled 'TC/ET' refers to the temperature measuring device: TC for thermocouple (local centerline temperatures) or ET for expansion thermometer (axially averaged centerline temperatures).

Table A.2.1-3 Summary of Rods in PAD5 Thermal Database

Plant/Program	Rod ID	TC/ ET	Gap[(1)] (mil)	Fill Gas	Backfill Pressure (psi)	EOL RABU[(2)] (MWd/MTU)	C/V	Gad (%)

a,b,c

Table A.2.1-3 Summary of Rods in PAD5 Thermal Database (cont.)

Plant/Program	Rod ID	TC/ ET	Gap[1] (mil)	Fill Gas	Backfill Pressure (psi)	EOL RABU[2] (MWd/MTU)	C/V	Gad (%)

a,b,c

Table A.2.1-3 Summary of Rods in PAD5 Thermal Database (cont.)

Plant/Program	Rod ID	TC/ ET	Gap[(1)] (mil)	Fill Gas	Backfill Pressure (psi)	EOL RABU[(2)] (MWd/MTU)	C/V	Gad (%)

a,b,c

Notes:

1. As-fabricated pellet-cladding diametral gap
2. End of Life Rod Average Burnup
3. Including extended operation to high burnup
4. [ ]^{a,b,c}

The database described in Table A.2.1-3 contains [ ]^{a,c}. However, points with measured temperatures [ ]^{a,c} These points do not sufficiently exercise the code calculation of temperature rise and contribute little to the thermal model development. [ ]^{a,c} Table A.2.1-4 provides further information of the distribution of data in the thermal database.

Table A.2.1-4 Distribution of the Number of Rods and Data Points in the PAD5 Thermal Database

Role	All Fuel		UO_2		Gadolinia	
	Rods	Data Points	Rods	Data Points	Rods	Data Points

a,b,c

In addition to the thermal model database described in Table A.2.1-3, the results of the [ ]^{a,b,c} The predictions obtained with PAD5 are compared to the results of the experiment in Section A.2.1.2.

A.2.1.2 Thermal Model Results

Thermal Model Calibration and Validation

As discussed in Section A.1.1, the first step in the thermal model calibration process was calibrating the thermal model to match BOL data. [

]^{a,c} The data used for BOL calibrations included data [ ]^{a,c}

Figures A.2.1-1 through A.2.1-6 show BOL thermal calibration results. The figures present plots of predicted versus measured temperature results as well as residual graphs (predicted minus measured temperatures) versus LHGR. Separate plots are presented for the calibration and validation datasets, as well as for the entire database combined. The plots show good overall agreement between measurements and predictions. No anomalous trends with increasing LHGR are seen.

Note that thermocouple data points are a function of local values, while expansion thermometer data points are a function of rod average values. The figures themselves are an aggregate of local and rod average values for the quantities involved.

a,b,c

Figure A.2.1-1 Predicted vs. Measured BOL Fuel Centerline (FCL) Temperatures for the Calibration Database

a,b,c

Figure A.2.1-2 Predicted Minus Measured BOL Fuel Centerline Temperatures vs. LHGR for the Calibration Database

a,b,c

Figure A.2.1-3 Predicted vs. Measured BOL Fuel Centerline Temperatures for the Validation Database

a,b,c

Figure A.2.1-4 Predicted Minus Measured BOL Fuel Centerline Temperatures vs. LHGR for the Validation Database

a,b,c

Figure A.2.1-5 Predicted vs. Measured BOL Fuel Centerline Temperatures for the Calibration and Validation Database.

a,b,c

Figure A.2.1-6 Predicted Minus Measured BOL Fuel Centerline Temperatures vs. LHGR for the Calibration and Validation Database

[

]^{a,c}

Figures A.2.1-7 through A.2.1-15 show calibration and validation results for fuel centerline temperature from all burnups throughout life, including burnups below 500 MWd/MTU. The figures are organized in sets of three for each database subset. Each set includes the following:

- Predicted versus measured fuel centerline temperatures,
- Predicted minus measured fuel centerline temperature residuals versus LHGR, and
- Predicted minus measured fuel centerline temperature residuals versus burnup.

Figures A.2.1-7 through A.2.1-9 show results for UO_2 fuel (calibration and validation datasets).

Figures A.2.1-10 through A.2.1-12 show results for gadolinia fuel (calibration and validation datasets).

Figures A.2.1-13 through A.2.1-15 show results for UO_2 and gadolinia fuel combined.

Table A.2.1-5 provides statistics for PAD5 thermal calibration and validation.

Table A.2.1-5 Statistics for the Predicted Minus Measured (P-M) Residuals in the PAD5 Thermal Calibration and Validation

	All Fuel			UO_2			Gadolinia		
Role	Data Points	P-M Average (°F)	P-M Standard Dev. (°F)	Data Points	P-M Average (°F)	P-M Standard Dev. (°F)	Data Points	P-M Average (°F)	P-M Standard Dev. (°F)

a,b,c

a,b,c

Figure A.2.1-7 Predicted vs. Measured In-Life Fuel Centerline Temperatures for the UO_2 Calibration and Validation Database

a,b,c

Figure A.2.1-8 Predicted Minus Measured In-Life Fuel Centerline Temperatures vs. LHGR for the UO_2 Calibration and Validation Database

a,b,c

Figure A.2.1-9 Predicted Minus Measured In-Life Fuel Centerline Temperatures vs. Burnup for the UO_2 Calibration and Validation Database

a,b,c

Figure A.2.1-10 Predicted vs. Measured In-Life Fuel Centerline Temperatures for the Gadolinia Calibration and Validation Database

a,b,c

Figure A.2.1-11 Predicted Minus Measured In-Life Fuel Centerline Temperatures vs. LHGR for the Gadolinia Calibration and Validation Database

a,b,c

Figure A.2.1-12 Predicted Minus Measured In-Life Fuel Centerline Temperatures vs. Burnup for the Gadolinia Calibration and Validation Database

a,b,c

Figure A.2.1-13 Predicted vs. Measured In-Life Fuel Centerline Temperatures

a,b,c

Figure A.2.1-14 Predicted Minus Measured In-Life Fuel Centerline Temperatures vs. LHGR for the UO_2 and Gadolinia Database

a,b,c

Figure A.2.1-15 Predicted Minus Measured In-Life Fuel Centerline Temperatures vs. Burnup for the UO_2 and Gadolinia Database

It is concluded from Figures A.2.1-1 through A.2.1-15 that:

1. There are no anomalous trends with burnup (as shown in Figures A.2.1-9, A.2.1-12, and A.2.1-15) or LHGR (as shown in Figures A.2.1-2, A.2.1-4, A.2.1-6, A.2.1-8, A.2.1-11, and A.2.1-14) for any of the datasets.

2. There are no significant differences in the quality or behavior of the predictions for gadolinia and UO_2 rods. This is also seen in the statistics shown in Table A.2.1-5.

3. The validation dataset shows a somewhat larger scatter, but otherwise the results are similar to those seen in the calibration dataset (as shown in Figures A.2.1-7 through A.2.1-10)

4. For burnups [ ]^{a,c} (as shown in Figure A.2.1-15), and the average value of the predicted minus measured residuals is [ ]^{a,c}. This confirms that the degradation of the fuel thermal conductivity with burnup has been adequately modeled.

5. A significant number of points are contained [ ]^{a,c} (as shown in Figures A.2.1-14 and A.2.1-15).

Therefore, based on the results and discussion presented in this section and in Figures A.2.1-1 through A.2.1-15, it is concluded that the PAD5 code fuel temperatures are generally in [
]^{a,c}

Comparison with the Results from the HBC Power-to-Melt Test

As described earlier, the results of [

]^{a,b,c}

For the UO_2 rod, [

]^{a,b,c}

Figures A.2.1-16 and A.2.1-17 show the PAD5 calculated radial fuel temperature profile for the UO_2 rod at nodes 8, and 11, respectively. Node 7 had essentially equivalent conditions as did node 8 and the results obtained for both nodes are also essentially equivalent. Fuel melting temperatures as calculated using the correlation in Equation (6-14), Section 6.1.5 are also shown in each figure for comparison.

The analysis shows that PAD5 predicts [
]^{a,b,c} The results obtained with PAD5 for the UO_2 rod are consistent with the observations reported for this rod.

For the gadolinia rod, [

]^{a,b,c}

[

]^{a,b,c}

Figure A.2.1-18 shows the calculated radial fuel temperature profile for the gadolinia rod at node 8 [ ]^{a,c} and Figure A.2.1-19 show the result for [ ]^{a,c} With the fuel melt temperature calculated using Equation (6-15) in Section 6.1.5, [ ]^{a,c}

These direct melting point comparisons show that PAD5 is acceptable for predicting high fuel temperatures approaching fuel melting.

a,b,c

Figure A.2.1-16 Pellet Temperature Results for Nodal Elevation 8 of the UO_2 Rod of the HBC Test

a,b,c

Figure A.2.1-17 Pellet Temperature Results for Nodal Elevation 11 of the UO_2 Rod of the HBC Test

a,b,c

Figure A.2.1-18 Pellet Temperature Results for Node 8 of the Gadolinia Rod of the HBC Test with More Surface Peaked Radial Power Distribution

a,b,c

Figure A.2.1-19 Pellet Temperature Results for Node 8 of the Gadolinia Rod of the HBC Test with Less Surface Peaked Radial Power Distribution

A.2.1.3 Thermal Calibration Uncertainties

Upper and lower bound uncertainties were developed from the [
]^{a,c} It is observed that the prediction residuals for the cases [

]^{a,c}

[

]^{a,c}

For the predicted [ ]^{a,c} data, the upper-bound temperatures are calculated as:

$$\left[\right]^{a,c} \quad \text{(A.2-1)}$$

For the predicted [ ]^{a,c} data, the upper-bound temperatures are calculated as:

$$\left[\right]^{a,c} \quad \text{(A.2-2)}$$

For the predicted [ ]^{a,c} data, the lower-bound temperatures are calculated as:

$$[\quad \overset{a,c}{\quad} \quad] \qquad \text{(A.2-3)}$$

For the predicted [ ]^{a,c} data, the lower-bound temperatures are calculated as:

$$[\quad \overset{a,c}{\quad} \quad] \qquad \text{(A.2-4)}$$

where:

T_{BE} is the best-estimate temperature predicted by PAD5 (°F),
T_{UB} is the temperature to be used as upper-bound (°F),
T_{LB} is the temperature to be used as lower-bound (°F), and
[ ]^{a,c}

Figures A.2.1-20 through A.2.1-23 show the predicted minus measured temperature residuals calculated using the biased temperatures for upper and lower bound settings, as a function of LHGR and as a function of burnup.

a,b,c

[ ]

Figure A.2.1-20 Upper-Bound Fuel Centerline Temperatures Predicted Minus Measured vs. LHGR

a,b,c

Figure A.2.1-21 Upper-Bound Fuel Centerline Temperatures Predicted Minus Measured vs. Burnup

a,b,c

Figure A.2.1-22 Lower-Bound Fuel Centerline Temperatures Predicted Minus Measured vs. LHGR

a,b,c

Figure A.2.1-23 Lower-Bound Fuel Centerline Temperatures Predicted Minus Measured vs. Burnup

A.2.2 Fission Gas Release

A.2.2.1 Fission gas release database

The PAD5 UO_2 fueled steady state Fission Gas Release (FGR) database, the UO_2 fueled transient FGR database, and the UO_2-Gd_2O_3 fueled steady state and transient FGR database are described in this section. Table A.2.2-1 summarizes the industry available FGR measurements by data set, which has been combined with Westinghouse's own data. In reviewing and modeling these data, PAD5 models did not accurately model certain datasets due to atypical fuel feature or behavior. The data summarized in Table A.2.2-2 will be excluded from calibration and validation, with justification for the dataset exclusion.

Table A.2.2-1 FGR Test Program by Data Set

Validation Data Set	Number of Rods	References

a,b,c

Table A.2.2-2 Data Sets Excluded from Calibration and Validation

Test Program/Rods	Atypical Fuel Feature and Behavior	Reason for Exclusion

a,b,c

The PAD5 steady-state UO_2 fission gas release data has been [

]^{a,c}. It should be noted that [

]^{a,c}

There are [

]^{a,c}. The rods in each of these databases are listed in Tables A.2.2-3 (Thermal FGR database), A.2.2-4 (High Burnup Athermal FGR database), and A.2.2-5 (Low Burnup Athermal FGR database).

Table A.2.2-3 PAD5 FGR Model Calibration Results: Thermal FGR Database

Plant/Program	Rod ID	Rod Burnup (MWd/MTU)	Measured FGR (%)	Predicted FGR (%)	C/V

a,b,c

Table A.2.2-3 PAD5 FGR Model Calibration Results: Thermal FGR Database (cont.)

Plant/Program	Rod ID	Rod Burnup (MWd/MTU)	Measured FGR (%)	Predicted FGR (%)	C/V

a,b,c

Table A.2.2-3 PAD5 FGR Model Calibration Results: Thermal FGR Database (cont.)

Plant/Program	Rod ID	Rod Burnup (MWd/MTU)	Measured FGR (%)	Predicted FGR (%)	C/V

a,b,c

Table A.2.2-4 PAD5 FGR Model Calibration Results: High Burnup Athermal FGR Database

Plant/Program	Rod ID	Rod Burnup (MWd/MTU)	Measured FGR (%)	Predicted FGR (%)	C/V

a,b,c

Table A.2.2-4 PAD5 FGR Model Calibration Results: High Burnup Athermal FGR Database (cont.)

Plant/Program	Rod ID	Rod Burnup (MWd/MTU)	Measured FGR (%)	Predicted FGR (%)	C/V

a,b,c

Table A.2.2-4 PAD5 FGR Model Calibration Results: High Burnup Athermal FGR Database (cont.)

Plant/Program	Rod ID	Rod Burnup (MWd/MTU)	Measured FGR (%)	Predicted FGR (%)	C/V

a,b,c

Table A.2.2-4 PAD5 FGR Model Calibration Results: High Burnup Athermal FGR Database (cont.)

Plant/Program	Rod ID	Rod Burnup (MWd/MTU)	Measured FGR (%)	Predicted FGR (%)	C/V

a,b,c

Table A.2.2-5 PAD5 FGR Model Calibration Results: Low Burnup Athermal FGR Database

Plant/Program	Rod ID	Rod Burnup (MWd/MTU)	Measured FGR (%)	Predicted FGR (%)	C/V

a,b,c

Table A.2.2-5 PAD5 FGR Model Calibration Results: Low Burnup Athermal FGR Database (cont.)

Plant/Program	Rod ID	Rod Burnup (MWd/MTU)	Measured FGR (%)	Predicted FGR (%)	C/V

a,b,c

Table A.2.2-5 PAD5 FGR Model Calibration Results: Low Burnup Athermal FGR Database (cont.)

Plant/Program	Rod ID	Rod Burnup (MWd/MTU)	Measured FGR (%)	Predicted FGR (%)	C/V

a,b,c

There are [ ]^{a,c} in the UO_2 fueled transient fission gas release database. Note that rods with less than 3% measured FGR were not used as part of calibration or validation, however, they were used as part of the uncertainty evaluation. The rods in each of these databases are listed in Table A.2.2-6 (Transient FGR database).

Table A.2.2-6 PAD5 FGR Model Calibration Results: Transient FGR Database

Plant/Program	Rod ID	Rod Burnup (MWd/MTU)	Measured FGR (%)	Predicted FGR (%)[1]	C/ V	Refabricated

a,b,c

Table A.2.2-6 PAD5 FGR Model Calibration Results: Transient FGR Database (cont.)

Plant/Program	Rod ID	Rod Burnup (MWd/MTU)	Measured FGR (%)	Predicted FGR (%)[1]	C/ V	Refabricated

a,b,c

Table A.2.2-6 PAD5 FGR Model Calibration Results: Transient FGR Database (cont.)

Plant/Program	Rod ID	Rod Burnup (MWd/MTU)	Measured FGR (%)	Predicted FGR (%)(1)	C/ V	Refabricated

a,b,c

Note:
1. Predicted FGR values are the FGR due to [ ]^{a,c}

There are [ ]^{a,c} in the gadolinia fuel fission gas release database ([ ]^{a,c}). The rods in each of these databases are listed in Tables A.2.2-7 and A.2.2-8.

Table A.2.2-7 PAD5 FGR Model Calibration Results: Gadolinia Fuel Steady-State FGR Database

Plant/Program	Rod ID	Rod Burnup (MWd/MTU)	Gadolinia Concentration (w/o)	Measured FGR (%)	Predicted FGR (%)

a,b,c

Table A.2.2-8 PAD5 FGR Model Calibration Results: Gadolinia Fuel Transient FGR Database

Plant/Program	Rod ID	Rod Burnup (MWd/MTU)	Gadolinia Concentration (w/o)	Measured FGR (%)	Predicted FGR (%)

a,b,c

A.2.2.2 Fission Gas Release Model Results

The low burnup athermal fission gas release model is described as Equation (4-11) of Section 4.3.2. The constant F_{ath1} has been determined by fitting the equation for the athermal knockout/recoil release to the data in the low burnup athermal fission gas release database for which negligible thermal fission gas release is predicted. There is no high burnup athermal release due to the low burnup of the selected rods. The fit of the athermal fission gas release model to the 24 rods selected by this criterion is shown in Figure A.2.2-1. The remaining rods in the low burnup athermal database were used to validate the model. Figures A.2.2-2 and A.2.2-3 show the predicted versus measured fission gas release and predicted minus measured fission gas release as a function of rod average burnup, respectively, for the low burnup athermal fission gas release database (calibration and validation data sets combined). It is expected that some portion of the release is coming from thermal release for the validation data sets. Figures A.2.2-1 through A.2.2-3 show that PAD5 predicts the FGR for these low burnup rods with athermal dominated release.

a,b,c

[ ]

Figure A.2.2-1 PAD5 Athermal Fission Gas Release Model Predictions vs. Measured Gas Release with Essentially No Thermal Fission Gas Release

a,b,c

Figure A.2.2-2 PAD5 Fission Gas Release Predictions vs. Measured Fission Gas Release for the Low burnup Athermal Fission Gas Release Database

a,b,c

Figure A.2.2-3 PAD5 Fission Gas Release Predicted Minus Measured Results vs. Rod Average Burnup for the Low Burnup Athermal Fission Gas Release Database

The high burnup athermal FGR model is described as Equations (4-12a) and (4-12b) in Section 4.3.2. The model has been calibrated based on a subset of the available data base and validated by comparisons with the remaining database. About half of the database was selected for the calibration. The selection of calibration data was random with the constraint that the fuel rods from any assembly should not be heavily over represented in either the calibration or validation subsets. Although the athermal (both low and high burnup release) are the dominate mechanism for these rods, there may still be a fair amount of thermal FGR in these rods. The coefficients (Bu_{enh}, 1/a, and b) in the high burnup athermal FGR model along with the thermal FGR model, which are discussed next, have been determined to give a best estimate fit to the data in the high burnup athermal FGR database. The model constants are adjusted until the average predicted minus measured FGR is approximately 0. Figures A.2.2-4 and A.2.2-5 show the predicted versus measured fission gas release and predicted minus measured fission gas release as a function of rod average burnup for the high burnup athermal fission gas release database.

a,b,c

Figure A.2.2-4 PAD5 Fission Gas Release Predictions vs. Measured Fission Gas Release for the High Burnup Athermal Fission Gas Release Database

a,b,c

Figure A.2.2-5 PAD5 Fission Gas Release Predicted Minus Measured Results vs. Rod Average Burnup for the High Burnup Athermal Fission Gas Release Database

The thermal FGR model is described with Equations (4-7a), (4-7b), and (4-7c) in Section 4.3.1. Similar to the high burnup athermal model, the thermal model has been calibrated based on a subset of the available thermal database and validated by comparisons with the remaining database. About half of the database was selected for the calibration. The selection of calibration data was random with the constraint that the fuel rods from any assembly should not be heavily over represented in either the calibration or validation subsets. The thermal release is the dominate release mechanism for these data. The model parameters (B0, T0, BL ,TL, BM, TM, BH, TH1, BSL0, TSL0, BSLL, TSLL, BSLM, TSLM, BSLH, TSLH, BSLH1, TSLH1), which determine the release threshold $B_{INC}(T)$ and $B_{REP}(T)$ (Equation (4-6) in Section 4.3.1) are adjusted to give a best estimate fit to the data in the FGR databases. The model constants are adjusted until the average predicted minus measured FGR is approximately 0. Figures A.2.2-6 and A.2.2-7 show the predicted versus measured fission gas release and predicted minus measured fission gas release as a function of rod average burnup for the thermal fission gas release database.

a,b,c

Figure A.2.2-6 PAD5 Fission Gas Release Predictions vs. Measured Fission Gas Release for the Thermal Fission Gas Release Database

a,b,c

Figure A.2.2-7 PAD5 Fission Gas Release Predicted Minus Measured Results vs. Rod Average Burnup for the Thermal Fission Gas Release Database

The transient fission gas release model is described as Equations (4-8), (4-9a), and (4-9b) in Section 4.3.1. With the calibrated steady-state thermal FGR model, the transient FGR model is calibrated by adjusting the effective grain size parameter XDIFF that results in a best estimate fit, again determined by obtaining an average predicted minus measured fission gas release approaching zero. Figures A.2.2-8 and A.2.2-9 show the predicted versus measured fission gas release and the predicted minus measured fission gas release as a function of rod average burnup for the transient fission gas release database.

a,b,c

Figure A.2.2-8 PAD5 Fission Gas Release Predictions vs. Measured Fission Gas Release for the Transient Fission Gas Release Database

a,b,c

Figure A.2.2-9 PAD5 Fission Gas Release Predicted Minus Measured Results vs. Rod Average Burnup for the Transient Fission Gas Release Database

[ ]^{a,c}

The gadolinia fuel thermal fission gas release multiplication factor is determined to give an average predicted minus measured fission gas release of approximately zero for the gadolinia fuel with measured fission gas releases greater than 3%, since these are the gadolinia fuel data which are expected to have a significant sensitivity to the thermal fission gas release model. Figures A.2.2-10 through A.2.2-12 show the predicted versus measured fission gas release, predicted minus measured fission gas release as a function of rod average burnup for the gadolinia fission gas release database, and predicted minus measured fission gas release as a function of gadolinia concentration, respectively. There is no trend observed as a function of burnup or gadolinia concentration.

a,b,c

Figure A.2.2-10 PAD5 Fission Gas Release Predictions vs. Measured Fission Gas Release for the Gadolinia Fuel Fission Gas Release Database

a,b,c

Figure A.2.2-11 PAD5 Fission Gas Predicted Minus Measured Results vs. Rod Average Burnup for the Gadolinia Fuel Fission Gas Release Database

a,b,c

Figure A.2.2-12 PAD5 Fission Gas Predicted Minus Measured Results vs. Gadolinia Concentration for the Gadolinia Fuel Fission Gas Release Database

Tables A.2.2-3 through A.2.2-8 in Section A.2.2.1 give a complete listing of the fission gas release data and the PAD5 fission gas release predictions for all the rods in the fission gas release database. Statistics for the PAD5 FGR calibration results are given in Table A.2.2-9.

Table A.2.2-9 PAD5 FGR Model Results Statistics

Thermal Fission Gas Release Database			
	Calibration Database	**Validation Database**	**Entire Database**
Number of rods			
P – M average (%)			
P – M σ (%)			
High Burnup Athermal (Greater than 45 GWd/MTU) Fission Gas Release Database			
	Calibration Database	**Validation Database**	**Entire Database**
Number of rods			
P – M average (%)			
P – M σ (%)			

a,b,c

a,b,c

Table A.2.2-9 PAD5 FGR Model Results Statistics (cont.)

Low Burnup Athermal (Less than 45 GWd/MTU) Fission Gas Release Database				
	Calibration Database	**Validation Database**	**Entire Database**	a,b,c
Number of rods	[			]
P – M average (%)				
P – M σ (%)				

Complete Athermal Fission Gas Release Database				
	Calibration Database	**Validation Database**	**Entire Database**	a,b,c
Number of rods	[			]
P – M average (%)				
P – M σ (%)				

Transient Fission Gas Release Database					
	Calibration Database	**Validation Database**	**Entire Database Measured FGR ≥ 3%**	**Entire Database**	a,b,c
Number of rods	[				]
P – M average (%)					
P – M σ (%)					

Gadolinia Fission Gas Release Database, Measured FGR > 3%				
	Steady State FGR Data	**Transient FGR Data**	**Entire Database**	a,b,c
Number of rods	[			]
P – M average (%)				
P – M σ (%)				

A.2.2.3 Fission Gas Release Model Uncertainties

In PAD5, [

]^{a,c}. The athermal FGR model uncertainty is given by [

]^{a,c}. The thermal FGR model uncertainty is derived by [

]^{a,c}. For transient FGR, [

]^{a,c}. The UB/LB FGR results are obtained by using [

]^{a,c}.

For example for the UB FGR results, the EOL FGR for each rod is calculated with PAD5 for [

]^{a,c}

The UB SRSS value is calculated with the expression:

$$\left[\qquad\qquad\right]^{a,c} \tag{A.2-5}$$

The final FGR model uncertainties and BE model parameters are summarized in Table A.2.2-10. Figures A.2.2-13 through A.2.2-19 compare the bounding models with the measured fission gas release data. The UB FGR model [ ]^{a,c} of the UO_2 fuel thermal FGR data, [ ]^{a,c} of the UO_2 fuel athermal FGR data, [ ]^{a,c} of the transient UO_2 fuel FGR data, and [ ]^{a,c} of the total steady-state and transient UO_2 fuel thermal FGR data. The LB FGR model bounds [ ]^{a,c} of the UO_2 fuel thermal FGR data, [ ]^{a,c} of the UO_2 fuel athermal FGR data, and [ ]^{a,c} of the total steady-state and transient UO_2 fuel thermal FGR data. The model uncertainties are appropriate for gadolinia fuel without further modification.

Table A.2.2-10 PAD5 Fission Gas Release Model Uncertainties			
Model Coefficient	**BE**	**UB**	**LB**
Athermal Fission Gas Release Model Uncertainties			a,c
Thermal Fission Gas Release Model Uncertainties			a,c

Note:
1. Note that the [
]^{a,c}

a,b,c

Figure A.2.2-13 Upper Bound UO_2 Steady-State Fission Gas Release Model, Thermal Release Dominated

a,b,c

Figure A.2.2-14 Upper Bound UO_2 Steady-State Fission Gas Release Model, Athermal Release Dominated

a,b,c

Figure A.2.2-15 Lower Bound UO_2 Steady-State Fission Gas Release Model, Thermal Release Dominated

a,b,c

Figure A.2.2-16 Lower Bound UO_2 Steady-State Fission Gas Release Model, Athermal Release Dominated

a,b,c

Figure A.2.2-17 Upper Bound UO_2 Transient Fission Gas Release Model

a,b,c

Figure A.2.2-18 Upper Bound Gadolinia Fission Gas Release Model

a,b,c

Figure A.2.2-19 Lower Bound Gadolinia Fission Gas Release Model

A.2.3 Cladding Creep

A.2.3.1 Cladding Creep Database

Table A.2.3-1 provides a summary of the creep database used to calibrate and validate the PAD5 cladding creep model and to quantify the model uncertainties. Table A.2.3-1 includes a brief description of the test characteristics for each set of data. Except for the [
]^{a,c}, all of the ZIRLO and **Optimized ZIRLO** in-reactor data is [
]^{a,c}, while the Zircaloy-4 in-reactor data is [
]^{a,c}. These rods have not experienced significant pellet-clad contact, hence the measured diametral profilometry reflects the evolution of the permanent deformation of the clad geometry. The Plant R samples also do not experience any pellet-clad contact, by the design of the samples.

Table A.2.3-1 Summary PAD5 Cladding Creep Database

Campaign	Material	Comments

a,b,c

For comparison purposes, the measured in-reactor profilometry data has been [ ]^{a,c}, and [ ]^{a,c} of the rod have been considered. [ ]^{a,c}

A.2.3.2 Cladding Creep Model Calibration

The ZIRLO and **Optimized ZIRLO** cladding creep database has been separated into two roughly equal subsets, namely the Calibration (C) and Validation (V) datasets. The separation process was achieved by first sorting the list of unique rod names and then selecting every other rod (this ensures a roughly 50%/50% selection from each campaign over all campaigns). The Zircaloy-4 database was similarly separated. Table A.2.3-2 summarizes the separation of the database into C and V data sets.

Table A.2.3-2 PAD5 Clad Creep Calibration and Validation Database

Plant/Program	Rod ID	Rod Average Burnup (MWd/MTU)[1]	Cladding	Calibration (C)/Validation (V)

a,b,c

Table A.2.3-2 PAD5 Clad Creep Calibration and Validation Database (cont.)

Plant/Program	Rod ID	Rod Average Burnup (MWd/MTU)[1]	Cladding	Calibration (C)/Validation (V)

a,b,c

Table A.2.3-2 PAD5 Clad Creep Calibration and Validation Database (cont.)

Plant/Program	Rod ID	Rod Average Burnup (MWd/MTU)[1]	Cladding	Calibration (C)/Validation (V)

a,b,c

Table A.2.3-2 PAD5 Clad Creep Calibration and Validation Database (cont.)

Plant/Program	Rod ID	Rod Average Burnup (MWd/MTU)[1]	Cladding	Calibration (C)/Validation (V)

a,b,c

Table A.2.3-2 PAD5 Clad Creep Calibration and Validation Database (cont.)

Plant/Program	Rod ID	Rod Average Burnup (MWd/MTU)[1]	Cladding	Calibration (C)/Validation (V)

a,b,c

Table A.2.3-2 PAD5 Clad Creep Calibration and Validation Database (cont.)

Plant/Program	Rod ID	Rod Average Burnup (MWd/MTU)[1]	Cladding	Calibration (C)/Validation (V)
[				] a,b,c

PAD5 clad creep model is discussed in Section 5.4. For ZIRLO and **Optimized ZIRLO** cladding, the calibration of the irradiation creep model (Equation (5-26) in Section 5.4) is [ ]^{a,c} and the calibration of the thermal creep model (Equation (5-22) in Section 5.4) is [ ]^{a,c}

The final calibration was [

]^{a,c}

The validation dataset was used to confirm that the predictions remain for a fully independent set of data. Table A.2.3-3 (for ZIRLO and **Optimized ZIRLO** cladding) and Table A.2.3-4 (for Zircaloy-4) show that the combined calibration and validation datasets (All) have very similar best estimate creep statistics.

Table A.2.3-3 ZIRLO/*Optimized ZIRLO* Best Estimate Cladding Creep Statistics

Dataset	Sample Size	Average of Predicted Minus Measured Diameter (mils)	Standard Deviation of Predicted Minus Measured Diameter (mils)
All	[		
Calibration			
Validation	]		

a,b,c

Table A.2.3-4 Zircaloy-4 Best Estimate Cladding Creep Statistics				a,b,c
Dataset	**Sample Size**	**Average of Predicted Minus Measured Diameter (mils)**	**Standard Deviation of Predicted Minus Measured Diameter (mils)**	
All	[			]
Calibration				
Validation	]			

The PAD5 prediction versus measured results for the ZIRLO and **Optimized ZIRLO** in-reactor creep and for the Plant R creep data are shown in Figures A.2.3-1 and A.2.3-2, respectively. "In-reactor" in the following figures refers to commercial fuel rods. To assess trends in the ZIRLO and **Optimized ZIRLO**, in-reactor creep predictions the residual (prediction minus measured cladding diameter) versus some key model input parameters (burnup and clad temperature (elevation)) are shown in Figures A.2.3-3 and A.2.3-4. Over the [ ]^{a,c} of the rod the PAD5 model residual does not have any significant trends with burnup or elevation. The PAD5 BE model has acceptable stress, temperature (as shown in the elevation plots), and fast fluence (and flux) dependence over the whole range of conditions that are typical of one cycle fuel rod exposure.

a,b,c

Figure A.2.3-1 ZIRLO and *Optimized ZIRLO* Cladding In-reactor Creepdown

a,b,c

Figure A.2.3-2 ZIRLO Cladding Creep From Plant R Creep and Growth Program

a,b,c

Figure A.2.3-3 ZIRLO and *Optimized ZIRLO* Cladding In-reactor Residual (M – P) vs. Nodal Burnup

a,b,c

Figure A.2.3-4 ZIRLO Cladding In-reactor Residual (P – M) vs. Normalized Elevation

For all practical purposes, [

]^{a,c} Figures A.2.3-5 and A.2.3-6 show the creep results by ZIRLO and **Optimized ZIRLO** data sets.

a,b,c

Figure A.2.3-5 ZIRLO and *Optimized ZIRLO* Cladding In-reactor Creepdown

a,b,c

Figure A.2.3-6 ZIRLO and *Optimized ZIRLO* Cladding In-reactor Residual (P – M) vs. Nodal Burnup

As discussed in Section 5.4, there is [

]^{a,c} For Zircaloy-4, [

]^{a,c} were used in the best estimate calibration. Figures A.2.3-7 through A.2.3-9 show the Zircaloy-4 best estimate results. To assess trends in the Zircaloy-4 creep predictions, the residual (predicted minus measured clad diameter) versus some key model input parameters (burnup and clad temperature (elevation)) are shown in Figures A.2.3-8 and A.2.3-9.

a,b,c

Figure A.2.3-7 Zircaloy-4 In-reactor Predicted vs. Measured Creepdown

a,b,c

Figure A.2.3-8 Zircaloy-4 In-reactor Creepdown Residual (P – M) vs. Nodal Burnup

a,b,c

Figure A.2.3-9 Zircaloy-4 In-reactor Creepdown Residual (P – M) vs. Normalized Elevation

The online measurement data from the Halden tests (Reference A.18 and A.19) are also used to confirm the capability of the model to predict the history of cladding creep under irradiation. Figures A.2.3-10 through A.2.3-12 show the PAD5 predictions of creep strain as a function of time for the Halden ZIRLO tests. The conditions of the Halden ZIRLO creep test are listed in Table A.2.3-5. These Halden tests were performed at [ ]^{a,c} hence it is valuable to quantify the steady state creep rate under these conditions, representing the top end of the rod. These tests, due to the higher temperature, have [ ]^{a,c}. It should be noted that the Halden ZIRLO creep test [ ]^{a,c}.

Table A.2.3-5 Halden ZIRLO Creep Test Conditions

Test	Hoop Stress [MPa]	Fast Flux [10^13 n/cm^2-s E>1 MeV]	Temperature [°F]
IFA 663-1			
IFA 663-2			
IFA 663-3			
IFA 617			

a,b,c

a,b,c

Figure A.2.3-10 Halden ZIRLO Cladding Creep Tests IFA663-1 and IFA663-2

a,b,c

Figure A.2.3-11 Halden ZIRLO Cladding Creep Test IFA663-3

a,b,c

Figure A.2.3-12 Halden ZIRLO Cladding Creep Test IFA617

The online measurement data from the [ ]^{a,c} are used to confirm the capability of the model to predict the history of creep strain. Figure A.2.3-13 shows the PAD5 predictions of creep strain as a function of time for the [ ]^{a,c}. This test was performed at high temperature (662 °F) and high fast flux (16.9×10^{13} n/cm^2/s), hence it is valuable to quantify the steady state creep rate under these prototypic limiting conditions.

a,b,c

Figure A.2.3-13 The CEA Zircaloy-4 Creep Test

A.2.3.3 Cladding Creep Model Uncertainty

To quantify the uncertainty in the PAD5 creep model, [ ]^{a,c}, is applied to the creep model, which is equal to unity in the best estimate (BE) case. The Upper Bound (UB) and Lower Bound (LB) [ ]^{a,c} are determined from [ ]^{a,c} as used in the BE calculations in Section A.2.3.2. The LB and UB ACREEP values for PAD5 are listed in Table A.2.3-6. All alloys (Zircaloy-4, ZIRLO, and **Optimized ZIRLO**) have the same functional form. Further, for convenience, the PAD5 creep model also considers that [ ]^{a,c}.

The Zircaloy-4, ZIRLO and **Optimized ZIRLO** UB and LB values are determined by [ ]^{a,c}. Figures A.2.3-14 and A.2.3-15 show the ZIRLO and **Optimized ZIRLO** UB and LB predictions, respectively. Figures A.2.3-16 and A.2.3-17 show the Zircaloy-4 UB and LB predictions respectively.

Table A.2.3-6 Bounding PAD5 Creep Model Alloy Specific Material ACREEP

Cladding Material	LB ACREEP	UB ACREEP
Zircaloy-4		
ZIRLO and **Optimized ZIRLO**		

a,b,c

a,b,c

Figure A.2.3-14 ZIRLO and *Optimized ZIRLO* Cladding Upper Bound Predictions

a,b,c

Figure A.2.3-15 ZIRLO and *Optimized ZIRLO* Cladding Lower Bound Predictions

a,b,c

Figure A.2.3-16 Zircaloy-4 Upper Bound Predictions

a,b,c

Figure A.2.3-17 Zircaloy-4 Lower Bound Predictions

A.2.4 Cladding Diameter Change from Ramp Tests

A.2.4.1 Ramp Diameter Change Database

Table A.2.4-1 summarizes the available ramp cladding diameter change measurements by data set. In reviewing and modeling these data, PAD5 models did not accurately model certain datasets due to either atypical fuel design or defective measurements. The data summarized in Table A.2.4-2 will be excluded from calibration and validation.

Table A.2.4-1 Cladding Diameter Change Measurements by Data Set		
Validation Data Set	**Number of Rods**	**References**

a,b,c

Table A.2.4-2 Cladding Diameter Change Data Sets Excluded from Calibration and Validation		
Test Program/Rods	**Atypical Fuel Features**	**Reason for Exclusion**

a,b,c

The data used for calibrating fission gas swelling during long ramps are listed in Table A.2.4-3.
[

]^{a,c} This data set covers a wide range of burnup levels. For calibration and validation purposes these data are further divided into a Calibration (C) set and Validation (V) set as shown in the C/V column in Table A.2.4-3. The selection of rods for the calibration or the validation data set is random in nature, except that the [

]^{a,c} are intentionally kept in the calibration set.

Table A.2.4-3 Long Term Ramp Tests Data Used for Ramp Diameter Change Calibration and Validation

Plant/Program	Rod ID	Burnup (GWd/MTU)	Ramp Terminal LHGR (RTL) (kW/ft)	Holding Time (h)	C/V

a,b,c

The data used for calibrating fission gas swelling during short ramps are listed in Table A.2.4-4. [

]^{a,c}

Table A.2.4-4 Ramp Tests Data Used for Justification of Reduced Fission Gas Swelling for Short Ramps

Program	Rods	Burnup (GWd/MTU)	RTL (KW/ft)	Holding Time

a,b,c

A.2.4.2 Ramp Diameter Change Calibration Results

Many PAD5 models contribute to the ramp strain, including fuel thermal expansion, fuel relocation, fission gas swelling, cladding thermal expansion, cladding plasticity and cladding creep. Therefore, ramp strain is an integral calibration confirmation of the mechanical models of PAD5. [

]^{a,c}

The typical ramp tests have holding times from a few hours to days, which is sufficient time for the fission gas bubbles to develop and cause gaseous swelling. However, [

]^{a,c}

It should be noted there are [

]^{a,c} The PAD5 fission gas swelling model is discussed in Section 5.8.

The coefficients in Equation (5-40) of Section 5.8 are adjusted to best predict the clad diameter change during long ramps. Figures A.2.4-1 and A.2.4-2 show the calibration and validation results for the ramp test rods with long holding time. These results show good agreement between predicted and measured values with no apparent bias in predicted minus measured data versus burnup. There are expected differences in the behavior of gaseous swelling between low burnup and high burnup. At low burnup there is limited grain boundary gas accumulation. At high burnup there may be fission gas already accumulated at the grain boundary during steady state operation from the fission gas release processes and from microstructure changes. PAD5 is able to treat those effects properly.

a,b,c

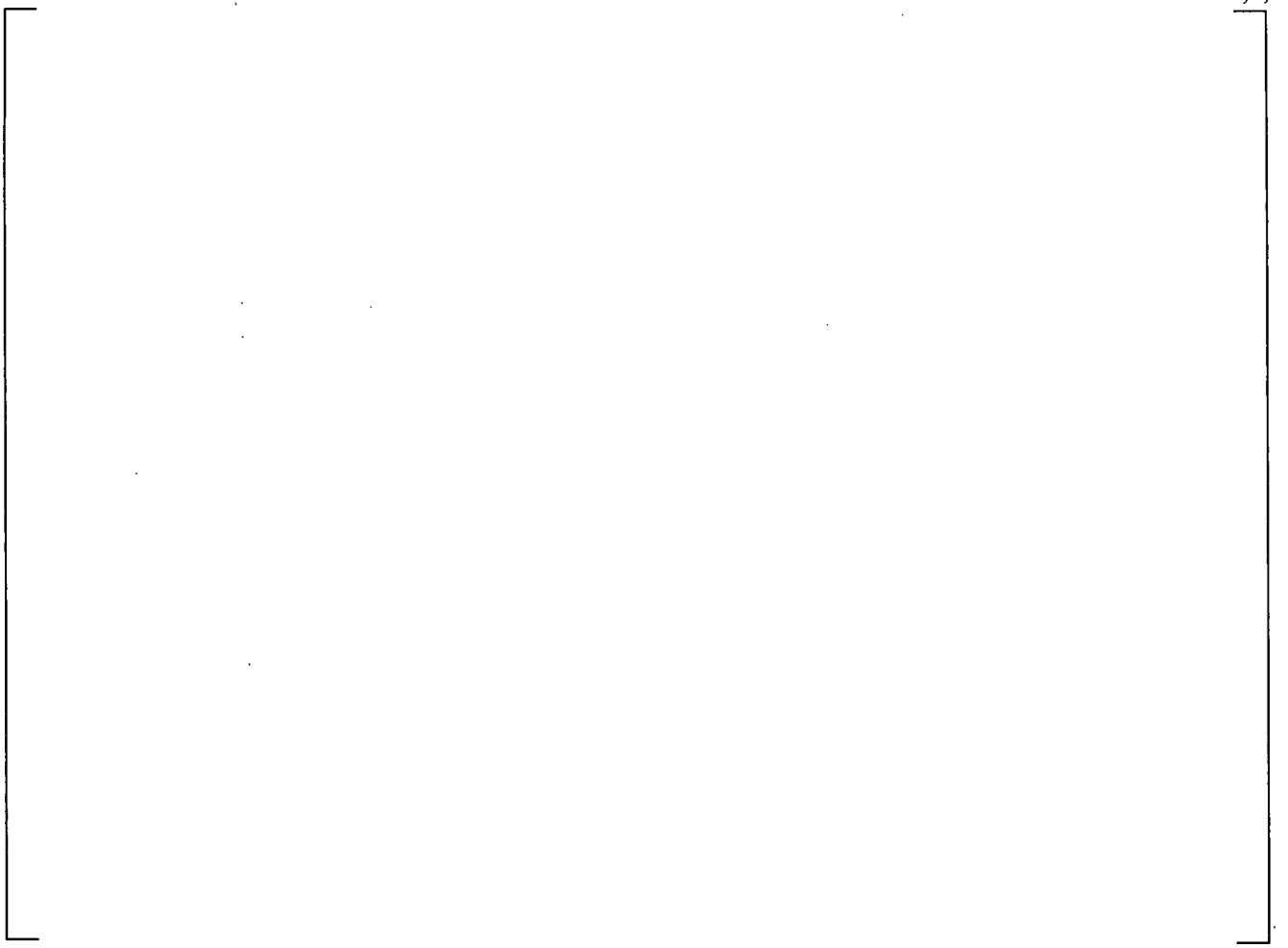

Figure A.2.4-1 PAD5 Predicted vs. Measured Diameter Change – Calibration and Validation Sets for Ramps with Long Hold Times

a,b,c

[

]

Figure A.2.4-2 PAD5 Predicted Minus Measured Diameter Change vs. Nodal Burnup – Calibration and Validatiaon Sets for Ramps with Long Hold Times

The coefficients in Equation (5-41) of Section 5.8 are adjusted to best predict the clad diameter change during short ramps. Figures A.2.4-3 and A.2.4-4 show the results for the rods with short holding times as listed in Table A.2.4-4. [

]a,c

a,b,c

Figure A.2.4-3 Predicted vs. Measured Ramp Cladding Diameter Change for Long and Short Ramps

a,b,c

Figure A.2.4-4 PAD5 Predicted Minus Measured Ramp Cladding Diameter Change for Long and Short Ramps

A.2.4.3 Ramp Diameter Change Model Uncertainties

As discussed in Section A.2.4.2, the PAD5 diameter change predictions are affected by many performance models. The uncertainties in these models contribute to the uncertainty in the permanent cladding deformation results. In addition, uncertainties in key fuel design parameters, particularly gap size, will also affect the permanent cladding deformation results. The Upper Bound (UB) uncertainty is an aggregate of the many model uncertainties that have contributed to the diameter changes during the ramp, i.e., fuel and clad thermal expansion, fuel solid swelling and densification, and cladding creep. [

]^{a,c}

A.2.5 Integral Calibration Confirmation

Following the calibration of the fuel performance parameters and models described in the preceding sections, the integrated code performance can be evaluated further based on the ability of the code to predict certain other fuel rod performance parameters which are a reflection of the whole rod

performance. This integrated code performance assessment shows how well the code predicts end of life or end of cycle fuel rod diameters and end of life cold internal void volumes.

A.2.5.1 Steady-State Cladding Outer Diameter

The cladding diameter change after fuel-cladding gap closure is impacted by the pellet deformation, i.e., thermal expansion, pellet relocation, fuel solid swelling, and fission gas swelling. The data considered for this evaluation has nodal burnups greater than [ ]^{a,c}. Figures A.2.5-1 and A.2.5-2 show the diameter change data and predictions from some multi-cycle high burnup profilometry. For comparison purposes, the measured in-reactor profilometry data has been [ ]^{a,c}. Table A.2.5-1 shows the data used for the steady-state cladding outer diameter evaluation. Figure A.2.5-1 shows the predicted versus measured cladding outer diameter change. Figure A.2.5-2 shows the predicted minus measured cladding outer diameter change versus rod average burnup. There is [

]^{a,c}

Table A.2.5-1 Steady-state Cladding Outer Diameter Database (Nodal Burnup > [ ]^{a,c})

Plants	Rod ID	Rod Average Burnup (MWd/MTU)	Cladding Type

a,b,c

Table A.2.5-1 Steady-state Cladding Outer Diameter Database (Nodal Burnup > [ ] [a,c]) (cont.)

Plants	Rod ID	Rod Average Burnup (MWd/MTU)	Cladding Type

a,b,c

Table A.2.5-1 Steady-state Cladding Outer Diameter Database (Nodal Burnup > [ ] [a,c]) (cont.)

Plants	Rod ID	Rod Average Burnup (MWd/MTU)	Cladding Type

a,b,c

Table A.2.5-1 Steady-state Cladding Outer Diameter Database (Nodal Burnup > [ ] [a,c]) (cont.)

Plants	Rod ID	Rod Average Burnup (MWd/MTU)	Cladding Type

a,b,c

Table A.2.5-1 Steady-state Cladding Outer Diameter Database (Nodal Burnup > [ ]^{a,c}) (cont.)

Plants	Rod ID	Rod Average Burnup (MWd/MTU)	Cladding Type

a,b,c

a,b,c

Figure A.2.5-1 Predicted Versus Measured Steady-State Clad Diameter Change (Burnup > [ ]^{a,c})

a,b,c

Figure A.2.5-2 Predicted Minus Measured Steady-State Clad Diameter Change vs. Nodal Burnup (Burnup > [ ]^{a,c})

A.2.5.2 Void Volume

Void volume data are used primarily to assess the integral performance of cladding creep, fuel relocation, rod growth, fuel densification, and the fuel swelling models. Table A.2.5-2 lists the void volume data used in this integral calibration. Void volumes from the refabricated ramp test rods are excluded. PAD5 results at room temperature (cold) are compared with the measured data in Figures A.2.5-3 and A.2.5-4.
Figure A.2.5-3 shows the predicted versus measured total free volume at room temperature.
Figure A.2.5-4 shows the predicted minus measured total free volume versus rod average burnup. These figures illustrate good agreement between the predicted and measured total free cold void volume.

Table A.2.5-2 PAD5 Cold Void Volume Database

Plant/Program	Rod ID	Fuel Type	Rod Average Burnup (MWd/MTU)	Measured Cold Void Volume (in^3)	Predicted Cold Void Volume (in^3)

a,b,c

Table A.2.5-2 PAD5 Cold Void Volume Database (cont.)

Plant/Program	Rod ID	Fuel Type	Rod Average Burnup (MWd/MTU)	Measured Cold Void Volume (in³)	Predicted Cold Void Volume (in³)

a,b,c

Table A.2.5-2 PAD5 Cold Void Volume Database (cont.)

Plant/Program	Rod ID	Fuel Type	Rod Average Burnup (MWd/MTU)	Measured Cold Void Volume (in³)	Predicted Cold Void Volume (in³)

a,b,c

Table A.2.5-2 PAD5 Cold Void Volume Database (cont.)

Plant/Program	Rod ID	Fuel Type	Rod Average Burnup (MWd/MTU)	Measured Cold Void Volume (in³)	Predicted Cold Void Volume (in³)

a,b,c

Table A.2.5-2 PAD5 Cold Void Volume Database (cont.)

Plant/Program	Rod ID	Fuel Type	Rod Average Burnup (MWd/MTU)	Measured Cold Void Volume (in³)	Predicted Cold Void Volume (in³)

a,b,c

Table A.2.5-2 PAD5 Cold Void Volume Database (cont.)

Plant/Program	Rod ID	Fuel Type	Rod Average Burnup (MWd/MTU)	Measured Cold Void Volume (in^3)	Predicted Cold Void Volume (in^3)

a,b,c

Table A.2.5-2 PAD5 Cold Void Volume Database (cont.)

Plant/Program	Rod ID	Fuel Type	Rod Average Burnup (MWd/MTU)	Measured Cold Void Volume (in³)	Predicted Cold Void Volume (in³)

a,b,c

Table A.2.5-2 PAD5 Cold Void Volume Database (cont.)

Plant/Program	Rod ID	Fuel Type	Rod Average Burnup (MWd/MTU)	Measured Cold Void Volume (in³)	Predicted Cold Void Volume (in³)
[					]a,b,c

[

]a,b,c

Figure A.2.5-3 Predicted vs. Measured Cold Void Volume

a,b,c

Figure A.2.5-4 Predicted Minus Measured Cold Void Volume vs. Rod Average Burnup

A.3 CONCLUSIONS

PAD5 calibration and validation is based on a significantly expanded database, particularly data for fuel rods with burnup higher than [ ]^{a,c} As shown by the calibrations presented in this appendix, PAD5 predicts the fuel temperature, fission gas release, ramp cladding diameter change, steady state cladding diameter, and cold internal void volume data well at high rod average burnups up to and above [ ]^{a,c}, and exhibits no significant error trend over the range of operation (i.e. burnup , power, and temperatures). The PAD5 results presented in this Appendix, along with the results for individual models presented in Sections 3 through 6, in particular clad corrosion and rod growth, demonstrate that PAD5 models are qualified to model ZIRLO (and legacy Zircaloy-4) fuel rods with lead rod average burnup up to 62 GWd/MTU and **Optimized ZIRLO** clad fuel rods with lead rod average burnup up to [ ]^{a,c}

A.4 APPENDIX A REFERENCES

A.1 NUREG/CR-0332 (BNWL-1988), R3, "Test Design, Precharacterization, and Fuel Assembly Fabrication for Instrumented Fuel Assemblies IFA-431 and IFA-432," November 1977.

A.2 PNL-2494 (NRC-1&3), "Data Report for the NRC/PNL Halden Assembly IFA-431," April 1978.

A.3 NUREG/CR-0560 (PNL-2673), R-3, "Data Report for the NRC/PNL Halden Assembly IFA-432," August 1978.

A.4 NUREG/CR-1950 (PNL-3709), R3 , "Data Report for the NRC/PNL Halden Assembly IFA-432: April 1978-May 1980," April 1981.

A.5 HPR-273, "Fuel Behaviour Inferred from Internal Gas Flow and Temperature Measurements Made at the Beginning-of-Life of IFA-504," May 1981.

A.6 HWR-332, "Thermal Behaviour and Fission Product Release in the Gas-Flow Rig IFA-504 up to 50 MWd/kg UO_2," January 1993.

A.7 HPR-235, "Status Report of the 3-Rod Diameter Rig IFA-509 (NUCLITAL-HP)," May 1980.

A.8 HWR-671, "Study of thermal behavior of UO_2 and $(U,Gd)O_2$ to high burnup (IFA-515)," February 2001.

A.9 HWR-531, "Steady State and Transient Temperature Measurements on BWR-Type Fuel up to 70 MWd/kgUO_2. (IFA-533.2)," January 1998.

A.10 HWR-245, "Final Report on the In-Pile Results from the Pellet Roughness Test in Rig IFA-562," November 1989.

A.11 HWR-341, "Thermal Conductivity Degradation Analysis of the Ultra High Burnup Experiment (IFA-562)," February 1993.

A.12 HWR-442, "The integral fuel rod behaviour test IFA-597.2: Pre-characterization and analysis of the measurements," March 1996.

A.13 HWR-817, "Final Report on the UO_2-$Gd_2 O_3$ Fuel Performance Test in IFA-636," September 2005.

A.14 HWR-1007, "Progress Report on the Irradiation of VVER Large Grain and Gd-Doped Fuel in IFA-676.1," September 2011.

A.15 HWR-922, "Comparative Integral Irradiation Test on Gadolinium Fuel (IFA-681); Update After Ten Cycles of Irradiation," March 2010.

A.16 HBC 89/10, "HBC Task 3 Power-To-Melt Experiment," April 1989.

A.17 HBC 94/47, "HBC Task 3 HBC-5 Power-To-Melt Experiment," November 1994.

A.18 HWR-658, "In Reactor Creep of Zircaloy Fuel Caldding: Results from IFA-617 and Plans for Future Testing," January 2001.

A.19 M. A. McGrath, "Summary of Results from the Cladding Creep Test IFA-663," OECD Halden Reactor Project, Enlarged Halden Programme Group Meeting, HPR-364, Vol. 1, Paper 1.7, 16-21 October 2005.

A.20 A. Soniak, et al, "Irradiation Creep Behavior of Zr-Base Alloys," Zirconium in the Nuclear Industry: Thirteenth International Symposium, ASTM STP 1423, G.D. Moan and P. Rudling, Eds., ASTM International, West Conshohocken, PA, 2002, pp. 837-862.

A.21 LTR-NRC-13-6, "SER Compliance of WCAP-12610-P-A & CENPD-404-P-A Addendum 1-A "Optimized ZIRLO™" (Proprietary/Non-Proprietary)," February 25, 2013.

A.22 E. Kolstad, "The 3-Rod Diameter Rig Experiments IFA-404[I] (HP) and IFA-404[II] (HP)," HPR-0190, Session 5, Paper 29.

A.23 P. Knudsen, et al, "Final Report on the RISO Transient Fission Gas Release Project," RISO-TFGP-R29, May 1986.

A.24 RISO-FGP3-FINAL, Pt. 1, "The Third Riso Fission Gas Project, Final Report: The Project," March 1991

A.25 STIR-53, "Final Report of Inter-Ramp Project," August 1979.

A.26 M. Grounes, "Final Report of the TRANS-RAMP II Project," STUDSVIK-STTRII-14, March, 1987.

A.27 S. Djurle, "The Studsvik Over-Ramp Project," NP-3007, Research Project 1026-1, Final Report, April 1983

A.28 S. Djurle, "Final Report of The Supper-Ramp Project," STUDSVIK-STSR-32, December 1984.

A.29 R. Kallstrom, "SCIP, Task 0; Ramp Test Results," Final Report, SUDSVIK/N-05/154, STUDSVIK-SCIP-42, 2005.

A.30 P. Blanpain, and L. Mertens, "Gain Final Report," GN 89/48, March 1991.

A.31 R. Sairanen, et al, "Analysis of IFA-505 Fission Gas Release Data and Comparison with Release Models," HPR-317, May 1984.

A.32 J. O. Barner, et al, "High Burnup Effects Program – Final Report," HBEP-61, April 1990.

A.33 P. Knudsen, et al, "Final Report on the RISO Fission Gas Project," RISO-FGP-R17rev, June 1983.

A.34 WCAP-15063-P-A Revision 1, with Errata, (Proprietary) and WCAP-15064-NP-A Revision 1, with Errata, (Non-Proprietary), "Westinghouse Improved Performance Analysis and Design Model (PAD 4.0)," July 2000.

A.35 P. Blanpain, et al, "Properties of UO_2 Irradiated to High Burnups," EPRI NP-5191-LD, Project X101-5, Final Report, April 1987.

APPENDIX B
SAMPLE CALCULATION

B.1 INTRODUCTION

Appendix B provides sample PAD5 results for six fuel rods selected from three fuel assembly designs, as summarized in Table B.1-1. A standard UO_2 fuel rod and an Integral Fuel Burnable Absorber (IFBA) fuel rod were modeled from each assembly type. The 15X15 fuel rods represent the largest cladding outer diameter (0.422" OD) Westinghouse fuel design, and the 17X17 fuel rods represent the smallest cladding outer diameter (0.360" OD) Westinghouse fuel design. The 15X15 and 17X17 IFBA fuel designs use ZrB_2 coated UO_2 IFBA. The CE 16X16 IFBA fuel rod (0.382" OD) uses Gd_2O_3-UO_2 IFBA. All of these rods use **Optimized ZIRLO** cladding material.

Current Westinghouse fuel operation is limited to lead rod average burnup up to 62 GWd/MTU (CE NSSS limited to 60 GWd/MTU), and these reference case results are intended to illustrate expected fuel behavior consistent with three-cycles of operation to an extended lead rod average burnup up to [ ]^{a,c}. The power histories for these reference rods were developed based on current fuel rod designs but with adjustments to rod power and cycle lengths to produce the desired increase in rod burnup. Axial power shapes, defined by axial node, represent realistic plant operation, but the shape assignments to specific steps were simplified to reduce the total number of axial shapes to less than 20 (consistent with FRAPCON 3.4 input limitations, Reference B.1). The resulting shape assignments produced more limiting end of cycle local power changes in the 17X17 case results. Additional details on the reference case designs are provided in Section B.2.

PAD5 models the rod power history as a series of discrete time steps, with the rod average power and axial power shape held constant during the time step. For example, if the first and second time steps are (in hours) 0.01 and 150.0, respectively, the first power level and axial shape are applied for the time interval from 0.0 to 0.01 hours, and the second power level and axial shape are applied for the time interval from 0.01 to 150.0 hours. This is indicated in the figures that illustrate the reference rod power histories in Section B.2 as a step function.

Typical PAD5 output summarizes the predicted results at the end of each time step. The reference case predicted performance parameters are plotted as a function of burnup as line segments connecting these end of step results.

Table B.1-1 PAD5 Reference Designs					
Reference Case	Fuel Assembly Type	Rod Type	Rod Average Burnup (MWd/MTU)	Cladding Outer Diameter (inches)	a,c
1					
2					
3					
4					
5					
6					

B.2 KEY FUEL ROD PERFORMANCE PARAMETERS

This section provides additional fuel rod design data and selected PAD5 results for each of the six reference fuel rods described in Table B.1-1. Subsections B.2.1, B.2.2, and B.2.3 summarize the 15X15, 17X17, and CE 16X16 fuel rod designs and best estimate PAD5 predictions.

The following additional fuel rod design information is provided for each reference design:

- Detailed fuel rod design parameters, including fabrication tolerances
- Time-dependent rod average power history
- Time-dependent axial power shapes
- Core operating conditions
- Rod average fast fluence

For each fuel rod, the following PAD5 results are provided on a best-estimate basis:

- Hot void volume versus rod average burnup
- Rod internal pressure versus rod average burnup
- Fission gas release versus rod average burnup
- Pellet-clad gap versus local burnup at axial node 15
- Gap conductance versus local burnup at axial node 15
- Fuel surface temperature versus local burnup at axial node 15
- Fuel average temperature versus local burnup at axial node 15
- Fuel centerline temperature versus local burnup at axial node 15
- Pellet diameter versus local burnup at axial node 15
- Clad OD versus local burnup at axial node 15

B.2.1 15X15 (0.422" OD) Reference Cases

The following tables and figures summarize the fuel rod design input parameters for 15X15 (0.422" OD) reference fuel rods.

- Table B.2.1-1: 15X15 Reference Case Fuel Rod Parameters
- Table B.2.1-2: 15X15 Reference Case Axial Power Shapes
- Table B.2.1-3: 15X15 Reference Case Rod Power History
- Table B.2.1-4: 15X15 Reference Case Core Operating Conditions
- Figure B.2.1-1: 15X15 Reference Case Rod Average Fast Fluence
- Figure B.2.1-2: 15X15 Reference Case Rod Power History

The following figures illustrate the PAD5 predictions for selected fuel rod parameters. The IFBA fuel rod and the UO_2 fuel rod predictions are provided in the same figures for comparison.

- Figure B.2.1-3: 15X15 Hot Void Volume Versus Rod Average Burnup
- Figure B.2.1-4: 15X15 Rod Internal Pressure Versus Rod Average Burnup
- Figure B.2.1-5: 15X15 Fission Gas Release Versus Rod Average Burnup
- Figure B.2.1-6: 15X15 Pellet-Clad Gap Versus Local Burnup (Axial Node 15)
- Figure B.2.1-7: 15X15 Gap Conductance Versus Local Burnup (Axial Node 15)
- Figure B.2.1-8: 15X15 Fuel Surface Temperature Versus Local Burnup (Axial Node 15)
- Figure B.2.1-9: 15X15 Fuel Average Temperature Versus Local Burnup (Axial Node 15)
- Figure B.2.1-10: 15X15 Fuel Centerline Temperature Versus Local Burnup (Axial Node 15)
- Figure B.2.1-11: 15X15 Pellet Diameter Versus Local Burnup (Axial Node 15)
- Figure B.2.1-12: 15X15 Clad OD Versus Local Burnup (Axial Node 15)

Table B.2.1-1 15X15 Reference Case Fuel Rod Parameters

Description	Input	Upper Bound Uncertainty	Lower Bound Uncertainty	Uncertainty Distribution
Clad Material				
Fuel Stack Length (ft)				
Plenum Length (in)				
Pellet Diameter (in)				
Clad Inner Diameter (in)				
Clad Outer Diameter (in)				
Pellet Length (in)				
Chamfer Depth (in)				
Chamfer Width (in)				
Pellet Dish Spherical Radius (in)				
Pellet Dish Depth (in)				
Pellet Sintering Temperature (°F)				

a,c

Table B.2.1-1 15X15 Reference Case Fuel Rod Parameters (cont.)

Description	Input	Upper Bound Uncertainty	Lower Bound Uncertainty	Uncertainty Distribution
Axial Blanket Design				
Axial Blanket Length (in)				
Annulus Inner Diameter (in)				
Annulus Volume (in^3)(1)				
Plenum with Annulus Volume (in)(2)				
Initial Cold Void Volume (in^3)				
Plenum Spring Diameter (in)				
Plenum Spring Wire Diameter (in)				
Plenum Spring Turns				
Pellet True Density (% Theoretical Density)				
Fuel U-235 Enrichment (w/o)				
Helium Backfill Pressure (psig)				
Rod Pitch (in)				
ZrB_2 IFBA Coating Length (in)				
ZrB_2 IFBA B10 Loading (mg/in)				
ZrB_2 IFBA Coating Thickness (mils)				
Gadolinia Enrichment (w/o)				

a,c

Notes:
1. [ ]a,c
2. [ ]a,c

Table B.2.1-2 15X15 Reference Case Axial Power Shapes

Axial Segment	Power Shape						
	1	2	3	4	5	6	a,c
1							
2							
3							
4							
5							
6							
7							
8							
9							
10							
11							
12							
13							
14							
15							
16							
17							
18							

Axial Segment	Power Shape					
	7	8	9	10	11	a,c
1						
2						
3						
4						
5						
6						
7						
8						
9						
10						

Table B.2.1-2 15X15 Reference Case Axial Power Shapes (cont.)

Axial Segment	Power Shape				
	7	8	9	10	11
11					
12					
13					
14					
15					
16					
17					
18					

a,c

Table B.2.1-3 15X15 Reference Case Rod Power History

Time Step	Time (Hours)	Rod Average Burnup (MWd/MTU)	Rod Average Power (kW/ft)	Axial Power Shape
1				
2				
3				
4				
5				
6				
7				
8				
9				
10				
11				
12				
13				
14				
15				
16				
17				

a,c

Table B.2.1-3 15X15 Reference Case Rod Power History (cont.)

Time Step	Time (Hours)	Rod Average Burnup (MWd/MTU)	Rod Average Power (kW/ft)	Axial Power Shape
18				
19				
20				
21				
22				
23				
24				
25				
26				
27				
28				
29				
30				
31				

a,c

Table B.2.1-4 15X15 Reference Case Core Operating Conditions

Core Operating Condition	Value
Core Average Linear Power (kW/ft)	
Primary Coolant System Pressure (psi)	
Core Mass Flow Rate (1E+6 lbm/hr-ft^2)	
Core Inlet Temperature (°F)	

a,c

a,c

Figure B.2.1-1 15X15 Reference Case Rod Average Fast Fluence

a,c

Figure B.2.1-2 15X15 Reference Case Rod Power History

a,c

Figure B.2.1-3 15X15 Hot Void Volume Versus Rod Average Burnup

a,c

Figure B.2.1-4 15X15 Rod Internal Pressure Versus Rod Average Burnup

a,c

Figure B.2.1-5 15X15 Fission Gas Release Versus Rod Average Burnup

a,c

Figure B.2.1-6 15X15 Pellet-Clad Gap Versus Local Burnup (Axial Node 15)[1]

1. [

]a,c

a,c

Figure B.2.1-7 15X15 Gap Conductance Versus Local Burnup (Axial Node 15)

a,c

Figure B.2.1-8 15X15 Fuel Surface Temperature Versus Local Burnup (Axial Node 15)

a,c

Figure B.2.1-9 15X15 Fuel Average Temperature Versus Local Burnup (Axial Node 15)

a,c

Figure B.2.1-10 15X15 Fuel Centerline Temperature Versus Local Burnup (Axial Node 15)

a,c

Figure B.2.1-11 15X15 Pellet Diameter Versus Local Burnup (Axial Node 15)

a,c

Figure B.2.1-12 15X15 Clad OD versus Local Burnup (Axial Node 15)

B.2.2 17X17 (0.360" OD) Reference Cases

The following tables and figures summarize the fuel rod design input parameters for 17X17 (0.360" OD) reference fuel rods.

- Table B.2.2-1: 17X17 Reference Case Fuel Rod Parameters
- Table B.2.2-2: 17X17 Reference Case Axial Power Shapes
- Table B.2.2-3: 17X17 Reference Case Rod Power History
- Table B.2.2-4: 17X17 Reference Case Core Operating Conditions
- Figure B.2.2-1: 17X17 Reference Case Rod Average Fast Fluence

- Figure B.2.2-2: 17X17 Reference Case Rod Power History

The following figures illustrate the PAD5 predictions for selected fuel rod parameters. The IFBA fuel rod and the UO_2 fuel rod predictions are provided in the same figures for comparison.

- Figure B.2.2-3: 17X17 Hot Void Volume Versus Rod Average Burnup
- Figure B.2.2-4: 17X17 Rod Internal Pressure Versus Rod Average Burnup
- Figure B.2.2-5: 17X17 Fission Gas Release Versus Rod Average Burnup
- Figure B.2.2-6: 17X17 Pellet-Clad Gap Versus Local Burnup (Axial Node 15)
- Figure B.2.2-7: 17X17 Gap Conductance Versus Local Burnup (Axial Node 15)
- Figure B.2.2-8: 17X17 Fuel Surface Temperature Versus Local Burnup (Axial Node 15)
- Figure B.2.2-9: 17X17 Fuel Average Temperature Versus Local Burnup (Axial Node 15)
- Figure B.2.2-10: 17X17 Fuel Centerline Temperature Versus Local Burnup (Axial Node 15)
- Figure B.2.2-11: 17X17 Pellet Diameter Versus Local Burnup (Axial Node 15)
- Figure B.2.2-12: 17X17 Clad OD Versus Local Burnup (Axial Node 15)

Table B.2.2-1 17X17 Reference Case Fuel Rod Parameters

Description	Input	Upper Bound Uncertainty	Lower Bound Uncertainty	Uncertainty Distribution
Clad Material				
Fuel Stack Length (ft)				
Plenum Length (in)				
Pellet Diameter (in)				
Clad Inner Diameter (in)				
Clad Outer Diameter (in)				
Pellet Length (in)				
Chamfer Depth (in)				
Chamfer Width (in)				
Pellet Dish Spherical Radius (in)				
Pellet Dish Depth (in)				
Pellet Sintering Temperature (°F)				
Axial Blanket Design				
Axial Blanket Length (in)				
Annulus Inner Diameter (in)				
Annulus Volume (in^3)(1)				
Plenum with Annulus Volume (in)(2)				
Initial Cold Void Volume (in^3)				

a,c

Table B.2.2-1 17X17 Reference Case Fuel Rod Parameters (cont.)

Description	Input	Upper Bound Uncertainty	Lower Bound Uncertainty	Uncertainty Distribution
Plenum Spring Diameter (in)				
Plenum Spring Wire Diameter (in)				
Plenum Spring Turns				
Pellet True Density (% Theoretical Density)				
Fuel U-235 Enrichment (w/o)				
Helium Backfill Pressure (psig)				
Rod Pitch (in)				
ZrB_2 IFBA Coating Length (in)				
ZrB_2 IFBA B10 Loading (mg/in)				
ZrB_2 IFBA Coating Thickness (mils)				
Gadolinia Enrichment (w/o)				

a,c

Notes:
1. [ ]a,c
2. [ ]a,c

Table B.2.2-2 17X17 Reference Case Axial Power Shapes

Axial Segment	Power Shape 1	2	3	4	5
1					
2					
3					
4					
5					
6					
7					
8					

a,c

Table B.2.2-2 17X17 Reference Case Axial Power Shapes (cont.)

Axial Segment	Power Shape 1	2	3	4	5
9	a,c				
10					
11					
12					
13					
14					
15					
16					
17					
18					

Axial Segment	Power Shape 6	7	8	9	10
1	a,c				
2					
3					
4					
5					
6					
7					
8					
9					
10					
11					
12					
13					
14					
15					
16					
17					
18					

Table B.2.2-2 17X17 Reference Case Axial Power Shapes (cont.)

Axial Segment	Power Shape				
	11	12	13	14	a,c
1					
2					
3					
4					
5					
6					
7					
8					
9					
10					
11					
12					
13					
14					
15					
16					
17					
18					

Axial Segment	Power Shape				
	15	16	17	18	a,c
1					
2					
3					
4					
5					
6					
7					
8					
9					

Table B.2.2-2 17X17 Reference Case Axial Power Shapes (cont.)

Axial Segment	Power Shape				
	15	16	17	18	a,c
10					
11					
12					
13					
14					
15					
16					
17					
18					

Table B.2.2-3 17X17 Reference Case Rod Power History

Time Step	Time (Hours)	Rod Average Burnup (MWd/MTU)	Rod Average Power (kW/ft)	Axial Power Shape	a,c
1					
2					
3					
4					
5					
6					
7					
8					
9					
10					
11					
12					
13					
14					
15					
16					

Table B.2.2-3 17X17 Reference Case Rod Power History (cont.)

Time Step	Time (Hours)	Rod Average Burnup (MWd/MTU)	Rod Average Power (kW/ft)	Axial Power Shape
17				
18				
19				
20				
21				
22				
23				
24				
25				
26				
27				
28				
29				
30				
31				
32				
33				
34				
35				
36				
37				
38				
39				
40				
41				
42				
43				
44				
45				
46				

a,c

Table B.2.2-3 17X17 Reference Case Rod Power History (cont.)

Time Step	Time (Hours)	Rod Average Burnup (MWd/MTU)	Rod Average Power (kW/ft)	Axial Power Shape
47				
48				
49				
50				
51				
52				
53				
54				
55				

a,c

Table B.2.2-4 17X17 Reference Case Core Operating Conditions

Core Operating Condition	Value
Core Average Linear Power (kW/ft)	
Primary Coolant System Pressure (psi)	
Core Mass Flow Rate (1E+6 lbm/hr-ft^2)	
Core Inlet Temperature (°F)	

a,c

a,c

Figure B.2.2-1 17X17 Reference Case Rod Average Fast Fluence

a,c

Figure B.2.2-2 17X17 Reference Case Rod Power History

a,c

Figure B.2.2-3 17X17 Hot Void Volume Versus Rod Average Burnup

a,c

Figure B.2.2-4 17X17 Rod Internal Pressure Versus Rod Average Burnup

a,c

Figure B.2.2-5 17X17 Fission Gas Release Versus Rod Average Burnup

a,c

Figure B.2.2-6 17X17 Pellet-Clad Gap Versus Local Burnup (Axial Node 15)[2]

2. [

]a,c

a,c

Figure B.2.2-7 17X17 Gap Conductance Versus Local Burnup (Axial Node 15)

a,c

Figure B.2.2-8 17X17 Fuel Surface Temperature Versus Local Burnup (Axial Node 15)

a,c

Figure B.2.2-9 17X17 Fuel Average Temperature Versus Local Burnup (Axial Node 15)

a,c

Figure B.2.2-10 17X17 Fuel Centerline Temperature Versus Local Burnup (Axial Node 15)

a,c

Figure B.2.2-11 17X17 Pellet Diameter Versus Local Burnup (Axial Node 15)

a,c

Figure B.2.2-12 17X17 Clad OD Versus Local Burnup (Axial Node 15)

B.2.3 CE 16X16 (0.382" OD) Reference Cases

The following tables and figures summarize the fuel rod design input parameters for CE 16X16 (0.382" OD) reference fuel rods.

- Table B.2.3-1: CE 16X16 Reference Case Fuel Rod Parameters
- Table B.2.3-2: CE 16X16 Reference Case Axial Power Shapes (Gadolinia Fuel)
- Table B.2.3-3: CE 16X16 Reference Case Axial Power Shapes (UO_2 Fuel)
- Table B.2.3-4: CE 16X16 Reference Case Rod Power History (Gadolinia Fuel)
- Table B.2.3-5: CE 16X16 Reference Case Rod Power History (UO2 Fuel)
- Table B.2.3-6: CE 16X16 Reference Case Core Operating Conditions
- Figure B.2.3-1: CE 16X16 Reference Case Rod Average Fast Fluence
- Figure B.2.3-2: CE 16X16 Reference Case Rod Power History

The following figures illustrate the PAD5 predictions for selected fuel rod parameters. The IFBA fuel rod and the UO_2 fuel rod predictions are provided in the same figures for comparison.

- Figure B.2.3-3: CE 16X16 Hot Void Volume Versus Rod Average Burnup
- Figure B.2.3-4: CE 16X16 Rod Internal Pressure Versus Rod Average Burnup
- Figure B.2.3-5: CE 16X16 Fission Gas Release Versus Rod Average Burnup
- Figure B.2.3-6: CE 16X16 Pellet-Clad Gap Versus Local Burnup (Axial Node 15)
- Figure B.2.3-7: CE 16X16 Gap Conductance Versus Local Burnup (Axial Node 15)
- Figure B.2.3-8: CE 16X16 Fuel Surface Temperature Versus Local Burnup (Axial Node 15)
- Figure B.2.3-9: CE 16X16 Fuel Average Temperature Versus Local Burnup (Axial Node 15)
- Figure B.2.3-10: CE 16X16 Fuel Centerline Temperature Versus Local Burnup (Axial Node 15)
- Figure B.2.3-11: CE 16X16 Pellet Diameter Versus Local Burnup (Axial Node 15)
- Figure B.2.3-12: CE 16X16 Clad OD Versus Local Burnup (Axial Node 15)

Table B.2.3-1 CE 16X16 Reference Case Fuel Rod Parameters

Description	Input	Upper Bound Uncertainty	Lower Bound Uncertainty	Uncertainty Distribution
Clad Material				
Fuel Stack Length (ft)				
Plenum Length (in)				
Pellet Diameter (in)				
Clad Inner Diameter (in)				
Clad Outer Diameter (in)				
Pellet Length (in)				
Chamfer Depth (in)				
Chamfer Width (in)				
Pellet Dish Spherical Radius (in)				
Pellet Dish Depth (in)				
Pellet Sintering Temperature (°F)				
Axial Blanket Design				
Axial Blanket Length (in)				
Annulus Inner Diameter (in)				
Annulus Volume (in^3)				
Plenum with Annulus Volume (in)				

a,c

Table B.2.3-1 CE 16X16 Reference Case Fuel Rod Parameters (cont.)

Description	Input	Upper Bound Uncertainty	Lower Bound Uncertainty	Uncertainty Distribution
Initial Cold Void Volume (in^3)				
Plenum Spring Diameter (in)				
Plenum Spring Wire Diameter (in)				
Plenum Spring Turns				
Pellet True Density (% Theoretical Density)				
Fuel U-235 Enrichment (w/o)				
Helium Backfill Pressure (psig)				
Rod Pitch (in)				
ZrB_2 IFBA Coating Length (in)				
ZrB_2 IFBA B10 Loading (mg/in)				
ZrB_2 IFBA Coating Thickness (mils)				
Gadolinia Enrichment (w/o)				

a,c

Table B.2.3-2 CE 16X16 Reference Case Axial Power Shapes (Gadolinia Fuel)

	Power Shape				
Axial Segment	1	2	3	4	5
1					
2					
3					
4					
5					
6					
7					
8					
9					

a,c

Table B.2.3-2 CE 16X16 Reference Case Axial Power Shapes (Gadolinia Fuel) (cont.)

Axial Segment	Power Shape					
	1	2	3	4	5	a,c
10	[					
11						
12						
13						
14						
15						
16						
17						
18	[					

Axial Segment	Power Shape					
	6	7	8	9	10	a,c
1	[					
2						
3						
4						
5						
6						
7						
8						
9						
10						
11						
12						
13						
14						
15						
16						
17						
18	[					

Table B.2.3-2 CE 16X16 Reference Case Axial Power Shapes (Gadolinia Fuel) (cont.)

Axial Segment	Power Shape				
	11	12	13	14	a,c
1					
2					
3					
4					
5					
6					
7					
8					
9					
10					
11					
12					
13					
14					
15					
16					
17					
18					
Axial Segment	**Power Shape**				
	15	**16**	**17**	**18**	a,c
1					
2					
3					
4					
5					
6					
7					
8					
9					

Table B.2.3-2 CE 16X16 Reference Case Axial Power Shapes (Gadolinia Fuel) (cont.)

Axial Segment	Power Shape				
	15	16	17	18	a,c
10					
11					
12					
13					
14					
15					
16					
17					
18					

Table B.2.3-3 CE 16X16 Reference Case Axial Power Shapes (UO_2 Fuel)

Axial Segment	Power Shape					
	1	2	3	4	5	a,c
1						
2						
3						
4						
5						
6						
7						
8						
9						
10						
11						
12						
13						
14						
15						

Table B.2.3-3 CE 16X16 Reference Case Axial Power Shapes (UO_2 Fuel) (cont.)

Axial Segment	Power Shape					
	1	2	3	4	5	a,c
16	[					
17						
18	[					]
Axial Segment	**Power Shape**					
	6	**7**	**8**	**9**	**10**	a,c
1	[					
2						
3						
4						
5						
6						
7						
8						
9						
10						
11						
12						
13						
14						
15						
16						
17						
18	[					]

Table B.2.3-3 CE 16X16 Reference Case Axial Power Shapes (UO_2 Fuel) (cont.)

Axial Segment	Power Shape					
	11	12	13	14	15	a,c
1						
2						
3						
4						
5						
6						
7						
8						
9						
10						
11						
12						
13						
14						
15						
16						
17						
18						

Axial Segment	Power Shape				a,c
	16	17	18	19	
1					
2					
3					
4					
5					
6					
7					
8					
9					

Table B.2.3-3 CE 16X16 Reference Case Axial Power Shapes (UO_2 Fuel) (cont.)

Axial Segment	Power Shape				
	16	17	18	19	a,c
10					
11					
12					
13					
14					
15					
16					
17					
18					

Table B.2.3-4 CE 16X16 Reference Case Rod Power History (Gadolinia Fuel)

Time Step	Time (Hours)	Rod Average Burnup (MWd/MTU)	Rod Average Power (kW/ft)	Axial Power Shape	a,c
1					
2					
3					
4					
5					
6					
7					
8					
9					
10					
11					
12					
13					
14					
15					
16					

Table B.2.3-4 CE 16X16 Reference Case Rod Power History (Gadolinia Fuel) (cont.)

Time Step	Time (Hours)	Rod Average Burnup (MWd/MTU)	Rod Average Power (kW/ft)	Axial Power Shape
17	[			
18				
19				
20				
21				
22				
23				
24				
25				
26				
27				
28				
29				
30				
31				
32				
33				
34				
35				
36				
37				
38				
39				
40				
41				
42				
43				
44				
45				
46	]			

a,c

Table B.2.3-4 CE 16X16 Reference Case Rod Power History (Gadolinia Fuel) (cont.)

Time Step	Time (Hours)	Rod Average Burnup (MWd/MTU)	Rod Average Power (kW/ft)	Axial Power Shape
47				
48				
49				
50				
51				
52				

a,c

Table B.2.3-5 CE 16X16 Reference Case Rod Power History (UO_2 Fuel)

Time Step	Time (Hours)	Rod Average Burnup (MWd/MTU)	Rod Average Power (kW/ft)	Axial Power Shape
1				
2				
3				
4				
5				
6				
7				
8				
9				
10				
11				
12				
13				
14				
15				
16				
17				
18				
19				
20				

a,c

Table B.2.3-5 CE 16X16 Reference Case Rod Power History (UO_2 Fuel) (cont.)

Time Step	Time (Hours)	Rod Average Burnup (MWd/MTU)	Rod Average Power (kW/ft)	Axial Power Shape
21				
22				
23				
24				
25				
26				
27				
28				
29				
30				
31				
32				
33				
34				
35				
36				
37				
38				
39				
40				
41				
42				
43				
44				
45				
46				
47				
48				
49				
50				

a,c

Table B.2.3-5 CE 16X16 Reference Case Rod Power History (UO_2 Fuel) (cont.)

Time Step	Time (Hours)	Rod Average Burnup (MWd/MTU)	Rod Average Power (kW/ft)	Axial Power Shape
51				
52				
53				
54				
55				
56				
57				

a,c

Table B.2.3-6 CE 16X16 Reference Case Core Operating Conditions

Core Operating Condition	Value
Core Average Linear Power (kW/ft)	
Primary Coolant System Pressure (psi)	
Core Mass Flow Rate (1E+6 lbm/hr-ft^2)	
Core Inlet Temperature (°F)	

a,c

a,c

Figure B.2.3-1 CE 16X16 Reference Case Rod Average Fast Fluence

a,c

Figure B.2.3-2 CE 16X16 Reference Case Rod Power History

a,c

Figure B.2.3-3 CE 16X16 Hot Void Volume Versus Rod Average Burnup

a,c

Figure B.2.3-4 CE 16X16 Rod Internal Pressure Versus Rod Average Burnup

a,c

Figure B.2.3-5 CE 16X16 Fission Gas Release Versus Rod Average Burnup

a,c

Figure B.2.3-6 CE 16X16 Pellet-Clad Gap Versus Local Burnup (Axial Node 15)[3]

3. [

]a,c

a,c

Figure B.2.3-7 CE 16X16 Gap Conductance Versus Local Burnup (Axial Node 15)

a,c

Figure B.2.3-8 CE 16X16 Fuel Surface Temperature Versus Local Burnup (Axial Node 15)

a,c

Figure B.2.3-9 CE 16X16 Fuel Average Temperature Versus Local Burnup (Axial Node 15)

a,c

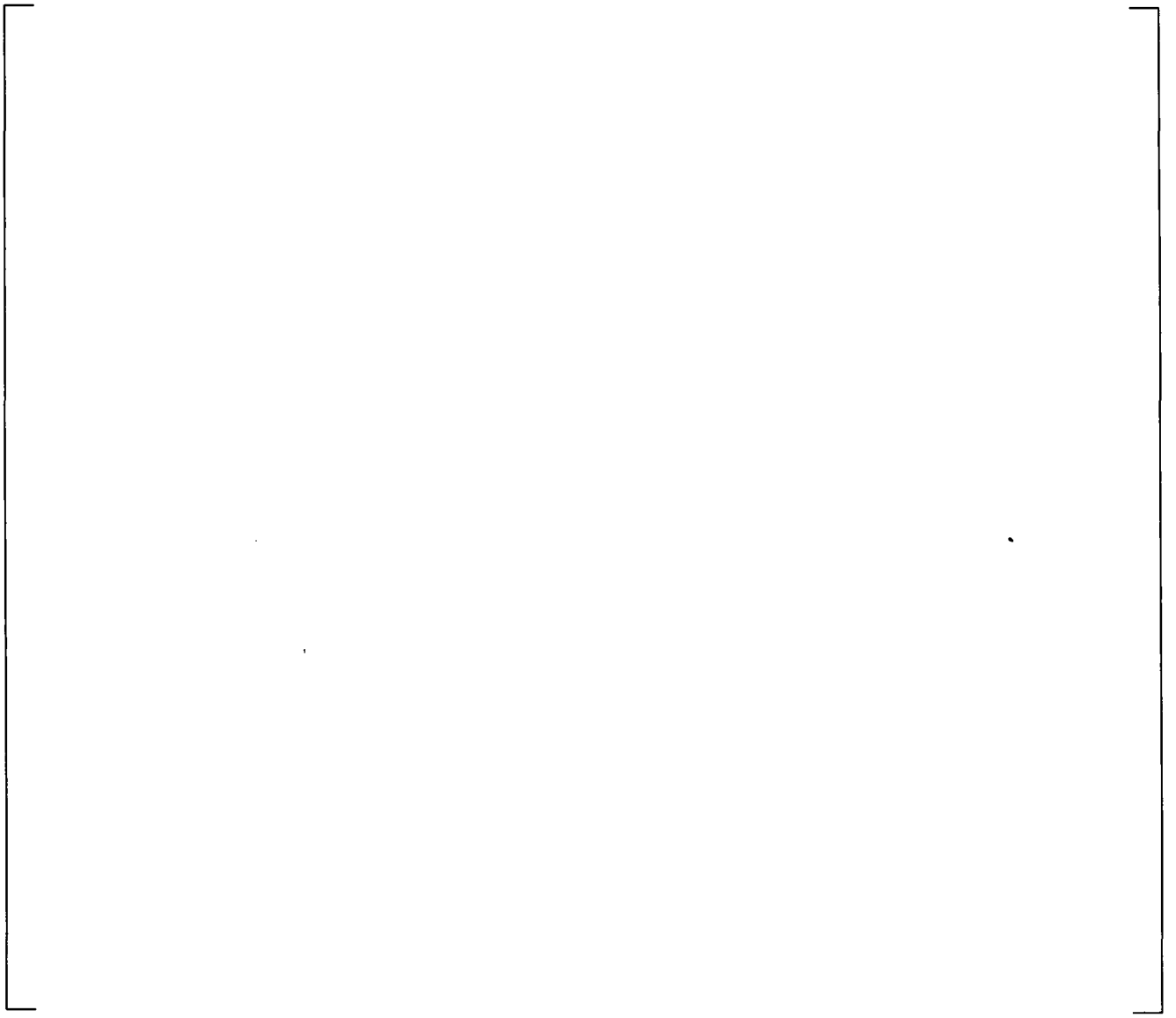

Figure B.2.3-10 CE 16X16 Fuel Centerline Temperature Versus Local Burnup (Axial Node 15)

a,c

Figure B.2.3-11 CE 16X16 Pellet Diameter Versus Local Burnup (Axial Node 15)

a,c

Figure B.2.3-12 CE 16X16 Clad OD Versus Local Burnup (Axial Node 15)

B.3 APPENDIX B REFERENCES

B.1 K. J. Geelhood, W. G. Luscher and C. E. Beyer, "FRAPCON-3.4: A Computer Code for the Calculation of Steady-State Thermal-Mechanical Behavior of Oxide Fuel Rods for High Burnup," NUREG/CR-7022, Vol. 1 (PNNL-19418, Vol. 1), March 2011.